

CONSIDERATIONS ON OPTIMUM DESIGN OF MICRO HEAT PIPE SINKS USING WATER AS  
WORKING FLUID

Except where reference is made to the work of others, the work described in this dissertation is my own or was done in collaboration with my advisory committee. This dissertation does not include proprietary or classified information.

---

Florentina Simionescu

Certificate of Approval:

---

Roy W. Knight  
Assistant Professor  
Mechanical Engineering

---

Daniel K. Harris, Chair  
Associate Professor  
Mechanical Engineering

---

Jay M. Khodadadi  
Professor  
Mechanical Engineering

---

Amnon J. Meir  
Professor  
Mathematics and Statistics

---

Joe F. Pittman  
Interim Dean  
Graduate School

CONSIDERATIONS ON OPTIMUM DESIGN OF MICRO HEAT PIPE SINKS USING WATER AS  
WORKING FLUID

Florentina Simionescu

A Dissertation

Submitted to

the Graduate Faculty of

Auburn University

in Partial Fulfillment of the

Requirements for the

Degree of

Doctor of Philosophy

Auburn, Alabama  
December 15, 2006

CONSIDERATIONS ON OPTIMUM DESIGN OF MICRO HEAT PIPE SINKS USING WATER AS  
WORKING FLUID

Florentina Simionescu

Permission is granted to Auburn University to make copies of this dissertation at its discretion, upon the request of individuals or institutions and at their expense. The author reserves all publication rights.

---

Signature of Author

---

Date of Graduation

## VITA

Florentina Simionescu, daughter of Gheorghe and Ioana Popa, was born on March 22, 1973, in Brăila, Romania. She graduated from Bogdan Petriceicu Hașdeu High School in Buzău, in 1991. In the same year she entered Transilvania University of Brașov and graduated in 1996 with a Bachelor of Science degree in Mechanical Engineering, majoring in Mechatronics. She received a Master of Science degree in Mechanical Engineering and a Master of Environmental Engineering in 1997 and 1999, respectively from the same university. Between 1998-2000 she worked as an instructor in the Department of Precision Mechanics, Transilvania University. In August 2000 she joined the graduate program of the Mathematics Department at Auburn University and received a Master of Applied Mathematics degree in May 2005. In January 2001 she started her Ph.D. studies in the Department of Mechanical Engineering at Auburn University. She married Petru Aurelian Simionescu on February 26, 2000.

DISSERTATION ABSTRACT

CONSIDERATIONS ON OPTIMUM DESIGN OF MICRO HEAT PIPE SINKS USING WATER AS  
WORKING FLUID

Florentina Simionescu

Doctor of Philosophy, December 15, 2006

(M.A.M., Auburn University, 2005)

(M.Env.Eng., Transilvania University of Braşov, 1999)

(M.S., Transilvania University of Braşov, 1997)

(B.S., Transilvania University of Braşov, 1996)

133 Typed Pages

Directed by Daniel K. Harris

The successful operation of RF wideband gap devices dissipating high levels of heat flux requires effective cooling techniques. One of the most promising thermal management strategies is the use of micro heat pipes (MHP). These devices are very thin profile heat spreaders that can be directly attached to the GaAs or GaN substrate whose function is to allow the spreading of the heat flux almost laterally within a 300  $\mu m$  thickness. The objective of the work presented was to estimate the convective heat transfer coefficient of a micro-channel heat sink corresponding to a maximum amount of heat removed from heat source placed on the top surface of the sink. This approach taken used an optimal control technique in which the solution of the heat equation is controlled by the convective boundary condition by taking the heat transfer coefficient as the control parameter. A conjugate gradient method was used to solve the optimal control problem. The results show that the temperature distributions corresponding to the controlled solution are lower than those corresponding to the uncontrolled solution. The difference between the controlled

and uncontrolled temperatures ( $4K - 10K$ ) is smaller than in the case of a planar spreader. This suggests that the convective coefficient corresponding to a finned spreader approaches by design an optimum distribution.

The effect of liquid charge on the performance of MHP sinks is important. A too large amount of fluid leads to a condenser flooding, while a too low fluid charge leads to an evaporator dry-out and an increase in channel wall temperature. An iterative scheme was devised to compute the liquid charge corresponding to the maximum heat transport capacity of the pipe.

This study can provide guidance in designing MHP sinks, which have emerged as an effective technique for cooling electronic components.

## ACKNOWLEDGMENTS

I would like to express my deepest gratitude to my advisor, Dr. Daniel Harris, Associate Professor of Mechanical Engineering, for his guidance and support toward the completion of this dissertation.

Special thanks are extended to Dr. A.J. Meir, Professor of Mathematics, for his invaluable help when needed mostly. I would also like to acknowledge Dr. Roy Knight, Assistant Professor of Mechanical Engineering, and Dr. Jay Khodadadi, Professor of Mechanical Engineering for their help and suggestions as committee members, as well as Dr. William Ashurst, the outside reader, for his thorough review of the manuscript.

I am grateful to my parents and sister for their love and moral support. Last but not least, I would like to thank my husband, Aurelian for his love, patience, and permanent encouragement that made this work possible.

In loving memory of my grandmother Caterina

Style manual or journal used International Journal of Mass and Heat Transfer(together with the style known as “aums”).

---

Computer software used The document preparation package T<sub>E</sub>X (specifically L<sup>A</sup>T<sub>E</sub>X) together with the departmental style-file aums.sty.

---



## TABLE OF CONTENTS

|                 |  |    |
|-----------------|--|----|
| LIST OF FIGURES |  | xi |
| 1               | INTRODUCTION   | 6  |
| 1.1             | Background . . . . .   | 6  |
| 1.2             | Objectives . . . . .   | 8  |
| 1.3             | Literature review . . . . .  | 8  |
| 2               | OPTIMAL CONVECTIVE HEAT TRANSFER COEFFICIENT OF A PLANAR SPREADER                  | 24 |
| 2.1             | Problem specification . . . . .  | 24 |
| 2.2             | Existence and uniqueness of solution . . . . .                                     | 28 |
| 2.3             | Optimal control for model problem . . . . .  | 29 |
| 2.3.1           | The direct problem . . . . .   | 30 |
| 2.3.2           | The optimal control problem . . . . .  | 31 |
| 2.3.3           | Existence and uniqueness of an optimal control . . . . .                           | 32 |
| 2.3.4           | Conjugate gradient algorithm . . . . .   | 33 |
| 2.3.5           | Sensitivity problem and calculation of the search step size . . . . .              | 34 |
| 2.3.6           | The adjoint problem . . . . .  | 36 |
| 2.3.7           | Computational algorithm . . . . .  | 38 |
| 2.4             | Implementation and numerical procedure . . . . .                                   | 39 |
| 2.5             | Results and discussions . . . . .  | 41 |
| 3               | OPTIMAL DESIGN OF A MICRO HEAT PIPE  | 44 |
| 3.1             | Problem specification . . . . .  | 44 |
| 3.2             | The direct problem . . . . .   | 45 |
| 3.2.1           | Heat transfer equations corresponding to the GaAs slab and silicon wafer . . . . . | 45 |
| 3.2.2           | 1-D Micro heat pipe model . . . . .  | 49 |
| 3.3             | The optimal control problem with $Bi$ and geometrical parameters as controls       | 62 |
| 3.3.1           | Conjugate gradient algorithm . . . . .   | 63 |
| 3.3.2           | Sensitivity problem and calculation of the search step sizes . . . . .             | 64 |
| 3.3.3           | Adjoint problems . . . . .   | 69 |
| 3.3.4           | Computational algorithm . . . . .  | 75 |
| 3.3.5           | Implementation and numerical procedure . . . . .                                   | 76 |
| 3.3.6           | Results and discussions . . . . .  | 76 |
| 3.4             | Liquid charge corresponding to maximum heat transport capacity of the pipe         | 78 |
| 3.4.1           | Computational procedure . . . . .  | 79 |
| 3.4.2           | Results and discussions . . . . .  | 80 |

|     |                       |    |
|-----|-----------------------|----|
| 3.5 | Conclusions . . . . . | 82 |
| 4   | APPENDIX              | 86 |

## LIST OF FIGURES

|     |  |    |
|-----|--|----|
| 2.1 | Computational domain. . . . .  | 25 |
| 2.2 | Structure of matrix $\mathbf{A}$ . . . . .   | 41 |
| 3.1 | Schematic of a MHP sink. . . . .   | 45 |
| 3.2 | Computational domain. . . . .  | 46 |
| 3.3 | Schematic of a MHP. . . . .  | 51 |
| 3.4 | Control volume used to derive the conservation equations . . . . .   | 52 |
| 3.5 | A cross section of the MHP with liquid recessed into the corner . . . . .                                    | 53 |
| 3.6 | Conservation of mass . . . . .   | 56 |
| 3.7 | Conservation of momentum . . . . .   | 57 |
| 4.1 | Graphs of controlled and uncontrolled solutions for different values of $\alpha$ . . .                       | 87 |
| 4.2 | Distributions of $Bi$ for different values of $\alpha$ . . . . .   | 88 |
| 4.3 | Distributions of $T - T_\infty$ at the chip-spreader interface for different values of $\alpha$ . . .        | 89 |
| 4.4 | Distributions of $T - T_\infty$ through a vertical symmetry plane for different values of $\alpha$ . . . . . | 90 |
| 4.5 | Distributions of optimal $Bi$ corresponding to $N = 60$ and different channel depths. . . . .                | 91 |
| 4.6 | Distributions of optimal $Bi$ corresponding to $N = 58$ and different channel depths. . . . .                | 92 |
| 4.7 | Distributions of optimal $Bi$ corresponding to $N = 56$ and different channel depths. . . . .                | 93 |
| 4.8 | Distributions of optimal $Bi$ corresponding to $N = 30$ and different channel depths. . . . .                | 94 |

|      |   |     |
|------|---|-----|
| 4.9  | Temperature distributions $T - T_\infty$ corresponding to $N = 60$ . . . . .  | 95  |
| 4.10 | Temperature distributions $T - T_\infty$ corresponding to $N = 58$ . . . . .  | 96  |
| 4.11 | Temperature distributions $T - T_\infty$ corresponding to $N = 56$ . . . . .  | 97  |
| 4.12 | Temperature distributions $T - T_\infty$ corresponding to $N = 30$ . . . . .  | 98  |
| 4.13 | Distribution of the meniscus radius for different values of $\alpha$ and channel depths ( $N = 60$ ). . . . .   | 99  |
| 4.14 | Distributions of the liquid and vapor velocities for $H_1 = 75\mu m$ and different values of $\alpha$ ( $N = 60$ ). . . . .   | 100 |
| 4.15 | Distributions of the liquid and vapor velocities for $H_1 = 100\mu m$ and different values of $\alpha$ ( $N = 60$ ). . . . .  | 101 |
| 4.16 | Distributions of the liquid and vapor velocities for $H_1 = 125\mu m$ and different values of $\alpha$ ( $N = 60$ ). . . . .  | 102 |
| 4.17 | Distributions of the liquid and vapor velocities for $H_1 = 150\mu m$ and different values of $\alpha$ ( $N = 60$ ). . . . .  | 103 |
| 4.18 | Distributions of the liquid and vapor pressures for different values of $\alpha$ and channel depths ( $N = 60$ ). . . . .   | 104 |
| 4.19 | Distributions of the 'ideal' optimum $Bi$ and the optimum $Bi$ corresponding to the maximum heat transport capacity of the pipe, for $N = 60$ and different channel depths. . . . . | 105 |
| 4.20 | Distributions of the 'ideal' optimum $Bi$ and the optimum $Bi$ corresponding to the maximum heat transport capacity of the pipe, for $N = 58$ and different channel depths. . . . . | 106 |
| 4.21 | Distributions of the 'ideal' optimum $Bi$ and the optimum $Bi$ corresponding to the maximum heat transport capacity of the pipe, for $N = 56$ and different channel depths. . . . . | 107 |
| 4.22 | Distributions of the 'ideal' optimum $Bi$ and the optimum $Bi$ corresponding to the maximum heat transport capacity of the pipe, for $N = 30$ and different channel depths. . . . . | 108 |
| 4.23 | Variations of the liquid charge with $r_0$ for different channel depths ( $N = 60$ ). . . . .   | 109 |

|      |   |     |
|------|---|-----|
| 4.24 | Variations of MHP heat transport capacity with $r_0$ for different channel depths ( $N = 60$ ). . . . . | 110 |
| 4.25 | Variations of liquid charge with channel depth for different values of $\alpha$ . . . .                 | 111 |
| 4.26 | Percent of volume charge corresponding to maximum heat transport capacity of the pipe. . . . .          | 112 |
| 4.27 | Variations of MHP heat transport capacity with channel depth for different values of $\alpha$ . . . . . | 113 |

## Nomenclature

|                    |  |
|--------------------|--|
| $a$                | bilinear form  |
| $c_l, c_{lw}, c_i$ | geometrical constants (functions of $\phi$ , $\theta$ , and $r$ )      |
| $d_c$              | height of chip   |
| $f_l$              | friction coefficient for liquid phase                                  |
| $f_v$              | friction coefficient for vapor phase                                   |
| $h$                | convective heat transfer coefficient                                   |
| $h_{fg}$           | latent heat of vaporization  |
| $k_c$              | coefficient of thermal conductivity for chip                           |
| $k_s$              | coefficient of thermal conductivity for planar spreader                |
| $k_{Si}$           | coefficient of thermal conductivity for Si                             |
| $k_{GaAs}$         | coefficient of thermal conductivity for GaAs                           |
| $l$                | width of channel   |
| $l_c$              | length of chip   |
| $p$                | channel aspect ratio   |
| $q_r$              | maximum heat transport capacity of MHP as a fraction of the input heat |
| $q_v$              | volumetric heat source   |
| $q_w$              | heat flux entering the MHP   |
| $r$                | meniscus radius  |
| $r_{max}$          | maximum radius of curvature  |
| $w_1$              | length of heating area   |
| $w_2$              | length of GaAs slab  |
| $w_c$              | width of chip  |

|               |  |
|---------------|--|
| $A_i$         | liquid-vapor interfacial area inside MHP |
| $A_l$         | liquid cross sectional area inside MHP   |
| $A_v$         | vapor cross sectional area inside MHP    |
| $A_{lw}$      | wall/liquid area inside MHP              |
| $A_{vw}$      | wall/vapor area inside MHP               |
| $Bi$          | Biot number                              |
| $Bi^*$        | minimum Biot number                      |
| $Bo$          | Bond number                              |
| $C^{0,1}$     | space of Lipschitz continuous functions  |
| $Ca$          | capillary number                         |
| $D_s$         | height of planar spreader                |
| $D_H$         | hydraulic diameter of empty pipe         |
| $D_{H_l}$     | hydraulic diameter of liquid phase       |
| $D_{H_v}$     | hydraulic diameter of vapor phase        |
| $H^1(\Omega)$ | Sobolev space                            |
| $H_1$         | height of fin (channel)                  |
| $H_2$         | height of Si substrate                   |
| $H_3$         | height of GaAs slab                      |
| $J$           | functional to be minimized               |
| $L$           | width of computational domain            |
| $L^2(\Omega)$ | space of square integrable functions     |
| $L_a$         | length of MHP adiabatic section          |
| $L_e$         | length of MHP evaporator section         |

|               |   |
|---------------|---|
| $L_s$         | length of planar spreader                             |
| $L_t$         | width of MHP heat sink                                |
| $N$           | number of channels                                    |
| $P, P_1, P_2$ | search directions in conjugate gradient algorithm     |
| $P_l$         | liquid pressure                                       |
| $P_v$         | vapor pressure  |
| $P_{ref}$     | reference pressure                                    |
| $\dot{Q}$     | dissipated power                                      |
| $R_T$         | total thermal resistance of a heat sink               |
| $Re_l$        | Reynolds number for liquid phase                      |
| $Re_v$        | Reynolds number for vapor phase                       |
| $S$           | chip/planar spreader interfacial area                 |
| $T_\infty$    | ambient temperature                                   |
| $T^*$         | minimum temperature                                   |
| $T_c$         | temperature distribution within the chip              |
| $T_f$         | temperature of coolant                                |
| $T_s$         | temperature distribution within the spreader          |
| $T_w$         | micro-channel wall temperature                        |
| $T_A$         | temperature distribution within GaAs slab             |
| $T_B$         | temperature distribution within Si base plate         |
| $T_C$         | temperature distribution within separating wall (fin) |
| $U_{ad}$      | set of admissible controls                            |
| $U_l$         | liquid velocity                                       |



|           |                                   |
|-----------|-----------------------------------|
| $U_v$     | vapor velocity                    |
| $U_{ref}$ | reference velocity                |
| $V_{il}$  | liquid phase interfacial velocity |
| $V_{iv}$  | vapor phase interfacial velocity  |
| $W_s$     | width of planar spreader          |
| $W$       | length of MHP sink                |

### Greek letters

|                                   |   |
|-----------------------------------|---|
| $\alpha$                          | weighting coefficient   |
| $\beta, \beta_1, \beta_2$         | search sizes in conjugate gradient algorithm                      |
| $\gamma, \gamma_1, \gamma_2$      | conjugate coefficient in conjugate gradient algorithm             |
| $\partial\Omega$                  | boundary of domain $\Omega$                                       |
| $\zeta_1, \zeta_2$                | adjoint variables corresponding to chip and spreader respectively |
| $\theta$                          | wall/liquid contact angle   |
| $\theta_1$                        | MHP sink tilt angle   |
| $\lambda_1, \lambda_2, \lambda_3$ | adjoint variables associated with $p$                             |
| $\xi_1, \xi_2, \xi_3$             | adjoint variables associated with $Bi$                            |
| $\rho_l$                          | liquid density  |
| $\rho_v$                          | vapor density   |
| $\sigma$                          | surface tension   |
| $\tau_{li}$                       | interfacial shear stress for liquid phase                         |
| $\tau_{vi}$                       | interfacial shear stress for vapor phase                          |
| $\tau_{lw}$                       | liquid/wall shear stress  |

|                  |  |
|------------------|--|
| $\tau_{vw}$      | vapor/wall shear stress  |
| $\phi$           | pipe corner angle  |
| $\Gamma$         | micro-channel cross section  |
| $\Gamma_s$       | bottom surface of planar spreader  |
| $\Delta p$       | small perturbation of $p$  |
| $\Delta Bi$      | small perturbation of $Bi$   |
| $\Delta T_c$     | sensitivity temperature within the chip  |
| $\Delta T_s$     | sensitivity temperature within the planar spreader                                 |
| $\Delta T_A^1$   | sensitivity temperature within GaAs slab when $p$ is perturbed by $\Delta p$       |
| $\Delta T_B^1$   | sensitivity temperature within Si base plate when $p$ is perturbed by $\Delta p$   |
| $\Delta T_C^1$   | sensitivity temperature within fin when $p$ is perturbed by $\Delta p$             |
| $\Delta T_A^2$   | sensitivity temperature within GaAs slab when $Bi$ is perturbed by $\Delta Bi$     |
| $\Delta T_B^2$   | sensitivity temperature within Si base plate when $Bi$ is perturbed by $\Delta Bi$ |
| $\Delta T_C^2$   | sensitivity temperature within fin when $Bi$ is perturbed by $\Delta Bi$           |
| $\Delta T_{S-C}$ | temperature rise above the input coolant temperature                               |
| $\Omega$         | computational domain for planar spreader   |
| $\Omega_c$       | chip subdomain   |
| $\Omega_s$       | planar spreader subdomain  |

CHAPTER 1  
INTRODUCTION

## 1.1 Background

With the increase in heat dissipation from microelectronic devices and their size reduction, thermal management becomes a more important element of electronic product design. Both the reliability and life expectancy of electronic equipment are inversely related to the component temperature of the equipment. The relationship between the reliability and the operating temperature of a typical silicon semi-conductor device shows that a reduction in the temperature corresponds to an exponential increase in the reliability and life expectancy of the device [35], [10], [75], [56]. Therefore, long life and reliable performance of a component may be achieved by effectively controlling the device operating temperature within the limits set by the device design engineers.

Heat sinks are devices that enhance heat dissipation from a hot surface, usually the case of a heat generating component, to a cooler ambient. The primary purpose of a heat sink is to maintain the device temperature below the maximum allowable temperature specified by the device manufacturers.

When designing or selecting an appropriate heat sink one needs to examine various parameters that affect not only the heat sink performance itself, but also the overall performance of the system. The performance of a heat sink is measured by its thermal resistance

$$R_T = \Delta T_{S-C} / \dot{Q} \quad (1.1)$$

where  $\Delta T_{S-C}$  is the temperature rise of the electronic component above the input coolant temperature and  $\dot{Q}$  is the dissipated power. The total thermal resistance is a sum of three components that account for conduction through the silicon (aluminum/copper) substrate, convection from the substrate to the cooling fluid, and resistance due to the heating of fluid as it absorbs the energy passing through the substrate, respectively. The optimization of a heat sink aims to minimize the total thermal resistance. The optimization procedure is performed subject to design constraints such as:

- Available pressure drop;
- Cross sectional geometry of incoming flow;
- Ambient fluid temperature;
- Amount of required heat dissipation;
- Maximum size of the heat sink;
- Orientation with respect to gravity, etc.

Usually the sinks are equipped with extended surfaces (fins) that increase the amount of heat removed. The parameters over which the designer has control when performing the optimization of a heat sink typically include:

- Fin height;
- Fin length;
- Fin thickness;
- Number/density of fins;

- Fin shape/profile;
- Base plate thickness;
- Heat sink material;
- Cooling fluid properties, etc.

There is always an interdependence among the above mentioned parameters. The impact one parameter has on the performance of a heat sink can not be determined without concurrently considering the contribution of the other parameters. For example, a greater fin height provides additional surface area for heat dissipation and improves the overall thermal performance. However, if the available volumetric flow rate is fixed, the overall performance may deteriorate by increasing the fin height.

## **1.2 Objectives**

The purpose of this work is to study the performance of a heat sink equipped with an array of micro heat pipes. The geometrical parameters of the heat sink and the heat transfer coefficient are optimized using an optimal control technique. These optimal design parameters correspond to a maximum amount of heat removed from a heat source placed on top of the heat sink. The liquid charge corresponding to the maximum heat transport capacity of the pipe is then computed.

## **1.3 Literature review**

During the last two decades, several cooling schemes ranging from simple planar thermal spreaders [9], [19], to more sophisticated two-phase flow heat sinks and microjet cooling

devices have been proposed and extensively studied both experimentally and theoretically. Some of the most representative works are briefly presented in the sequel.

Peles et al. [48] analyzed the performance of micro pin fin heat sinks. A simplified expression for the total thermal resistance was derived and experimentally validated. Geometrical and thermo-hydraulic parameters affecting the total thermal resistance have been discussed. It has been found that very low thermal resistances are achievable using a pin fin heat sink. The thermal resistances achieved using micro pin fin heat sinks were as low as the ones with micro-channel convective flows. The advantage of using pin fin configurations was the design flexibility in the geometrical selection of the pin shapes and their spacing. Experiments were performed by Wei and Honda [71] to study the effects of square micro pin fins on boiling heat transfer from silicon chips immersed in a pool of degassed or gas-dissolved FC-72. The micro pin finned chips showed a considerable heat transfer enhancement in the nucleate boiling region and increase in the critical heat flux, as compared to the smooth chip. The maximum value of allowable heat flux ( $84.5W/cm^2$ ), 4.2 times as large as that for the smooth chip, was obtained for a fin height of  $270\mu m$ , a fin width of  $50\mu m$ , and a liquid subcooling of  $45K$ . Another numerical study on pin fin heat exchangers was carried out by Saha and Acharya [55] to analyze the unsteady 3-D flow and heat transfer in a parallel-plate channel heat exchanger with in line arrays of periodically mounted rectangular cylinders (pins) at various Reynolds numbers and geometrical configurations. Results were presented to highlight different parametric effects, using both the instantaneous snapshots of the flow and heat transfer fields and the averaged (space- and time-averaged in case of unsteady flows) integral parameters, such as the friction factor and the Nusselt number. It was found that the thermal performance increases significantly when the flow becomes unsteady.

The thermal performance of liquid cooling heat sinks is usually one or two orders of magnitude greater than the one of the heat sinks using air for cooling. The air cooling devices on the other hand, are cheap, easy to implement, and reliable. Micro-channel heat exchangers combine the attributes of very high surface area to volume ratio, large convective heat transfer coefficient, small mass and volume, and small coolant inventory. Numerous investigations have been conducted on forced convection in micro-channels concerning both single phase and two-phase flows. A comparison of single-phase and two-phase (liquid-vapor) heat sinks shows that there is a significant enhancement in heat transfer in the latter case. The latent heat transfer in the two-phase systems allows the same amount of heat transfer at a much lower temperature difference (between the evaporator and the condenser).

The micro-channel heat sink concept was first introduced by Tuckerman and Pease in the early 1980s [68]. They performed an optimization of the micro-channel heat sink design subject to a fully developed and laminar in nature flow through the channels and a laminar Nusselt number. The channel to fin width ratio, the pressure drop through the fin array, the pumping work, the planar dimensions and the fin efficiency were fixed. They fabricated and tested several micro-channel heat sinks in a  $1\text{cm} \times 1\text{cm}$  silicon wafer. The experimental findings were in good agreement with the theoretical predictions. The heat sink with channels separated by  $50\mu\text{m}$  thick walls, having a width of  $50\mu\text{m}$  and a depth of  $302\mu\text{m}$  proved to be the optimal design solution. Using water as cooling fluid, the micro-channel heat sink was capable of dissipating  $790\text{W}/\text{cm}^2$  with a maximum substrate temperature raise of  $70^\circ\text{C}$  above the water inlet temperature for a pressure drop of  $31\text{psi}$ .

Following the work of Tuckerman and Pease [68] much research has been conducted for micro-channel heat sinks.

Weisberg et al. [72] analyzed the micro-channel heat exchangers solving for the coupled temperature fields within the solid substrate and the working fluid. A 2-D heat transfer was considered in both the fins and the fluid charged channels. The minimum thermal resistance was attained for a fin to channel width ratio equal to 1, this result being in accordance with the one obtained by Tuckerman and Pease [68].

Knight et al. [32] performed a micro-channel heat sink optimization allowing the relaxation of the aspect ratio, the channel to fin width ratio, Nusselt number, flow regime and volumetric flow rate. They also included in their analysis the effects of the developing channel flow. The results indicated that when the pressure drop through the channel is small, laminar solutions yield lower thermal resistance than turbulent solutions. Conversely, when the pressure drop is large the optimal thermal resistance is found in the turbulent region. With the relaxation of the above constraints, configurations that produced significant improvement in thermal resistance over that presented by Tuckerman and Pease [68] were found. When the turbulent regime was allowed, the thermal resistance was reduced by 35% from that of Tuckerman and Pease [68]. These theoretical predictions were experimentally verified [33]. Three heat sink systems from aluminum alloy with 5, 11 and 8 fins, respectively were built and tested, using air as coolant. The fin system with the lowest thermal resistance was predicted to occur for 9 channels, or 8 fins, and a ratio of fin to channel width of 0.565. This configuration was predicted to yield a turbulent flow, and a lower resistance than any laminar configuration operating under the same constraints. At 50W of power



dissipation, the optimal design operated about  $8^{\circ}C$  cooler than the 5 fin system, and about  $4^{\circ}C$  cooler than the 11 fin system.

The entrance effects on the thermal performance of the micro-channel heat sink were also examined by Ryu et al. [53]. They performed a 3-D heat transfer analysis which was further incorporated in an optimization scheme to find the optimal design parameters of the micro-channel heat sink, that minimize the thermal resistance subject to a specified pumping power and a channel aspect ratio less than 10. They pointed out that the thermal entrance effect is substantial when the working fluid is water ( $Pr \approx 7$ ). They varied the number of channels and obtained the associated design variables and the thermal resistance. A low sensitivity of the thermal resistance to the number of channels was found. When the number of channels was reduced to half, the thermal resistance increased by about 15% of the optimal value. It was shown that both the optimal dimensions and the thermal resistance have a power-law dependence on the pumping power. The optimal design parameters for a pumping power of  $2.56W$  and an input heat flux of  $100W/cm^2$  were found as follows: the number of channels  $N = 124$ , the channel width  $W = 45.3\mu m$ , and the channel height  $H = 453\mu m$  for a silicon substrate of  $100\mu m$ . The corresponding thermal resistance was 0.069. The same authors studied the performance of the manifold micro-channel heat sinks [54]. These heat sinks have an array of manifold dividers perpendicular to the micro-channels and placed atop of them. The coolant flows through the alternating inlet and outlet manifolds in the direction normal to the heat-sink base, to and from the segmented micro-channels, reducing the flow path to a small fraction of the total length of a heat sink. The shortened flow path reduces the pressure drop and restrains the growth of the thermal boundary layer in the streamwise direction. Compared to the traditional heat sink for the

identical heat load and pumping power, the thermal resistance was lowered by more than 50% while the maximum temperature variation on the heated wall was improved by tenfold.

Peng and Peterson [50] investigated experimentally the single-phase forced convective heat transfer and flow characteristics of water in micro-channel structures/plates with small rectangular channels having hydraulic diameters of  $0.133\text{mm}$ – $0.367\text{mm}$  and different aspect ratios. The laminar heat transfer was found to be dependent on the aspect ratio  $H/W$  and the ratio of the hydraulic diameter to the center-to-center distance of the micro-channels. The turbulent heat transfer on the other hand was found to be a function of a new dimensionless variable,  $Z = \min(H, W)/\max(H, W)$ , such that  $Z = 0.5$  will give the optimum configuration for turbulent heat transfer regardless of the groove aspect ratio. The friction factor or flow resistance reached a minimum value as  $Z$  approached 0.5. Empirical correlations were suggested for calculating both the heat transfer and pressure drop. Another experimental work by Peng and Peterson [49], [51] showed that the range of the transition zone, and the heat transfer characteristics of both the transition and laminar flow regimes, were strongly affected by the liquid temperature, liquid velocity and micro-channel size.

Zhao and Lu [76] used two approaches in analyzing the micro-channel heat sinks: the porous medium model and the fin model. In the porous medium approach, the modified Darcy equation for the fluid and the two-equation model for the heat transfer between the solid and fluid phases were employed. It was shown that the overall Nusselt number increases with increasing aspect ratio and decreases with increasing effective thermal conductivity ratio. Whereas the porous medium model predicted the existence of an optimal porosity, the fin approach predicted that the heat transfer capability of the heat sink increases monotonically with the porosity (defined as the ratio of the void volume to the total

volume). The effect of turbulent heat transfer within the micro-channel was also discussed and it was found that turbulent heat transfer results in a decrease of optimum porosity in comparison to that for laminar flow. The concept of micro-channel cooling in combination with micro heat pipes was proposed. Using a lumped capacitance technique, the micro heat pipes were modeled as homogeneous, solid regions embedded in the plates with an effective thermal conductivity that was assumed to be approximately 10 times that of silicon or copper. It was observed that the enhancement in heat transfer due to the incorporation of heat pipes becomes significant as the channel aspect ratio increases and for highly conducting coolants, such as water. Another porous medium model developed by Wang et al. [70] for two phase flows in mini-channels was used to predict the capillary limit of an operating micro heat pipe. Imke [26] developed a code to simulate the micro-channel flow and heat transfer in compact heat exchangers. The method was based on a forced convection porous medium approach combined with conventional pipe flow closure relations and solved for outlet temperatures, pressure losses, and vapor volume fractions. The code was applied to single phase cross flow and counter flow heat exchangers using water as working fluid. The experimental findings were in good agreement with the theoretical predictions.

Vafai and Zhu [69] proposed the design of two-layer micro-channel heat sinks based on stacking two layers of micro-channels one atop the other, with coolant flow in opposite directions in each of the micro-channel layers. This solution aimed to reduce the undesirable temperature gradients in the streamwise direction. The maximum temperature difference along the pipe was found to be 3 times lower than that of a one-layer micro-channel system. Some optimization issues for design parameters were addressed. The optimum ratio of channel width to fin width was found to be 0.6. In the analysis of one-layer structure

was pointed out that smaller channel size and higher aspect ratio can reduce the thermal resistance. This observation proved to hold true for two-layer structures as well. For the ratio of the pressure drop in the channel array closest to the heat source to the pressure drop in the second array the recommended optimum value was 2.5 – 3. Another parameter discussed was the channel length and was shown that a longer micro-channel design can indeed substantially reduce the streamwise temperature variation.

Wu and Cheng investigated the effect of surface condition on the performance of silicon micro-channels [73]. Based on 168 experimental data points, dimensionless correlations for the Nusselt number and the apparent friction constant were obtained for the flow of water in trapezoidal micro-channels, having different geometric parameters, surface roughness and surface hydrophilic properties. It was found that the laminar Nusselt number and apparent friction constant of the trapezoidal micro-channels increase with the increase of surface roughness. This increase is more obvious at large Reynolds numbers than at low Reynolds numbers. The Nusselt number and apparent friction constant of the trapezoidal micro-channels having strong hydrophilic surfaces (thermal oxide surfaces) were larger than those having weak hydrophilic surfaces (silicon surfaces). This suggested that convective heat transfer can be enhanced by increasing the surface hydrophilic capability.

A detailed 3-D analysis heat transfer in micro-channel heat sinks was provided by Li et al. [39]. In their study the variation of the liquid thermophysical properties with the bulk temperature was considered. For the 10mm long, 57 $\mu$ m wide, and 180 $\mu$ m deep rectangular micro-channels analyzed, a variation in the reference temperature from 20°C to 32°C changed the mean velocity from 1.11 to 1.31m/s. This resulted in a corresponding change in Reynolds number from 96 to 144.

Ambatipudi and Rahman [2] investigated numerically the heat transfer in a  $\langle 101 \rangle$  silicon substrate containing micro-channels. The effects of channel aspect ratio, Reynolds number, and number of channels on the thermal performance of the device were investigated. It was found that the Nusselt number is greater for a heat sink with a larger number of channels and a larger Reynolds number. For  $Re = 673$ , the optimum channel depth that maximizes Nusselt number occurred at  $300\mu m$ .

Chein and Huang [5] studied the performance of micro-channel heat sinks using nanofluids as cooling fluids. The nanofluid was a mixture of pure water and nanoscale copper particles with various volume fractions. It was found that nanofluids could enhance the micro-channel heat sinks performance due to the increase in thermal conductivity of coolant and the nanoparticle thermal dispersion effect.

Toh et al. [67] investigated the flow and heat transfer in micro-channels considering the case of temperature dependent thermophysical properties. It was concluded that a drastic change in the friction coefficient is due to the change in the viscosity of fluid. At lower Reynolds numbers, the fluid attains higher temperatures leading to lower viscosities. This results in lower pressure drop and hence the decrease in the value of the friction coefficient. At higher Reynolds numbers, the fluid temperature at the exit is almost the same as the inlet temperature. As a result the viscosity is almost constant and the friction coefficient approaches the constant properties.

Two-phase micro-channel heat sinks (or micro heat pipes) are an alternative to single-phase micro-channel heat sinks. They use the latent heat of vaporization to transfer heat from the evaporator to the condenser, maintaining the sink at a uniform temperature. Hassan et al. [18] present a state-of-the-art literature review of the research progress in the

field of micro-channel heat sinks. Earlier research works using single-phase coolants in their heat sinks and more recent works using two-phase coolants were presented. They pointed out that single-phase flow in micro-channel heat sinks requires high flow rates or smaller hydraulic diameters, consequently resulting in larger pressure drops.

Groll et al. [15] provide an extended literature survey on the micro heat pipes used for thermal control of electronic equipment. From a review of more than 100 papers micro heat pipe sinks were classified and compared according to their performances, designs, and thermophysical parameters. Common working fluids and wall materials were discussed and possibilities for combinations were presented. As a measure of heat transport capacity a *liquid transport factor*  $N_l$  was defined,  $N_l = \sigma h_{fg} / \nu_l$ , where  $\sigma$  is the surface tension,  $h_{fg}$  is the latent heat of vaporization, and  $\nu_l$  the kinematic viscosity of the liquid. This factor indicated that for the temperature range of  $0^\circ\text{C} - 100^\circ\text{C}$ , typical for electronic applications only acetone, methanol, ethanol, and water are suitable. Copper, aluminum, their alloys, and stainless steel were mentioned as common heat pipe wall materials. Tested combinations of fluid/wall material with theoretically no degradation were referred to as compatible combinations (e.g. water and either copper, stainless steel, nickel, titanium). Investigations on the effect of fluid-solid contact angle were presented. It was concluded that the use of a wetting fluid (small contact angle) should enhance the micro heat pipe performance. The effect of the micro heat pipe dimensions was discussed in terms of Bond number. For the micro heat pipe to operate properly regardless of orientation, the capillary forces should overcome the gravitational forces leading to  $Bo < 1$ . Therefore micro heat pipes can not be too long.

Experimental work on the performance of micro heat pipe arrays was conducted by many researchers. Launay et al. [36] investigated the thermal behavior of two silicon micro heat pipe arrays of triangular cross section. The first array made from two silicon wafers included 55 triangular ethanol charged micro-channels,  $230\mu m$  wide and  $170\mu m$  deep. One wafer contained the channels and the other one was used to seal them. The second array made from three silicon wafers had 25 micro-channels  $500\mu m$  wide and  $342\mu m$  deep and small triangular channels etched into the lower wafer which were used as arteries to drain the liquid to the evaporator. Methanol was used as working fluid. With the assumption of no heat losses and no heat conduction into the silicon wafer the effective thermal conductivity of the second array was found to be  $900W/mK$ , three times greater than the one of the first array. This improvement was due to the increased flow cross sectional area and a reduced pressure drop between the evaporator and condenser. The effect of liquid charge on the performance of the first micro heat sink was also analyzed. It was found that the enhancement factor for this micro heat pipe array, defined as the ratio between the thermal conductivity of the charged and empty micro heat pipe, had a maximum value of 7% corresponding to an optimum liquid charge of 24% of the channels' volume. This enhancement factor was nearly constant for power inputs ranging from 0.5 to 5W. The reason for this low improvement is that a large part of the heat is transferred by conduction through the silicon.

Le Berre et al. [4] studied experimentally the performance of a micro heat pipe array for various filling charges under various experimental conditions. The micro heat pipe array was  $20mm \times 20mm$  and consisted of 27 parallel triangular shaped channels,  $500\mu m$  wide and  $350\mu m$  deep, giving a void fraction of 11%. They defined an effective thermal

conductivity as the thermal conductivity of a homogeneous material which would lead to the same temperature field under the same conditions. The measurements indicated that the use of micro heat pipes increases the effective thermal conductivity to about  $200W/mK$ . This represents an increase of about 67% of the thermal conductivity if compared to the empty micro heat pipe array for which the thermal conductivity was determined to be  $120W/mK$ . The results showed that the performance of the micro heat pipe array is favored by decreasing the input heat flux or increasing the coolant temperature.

The research team from the Electrotechnics Laboratory of Grenoble performed experimental and analytical work on flat rectangular micro heat pipes [13], [34], [27]. In their design solution the evaporator (in contact with the electronic device) and the condenser (in contact with a cold plate) were on opposite faces of the heat pipe. The proposed solution was able to work in any position, even against gravity. They analyzed the behavior of the heat spreader with and without working fluid. For the empty device the heat transferred from the hot source to the cold plate was due only to conduction through the heat pipe walls. The same experiment was run with the heat spreader filled with pure water and an optimum liquid charge was found. The results showed that the thermal resistance between the power device and the heat sink can be decreased by about 65% for the heat spreader filled with  $105\mu l$  of pure water compared to the thermal resistance obtained with the same prototype without working fluid. The same team studied the advantages and disadvantages of two-phase micro-channel heat sinks over single-phase micro-channel heat sinks [14]. They found that the pumping power required by the single-phase heat exchangers is 10 times greater than the power necessary for the operation of the two-phase counterparts. The drawbacks of the two-phase heat exchangers were related to the working constraints



such as flow instabilities, local dry-out, critical heat flux and to the insertion of a condenser in the cooling loop.

Suman and Hoda [63] analyzed the sensitivity of a V-shaped micro heat pipe to variations of the thermophysical properties and design parameters. They found that an increase in the apex angle, viscosity, inclination, and length of the heat pipe reduces the performance of the heat pipe. Suman et al [62] studied the performance of micro heat pipes having different polygonal cross sections. They showed that the critical heat input decreases with increasing number of sides for regular polygons, due to an increase in the friction factor and hence a decrease in liquid velocity and capillary pumping capacity. The radius of curvature profile obtained by solving the coupled continuity, momentum, energy, and Laplace-Young equations was used to predict the onset of the dry-out point and the propagation of the dry-out length.

Microjet cooling devices are used as another solution for the thermal management of microelectronic components. Kercher et al. [28] investigated the efficacy of synthetic microjet technology for electronic cooling. Synthetic jets are formed from entrainment and expulsion of the fluid in which they are embedded. The microjet cooling devices in this study consist of a vibrating diaphragm, a diaphragm driver, and a housing with an orifice. When the diaphragm is vibrated by the driver, air is drawn into the housing through the orifice and ejected out from the same orifice, generating a series of vortex rings which propagate away from the orifice. As a result a round turbulent jet is synthesized as these vortex rings interact downstream. The cooling performance of the microjet cooling devices was assessed using a thermal test die consisting of a diode-bridge temperature sensor and a resistive heating element. It was shown that the performance of the microjet cooling

device was strongly dependent on the spacing between the orifice and the thermal die, the maximum cooling performance being achieved for a spacing of  $15\text{mm} - 20\text{mm}$ . They also concluded that the performance increases with increasing membrane resonance frequency and increasing driving power. The influence of the orifice diameter on the performance was also discussed and the  $2.38\text{mm}$  orifice showed the best result, compared to the  $1.98\text{mm}$  and  $2.78\text{mm}$  orifices also used in this analysis. Fabbri and Dhir [11] performed a heat transfer analysis using arrays of microjets which can improve the spatial uniformity of the heat transfer coefficient. Ten different arrays were studied with the jet diameters varying from  $69\mu\text{m}$  to  $250\mu\text{m}$  and the Reynolds number from 73 to 3813. The best performance was achieved using water jets of  $173.6\mu\text{m}$  diameter and  $3\text{mm}$  spacing, impinging at  $12.5\text{m/s}$  on a circular  $19.3\text{mm}$  diameter copper surface.

A brief review of the results obtained by previous investigators on the effect of different geometrical and thermophysical parameters of the heat sinks on their performance is presented in Tables 1.1-1.2. So far only experimental analysis has been done on the amount of working fluid charging the MHP sinks. In this work an analytical methodology is devised for assessing the performance of different configurations of MHP sinks and the amount of liquid charge corresponding to a maximum heat transport capacity of the MHPs.

| Author(s)                    | Heat sink type/<br>Coolant         | Methodology/Results  |
|------------------------------|------------------------------------|--|
| Hingorani et al. (1994)      | Planar spreader                    | -optimum thickness ( $Bi$ and radius given)<br>-optimum radius ( $Bi$ and thickness given)   |
| Peles et al. (2005)          | Micro pin fin heat sink            | -low thermal resistances<br>-flexibility in pin shape selection and spacing  |
| Saha and Acharya (2003)      | Micro pin fin heat sink            | -increase in thermal performance when the flow becomes unsteady  |
| Tuckerman and Pease (1981)   | Micro-channel heat sink/<br>water  | -optimum heat sink design ( $w_{fin}/w_{ch} = 1$ , dissipating $790W/mm^2$ , for $\Delta T = 70^\circ C$ and $\Delta P = 30psi$ )                                      |
| Knight et al. (1992)         | Micro-channel heat sink/<br>air    | -allowed relaxation of the constraints used by Tuckerman and Pease obtaining designs with improved performance   |
| Weisberg et al. (1992)       | Micro-channel heat sink            | -optimum thermal resistance ( $w_{fin}/w_{ch} = 1$ )   |
| Vafai and Zhu (1999)         | 2-layer micro channel<br>heat sink | -reduced undesirable temperature gradients in the streamwise direction   |
| Ambatipudi and Rahman (2000) | Micro-channel heat sink            | - $Nu$ increases with increasing nr. of channels<br>-for $Re = 673$ , maximum $N$ is achieved for a channel depth of $300\mu m$  |
| Ryu et al. (2002)            | Micro-channel heat sink            | -important thermal entrance effect when the working fluid is water ( $Pr \approx 7$ )<br>-thermal resistance increased by 15% when nr. of channels was reduced by half |
| Toh et al. (2002)            | Micro-channel heat sink/<br>water  | -investigated the temperature dependent thermophysical properties  |

Table 1.1: Literature review

| Author(s)                | Heat sink type/<br>Coolant             | Methodology/Results   |
|--------------------------|--|---|
| Zhao and Lu (2002)       | Micro-channel heat sink                | -MHP modeled as lumped capacitance with and effective thermal conductivity $\approx 10$ times that of Si or Cu)   |
| Wu and Cheng (2003)      | Micro-channel heat sink/<br>water      | -convective heat transfer enhanced by increasing the surface hydrophilic capability   |
| Peng and Peterson (2004) | Micro-channel heat sink                | -laminar flow: performance depends upon aspect ratio $H/W$ , $w_{ch}/w_{fin}$<br>-turbulent flow: performance depends on $Z = \min(H, W)/\max(H, W)$ , $Z_{opt} = 0.5$  |
| Chein and Huang (2005)   | Micro-channel heat sink/<br>nanofluids | -increase in thermal conductivity of coolant  |
| Launay et al. (2004)     | MHP sink/ethanol,<br>methanol          | -1 <sup>st</sup> array: 55 triangular channels,<br>230 $\mu m$ wide, 170 $\mu m$ deep<br>-2 <sup>nd</sup> array: 25 triangular channels,<br>342 $\mu m$ deep, with arteries<br>-thermal conductivity of 2 <sup>nd</sup> : 900W/mK<br>-optimum liquid charge for 1 <sup>st</sup> : 24% |
| Suman and Hoda (2005)    | MHP sink/pentane                       | -an increase in the apex angle, viscosity, tilt,<br>and length of MHP reduces the performance   |
| Le Berre et al. (2006)   | MHP sink/methanol                      | -tested a 20mm $\times$ 20mm sink, with 27<br>triangular channels, 500 $\mu m$ wide, 350 $\mu m$ deep<br>-10% volume charge increases the effective<br>thermal conductivity by 67% over<br>the empty MHP array  |

Table 1.2: Literature review cont'd

## CHAPTER 2

### OPTIMAL CONVECTIVE HEAT TRANSFER COEFFICIENT OF A PLANAR SPREADER

#### 2.1 Problem specification

Cooling of electronic devices requires the use of heat spreaders whose function is to allow the spreading of the heat flux lines in the 3-D space and to increase the exchange area with the coolant. This chapter is based on the work performed by Simionescu et al. [60] in which the convective heat transfer coefficient on the bottom surface of a heat spreader corresponding to a maximum heat removal from a heat source placed on the top surface of the heat spreader is estimated (see Figure 2.1).

The elliptic partial differential equation for steady heat transfer is posed in a bounded, 3-D domain  $\Omega = \Omega_c \cup \Omega_s$  of class  $C^{0,1}$  (with a Lipschitz continuous boundary; see [3]). The temperature  $T$  satisfies

$$-\nabla \cdot (k\nabla T) = q_v \quad \text{in } \Omega \quad (2.1)$$

$$\frac{\partial T}{\partial n} \Big|_{\partial\Omega \setminus \Gamma} = 0 \quad (2.2)$$

$$k_s \frac{\partial T}{\partial n} \Big|_{\Gamma} = -h(T|_{\Gamma} - T_{\infty}) \quad (2.3)$$

$$k_c \frac{\partial T_c}{\partial n} \Big|_S = -k_s \frac{\partial T_s}{\partial n} \Big|_S \quad (2.4)$$

$$T_c|_S = T_s|_S, \quad (2.5)$$

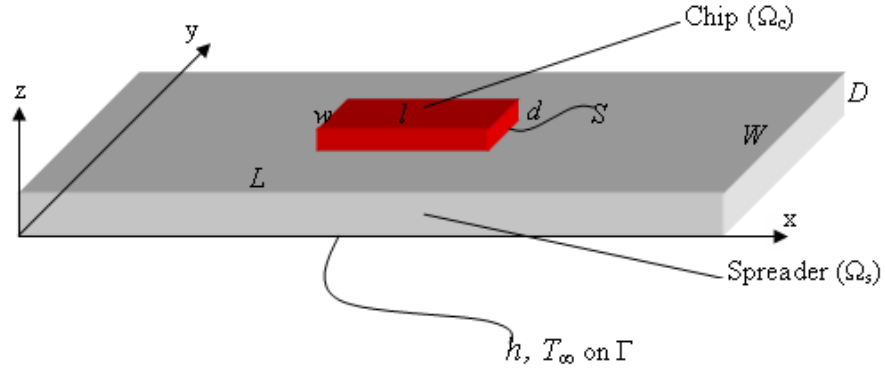


Figure 2.1: Computational domain.

where  $k$  is the coefficient of thermal conductivity defined as:

$$k = \begin{cases} k_c & \text{in } \Omega_c \\ k_s & \text{in } \Omega_s. \end{cases}$$

Here  $\Omega_c$  and  $\Omega_s$  are the subdomains corresponding to the chip and spreader respectively,  $\partial\Omega$  is the boundary,  $n$  is the outward pointing normal vector to the boundary. The temperature in the chip and spreader are  $T_c = T|_{\Omega_c}$  and  $T_s = T|_{\Omega_s}$ , respectively. For simplicity it is assumed that the heat is generated uniformly by a source  $q$  within the chip and is removed from the bottom surface of the heat sink (spreader) by convection, all the other surfaces being insulated. Both the chip and the spreader are isotropic media having the thermal conductivities  $k_c$  and  $k_s$ , respectively. The boundary conditions are of Robin type on  $\Gamma$ , the bottom surface of the spreader, corresponding to Newton's law of cooling, Eq.(2.3), where  $T_\infty$  is the ambient temperature. The boundary conditions on the remaining boundary,  $\partial\Omega \setminus \Gamma$  are of homogeneous Neumann type corresponding to an insulated boundary,

Eq.(2.2). Across the interface  $S$  between the two domains the temperature and heat flux are continuous, Eq.(2.4)–(2.5).

Let  $H^1(\Omega)$  be the usual Sobolev space of square integrable functions whose first distributional derivatives are also square integrable:

$$H^1(\Omega) = \{v: \int_{\Omega} v^2 dx < \infty, \int_{\Omega} |\nabla v|^2 dx < \infty\}, \quad (2.6)$$

equipped with the inner product

$$(u, v)_{H^1(\Omega)} = \int_{\Omega} uv + \nabla u \cdot \nabla v dx, \quad (2.7)$$

and norm

$$\|v\|_{H^1(\Omega)} = (v, v)_{H^1(\Omega)}^{1/2} = \left( \int_{\Omega} v^2 + |\nabla v|^2 dx \right)^{1/2}. \quad (2.8)$$

We also make use of the space of square integrable functions  $L^2(\Omega)$ :

$$L^2(\Omega) = \left\{ v \in \Omega: \int_{\Omega} v^2 dx < \infty \right\}, \quad (2.9)$$

equipped with the inner product

$$(u, v)_{L^2(\Omega)} = \int_{\Omega} uv dx, \quad (2.10)$$

and norm

$$\|v\|_{L^2(\Omega)} = (v, v)_{L^2(\Omega)}^{1/2} = \left( \int_{\Omega} v^2 dx \right)^{1/2}. \quad (2.11)$$

Optimal control techniques have been applied successfully in the field of heat transfer for solving boundary control and parameter estimation problems. Colaço and Orlande [7] estimated the boundary heat fluxes at two surfaces of a cavity, by using simulated temperature measurements taken from its interior. Martin and Dulikravich [43] estimated the convection coefficient using an inverse boundary element method. They used in their approach internal temperature measurements or overspecified boundary conditions on the boundary portion not exposed to convection. Silieti [58] used a genetic algorithm to estimate the heat transfer coefficients. Li and Yan [38] analyzed the unsteady temperature distribution in a turbulent forced convection between parallel plates taking the heat flux applied on the upper wall as the control. Huang and Yeh [25] used the boundary heat flux to control the entrance temperatures of concurrent flows between two adjacent parallel plate channels of a concurrent flow heat exchanger. Another study by Huang and Yeh [24] presents the temperature and moisture distributions inside a porous slab controlled by the convective boundary conditions. The controls are the heat and mass transfer coefficients, respectively. In the paper by Park and Lee [45] two different boundary control problems were analyzed in which the solution of the heat equation was controlled by the boundary temperature and the boundary heat flux, respectively. Lenhart and Wilson [37] studied the optimal control of a heat transfer problem with convective boundary conditions. They focused their efforts on establishing the existence and uniqueness of the solution of the optimality system. The optimal control problem is solved using a conjugate gradient method which consists of the following basic steps [23], [24], [25]:

1. Direct problem formulation
2. Optimal control problem formulation



3. Sensitivity problems formulation
4. Adjoint problems formulation
5. Gradient equations
6. Computational procedure

## 2.2 Existence and uniqueness of solution

We prove the existence and uniqueness of a weak solution to the problem (2.1)-(2.5) by applying the Lax-Milgram lemma (see [3]).

Define  $H$  as:

$$\begin{aligned} H: &= H^1(\Omega_c \cup \Omega_s) \\ &= \{v: v|_{\Omega_c} \in H^1(\Omega_c), v|_{\Omega_s} \in H^1(\Omega_s) \text{ and } \tau(v|_{\Omega_c})|_S = \tau(v|_{\Omega_s})|_S\} \end{aligned}$$

where  $\tau$  is the trace operator (see [3]). To obtain a weak formulation, the differential equation (2.1) is multiplied by  $v \in H$  and then integrated over  $\Omega$ . After applying Green's formula and the corresponding boundary conditions, we get:

$$\begin{aligned} \int_{\Omega} q_v v dx &= \int_{\Omega} -\nabla \cdot (k \nabla T) v dx & (2.12) \\ &= - \int_{\partial\Omega} v k \frac{\partial T}{\partial n} ds + \int_{\Omega} k \nabla T \cdot \nabla v dx \\ &= - \int_{\partial\Omega \setminus \Gamma} v k \frac{\partial T}{\partial n} ds - \int_{\Gamma} v k_s \frac{\partial T}{\partial n} ds + \int_{\Omega} k \nabla T \cdot \nabla v dx \\ &= \int_{\Gamma} h(T - T_{\infty}) v ds + \int_{\Omega} k \nabla T \cdot \nabla v dx. \end{aligned}$$

Define the linear form:

$$L(v) = \int_{\Omega} q_v v dx + \int_{\Gamma} h T_{\infty} v ds \quad (2.13)$$

and the bilinear form,

$$a(T, v) = \int_{\Gamma} h T v ds + \int_{\Omega} k \nabla T \cdot \nabla v dx. \quad (2.14)$$

For our particular problem  $q_v = \text{const}$  for  $x \in \Omega_c$  and  $q_v = 0$  for  $x \in \Omega_s$ . Now the weak form of problem (2.1)-(2.5) can be written as: Find  $T \in H$  such that

$$a(T, v) = L(v) \quad \forall v \in H. \quad (2.15)$$

Obviously,  $L: H \rightarrow \mathbf{R}$  is a continuous, linear form and  $a: H \times H \rightarrow \mathbf{R}$  is a symmetric, continuous, and coercive bilinear form, i.e. there exist positive constants  $K_1, K_2, K_3$  such that:

$$|L(v)| \leq K_1 \|v\|_{H(\Omega)} \quad \forall v \in H$$

$$|a(u, v)| \leq K_2 \|u\|_{H(\Omega)} \|v\|_{H(\Omega)} \quad \forall u, v \in H$$

$$K_3 \|v\|_{H(\Omega)}^2 \leq a(v, v) \quad \forall v \in H.$$

Hence the Lax-Milgram lemma guarantees the existence and uniqueness of a weak solution to problem (2.1)-(2.5) (see [3]).

### 2.3 Optimal control for model problem

We now show the existence and uniqueness of an optimal control and describe a conjugate gradient algorithm which can be used to approximate solutions of the optimal control

problem. The conjugate gradient algorithm requires the solution of three coupled problems, the direct problem, sensitivity problem and adjoint problem. We consider a model problem with a rectangular chip and rectangular heat spreader (see Figure 2.1).

### 2.3.1 The direct problem

The governing heat equation and the corresponding boundary conditions (2.1)-(2.5) for both the chip and the spreader, which are in thermal contact represent the direct problem. The two domains are made from materials with different thermophysical properties. The only heat source is within the chip.

The following dimensionless variables are introduced:

$$T_c \rightarrow \frac{T_c - T_\infty}{q_v D_s^2 / k_s} \quad T_s \rightarrow \frac{T_s - T_\infty}{q_v D_s^2 / k_s} \quad x \rightarrow \frac{x}{D_s} \quad y \rightarrow \frac{y}{D_s} \quad z \rightarrow \frac{z}{D_s}.$$

Dimensionless heat equations in the chip ( $\Omega_c$ ) and the in the heat sink ( $\Omega_s$ ) are respectively:

$$\frac{\partial^2 T_c}{\partial x^2} + \frac{\partial^2 T_c}{\partial y^2} + \frac{\partial^2 T_c}{\partial z^2} = -\frac{k_s}{k_c} \quad (2.16)$$

and

$$\frac{\partial^2 T_s}{\partial x^2} + \frac{\partial^2 T_s}{\partial y^2} + \frac{\partial^2 T_s}{\partial z^2} = 0 \quad (2.17)$$

subject to the following boundary conditions:

$$\left. \frac{\partial T_c}{\partial x} \right|_{x=\frac{L_s - l_c}{2}} = 0 \quad \left. \frac{\partial T_c}{\partial x} \right|_{x=\frac{L_s + l_c}{2}} = 0 \quad (2.18)$$

$$\left. \frac{\partial T_c}{\partial y} \right|_{y=\frac{W_s - w_c}{2}} = 0 \quad \left. \frac{\partial T_c}{\partial y} \right|_{y=\frac{W_s + w_c}{2}} = 0 \quad (2.19)$$

$$\left. \frac{\partial T_s}{\partial x} \right|_{x=0} = 0 \quad \left. \frac{\partial T_s}{\partial x} \right|_{x=L_s} = 0 \quad (2.20)$$

$$\left. \frac{\partial T_s}{\partial y} \right|_{y=0} = 0 \quad \left. \frac{\partial T_s}{\partial y} \right|_{y=W_s} = 0 \quad (2.21)$$

$$\left. \frac{\partial T_c}{\partial z} \right|_{z=1+d_c} = 0 \quad \left. \frac{\partial T_s}{\partial z} \right|_{z=0} = Bi T_s|_{z=0} \quad (2.22)$$

and the conditions of temperature and flux continuity at the interface:

$$T_c|_{z=1} = T_s|_{z=1} \quad \left. \frac{\partial T_s}{\partial z} \right|_{z=1} = \begin{cases} \frac{k_c}{k_s} \left. \frac{\partial T_c}{\partial z} \right|_{z=1} & \text{if } \begin{cases} \frac{L_s-l_c}{2} \leq x \leq \frac{L_s+l_c}{2} \\ \frac{W_s-w_c}{2} \leq y \leq \frac{W_s+w_c}{2} \end{cases} \\ 0 & \text{otherwise.} \end{cases} \quad (2.23)$$

Here  $Bi = hD_s/k_s$  is the Biot number which measures the ratio of conductive to convective heat transfer resistance and represents the control variable.

The direct problem is solved using a finite difference scheme for an initial guess of the control variable  $Bi$ .

### 2.3.2 The optimal control problem

In the optimal control problem, the optimal control  $Bi(x, y)$  is the unknown, and the equations (2.16)-(2.23) represent constraints that have to be satisfied. The goal is to find an optimal control that will maximize the amount of heat removed from the chip. This

statement is equivalent to minimizing the following functional:

$$J = \int_{\frac{L-l}{2}}^{\frac{L_s+l_c}{2}} \int_{\frac{W_s-w_c}{2}}^{\frac{W_s+w_c}{2}} \int_1^{1+d_c} T_c^2(x, y, z) dx dy dz + \frac{\alpha}{2} \int_0^{L_s} \int_0^{W_s} Bi^2(x, y) dx dy \quad (2.24)$$

where  $T_c$  is the computed temperature within the chip subject to the constraints (2.16)-(2.23) and  $\alpha$  is a weighting coefficient penalizing the control function. The goal of optimization is to minimize the first term appearing in the definition of the functional  $J$ . The second term is added to account for the *cost* of the control. The nonnegative penalty parameter  $\alpha$  can be used to change the relative importance of the second term in Eq.(3.50). The squares of the integrands guarantee the existence of a minimum. Note that ideally  $T_c$  should be 0, in which case the chip temperature is equal to the ambient temperature.

### 2.3.3 Existence and uniqueness of an optimal control

In proving the existence and uniqueness of a solution to the optimal control problem we follow the procedure presented by Lions [40], De los Reyes [42], and Gunzburger and Lee [16].

Define  $U_{ad} := \{Bi \in L^2(\Gamma)\}$  as the set of admissible controls which is obviously not empty. We want to prove the existence and uniqueness of a pair  $(T^*, Bi^*) \in H \times U_{ad}$  that minimizes the functional  $J$ , subject to equations (2.16)-(2.23).

Consider a minimizing sequence  $\{(T_n, Bi_n)\}$  such that

$$J(T_n, Bi_n) \longrightarrow \inf_{(T, Bi) \in H \times U_{ad}} J(T, Bi) \quad (2.25)$$

along with the weak formulation:

$$a(T_n, v) = L(v) \quad \forall v \in H(\Omega). \quad (2.26)$$

From the definition of  $J$  we have  $\frac{\alpha}{2} \|Bi_n\|_{L^2(\Gamma)}^2 \leq J(T_n, Bi_n) < \infty$ , which implies that  $Bi_n$  is bounded. From the coercivity of the bilinear form  $a$  and continuity of the linear form  $L$ ,  $T_n$  is also bounded. So we may extract subsequences such that  $Bi_n \rightharpoonup Bi^*$  weakly in  $L^2(\Gamma)$ ,  $T_n \rightharpoonup T^*$  weakly in  $H(\Omega)$ ,  $T_n \rightarrow T^*$  strongly in  $L^2(\Omega)$  for some  $(T^*, Bi^*) \in H(\Omega) \times L^2(\Gamma)$ . The last convergence follows from the compact embedding  $H(\Omega) \hookrightarrow L^2(\Omega)$ . Now by the weak lower semicontinuity of  $J$  we conclude that  $(T^*, Bi^*)$  is an optimal solution, i.e.

$$J(T^*, Bi^*) = \inf_{(T, Bi) \in H \times U_{ad}} J(T, Bi). \quad (2.27)$$

Thus we have shown that the optimal control exists. The uniqueness of the optimal solution follows from the convexity of the functional  $J$ .

### 2.3.4 Conjugate gradient algorithm

A minimizing sequence is constructed using the conjugate gradient method and the following iterative scheme (see [6]):

$$Bi^{(n+1)} = Bi^{(n)} - \beta^{(n)} P^{(n)} \quad (2.28)$$

where  $\beta^{(n)}$  is the step size and  $P^{(n)}$  is the search direction which is determined from:

$$P^{(n)} = \nabla J^{(n)} + \gamma^{(n)} P^{(n-1)}. \quad (2.29)$$

The conjugate coefficient  $\gamma^{(n)}$  is given by:

$$\gamma^{(n)} = \frac{\int_0^{L_s} \int_0^{W_s} |\nabla J^{(n)}(x, y)|^2 dx dy}{\int_0^{L_s} \int_0^{W_s} |\nabla J^{(n-1)}(x, y)|^2 dx dy} \quad \text{with} \quad \gamma^{(0)} = 0. \quad (2.30)$$

The iterative process described by Eq. (2.28)–(2.30) requires the step size  $\beta^{(n)}$  and the gradient of the functional,  $\nabla J^{(n)}$ . These parameters will be computed from the sensitivity and adjoint problem, respectively.

### 2.3.5 Sensitivity problem and calculation of the search step size

When the control  $Bi(x, y)$  undergoes a small perturbation  $\Delta Bi(x, y)$ , the temperatures within the chip and spreader are varied by  $\Delta T_c(x, y, z)$  and  $\Delta T_s(x, y, z)$  respectively. If we replace  $T_c$  in the direct problem (2.1)–(2.5) by  $T_c + \Delta T_c$ ,  $T_s$  by  $T_s + \Delta T_s$  and  $Bi$  by  $Bi + \Delta Bi$  and then from the resulting equations subtract the equations describing the direct problem the following sensitivity problem is obtained when the second order terms are neglected:

$$\frac{\partial^2 \Delta T_c}{\partial x^2} + \frac{\partial^2 \Delta T_c}{\partial y^2} + \frac{\partial^2 \Delta T_c}{\partial z^2} = 0 \quad (2.31)$$

$$\frac{\partial^2 \Delta T_s}{\partial x^2} + \frac{\partial^2 \Delta T_s}{\partial y^2} + \frac{\partial^2 \Delta T_s}{\partial z^2} = 0 \quad (2.32)$$

$$\left. \frac{\partial \Delta T_c}{\partial x} \right|_{x=\frac{L_s-l_c}{2}} = 0 \quad \left. \frac{\partial \Delta T_c}{\partial x} \right|_{x=\frac{L_s+l_c}{2}} = 0 \quad (2.33)$$

$$\left. \frac{\partial \Delta T_c}{\partial y} \right|_{y=\frac{W_s-w_c}{2}} = 0 \quad \left. \frac{\partial \Delta T_c}{\partial y} \right|_{y=\frac{W_s+w_c}{2}} = 0 \quad (2.34)$$

$$\left. \frac{\partial \Delta T_s}{\partial x} \right|_{x=0} = 0 \quad \left. \frac{\partial \Delta T_s}{\partial x} \right|_{x=L_s} = 0 \quad (2.35)$$

$$\left. \frac{\partial \Delta T_s}{\partial y} \right|_{y=0} = 0 \qquad \left. \frac{\partial \Delta T_s}{\partial y} \right|_{y=W_s} = 0 \qquad (2.36)$$

$$\left. \frac{\partial \Delta T_c}{\partial z} \right|_{z=1+d_c} = 0 \qquad \left. \frac{\partial \Delta T_s}{\partial z} \right|_{z=0} = Bi \Delta T_s|_{z=0} + \Delta Bi T_s|_{z=0} \qquad (2.37)$$

and the conditions of temperature and flux continuity at the interface:

$$\Delta T_c|_{z=1} = \Delta T_s|_{z=1}$$

$$\left. \frac{\partial \Delta T_s}{\partial z} \right|_{z=1} = \begin{cases} \frac{k_c}{k_s} \left. \frac{\partial \Delta T_c}{\partial z} \right|_{z=1} & \text{if } \begin{cases} \frac{L_s - l_c}{2} \leq x \leq \frac{L_s + l_c}{2} \\ \frac{W_s - w_c}{2} \leq y \leq \frac{W_s + w_c}{2} \end{cases} \\ 0 & \text{otherwise} \end{cases} \qquad (2.38)$$

where  $\Delta T_c(x, y, z)$  and  $\Delta T_s(x, y, z)$  represent the sensitivity functions. The functional  $J^{(n+1)}$  for the  $(n+1)$ th iteration is written by replacing  $Bi^{(n+1)}$  with the expression given by Eq. (2.28):

$$\begin{aligned} J^{(n+1)} &= \int_{\frac{L_s - l_c}{2}}^{\frac{L_s + l_c}{2}} \int_{\frac{W_s - w_c}{2}}^{\frac{W_s + w_c}{2}} \int_1^{1+d_c} T_c^2(x, y, z, Bi^{(n)} - \beta^{(n)} P^{(n)}) dx dy dz \\ &+ \frac{\alpha}{2} \int_0^{L_s} \int_0^{W_s} (Bi^{(n)} - \beta^{(n)} P^{(n)})^2 dx dy. \end{aligned} \qquad (2.39)$$

Here  $Bi^{(n+1)}$  is a parameter. In the above and following equation we abuse notation by adding a variable to  $T_c$  to emphasize its dependence on the control. Using a Taylor series expansion for  $T_c(x, y, z, Bi^{(n)} - \beta^{(n)} P^{(n)})$ , the following expression is obtained for the



functional  $J$  at the  $(n + 1)$ th iteration:

$$\begin{aligned}
J^{(n+1)} &= \int_{\frac{L_s-l_c}{2}}^{\frac{L_s+l_c}{2}} \int_{\frac{W_s-w_c}{2}}^{\frac{W_s+w_c}{2}} \int_1^{1+d_c} [T_c(x, y, z, Bi^{(n)}) - \beta^{(n)} \Delta T_c(P^{(n)})]^2 dx dy dz \\
&+ \frac{\alpha}{2} \int_0^{L_s} \int_0^{W_s} (Bi^{(n)} - \beta^{(n)} P^{(n)})^2 dx dy.
\end{aligned} \tag{2.40}$$

In the above equation  $T_c$  is the temperature distribution within the chip obtained by solving the direct problem (2.16)-(2.23) using an initial guess of the control  $Bi$ , while  $\Delta T_c$  is one of the sensitivity functions obtained from the solution of the sensitivity problem (2.31)-(2.38). The search step size  $\beta^{(n)}$  is obtained from the line search at each iteration by taking the derivative of Eq. (2.40) with respect to  $\beta^{(n)}$  and equating to 0:

$$\beta^{(n)} = \frac{\int_{\frac{L_s-l_c}{2}}^{\frac{L_s+l_c}{2}} \int_{\frac{W_s-w_c}{2}}^{\frac{W_s+w_c}{2}} \int_1^{1+d_s} 2T_c(Bi^{(n)}) \Delta T_c(P^{(n)}) dx dy dz + \alpha \int_0^{L_s} \int_0^{W_s} Bi^{(n)} P^{(n)} dx dy}{\int_{\frac{L_s-l_c}{2}}^{\frac{L_s+l_c}{2}} \int_{\frac{W_s-w_c}{2}}^{\frac{W_s+w_c}{2}} \int_1^{1+d_c} 2\Delta T_c^2(P^{(n)}) dx dy dz + \alpha \int_0^{L_s} \int_0^{W_s} (P^{(n)})^2 dx dy}. \tag{2.41}$$

### 2.3.6 The adjoint problem

The adjoint problem is obtained by multiplying Eq. (2.16) and Eq. (2.17) by the Lagrange multipliers  $\zeta_1(x, y, z)$  and  $\zeta_2(x, y, z)$ , respectively (see [6]). The obtained equations are integrated over the specified domains and the integrals are added to the functional  $J$ :

$$\begin{aligned}
J &= \int_{\frac{L_s-l_c}{2}}^{\frac{L_s+l_c}{2}} \int_{\frac{W_s-w_c}{2}}^{\frac{W_s+w_c}{2}} \int_1^{1+d_c} T_c^2 dx dy dz + \frac{\alpha}{2} \int_0^{L_s} \int_0^{W_s} Bi^2 dx dy \\
&+ \int_{\frac{L_s-l_c}{2}}^{\frac{L_s+l_c}{2}} \int_{\frac{W_s-w_c}{2}}^{\frac{W_s+w_c}{2}} \int_1^{1+d_c} \zeta_1 \left( \frac{\partial^2 T_c}{\partial x^2} + \frac{\partial^2 T_c}{\partial y^2} + \frac{\partial^2 T_c}{\partial z^2} + \frac{k_s}{k_c} \right) dx dy dz \\
&+ \int_0^{L_s} \int_0^{W_s} \int_0^1 \zeta_2 \left( \frac{\partial^2 T_s}{\partial x^2} + \frac{\partial^2 T_s}{\partial y^2} + \frac{\partial^2 T_s}{\partial z^2} \right) dx dy dz.
\end{aligned} \tag{2.42}$$

To obtain the variation  $\Delta J$  we need to calculate  $J|_{Bi+\Delta Bi} - J|_{Bi}$  where  $J|_{Bi+\Delta Bi}$  is found by replacing  $T_c$  by  $T_c + \Delta T_c$ ,  $T_s$  by  $T_s + \Delta T_s$  and  $Bi$  by  $Bi + \Delta Bi$  in Eq. (2.42) and then subtracting from the resulting expression the right hand side of Eq. (2.42):

$$\begin{aligned}
\Delta J|_{Bi} &= \int_{\frac{L_s-l_c}{2}}^{\frac{L_s+l_c}{2}} \int_{\frac{W_s-w_c}{2}}^{\frac{W_s+w_c}{2}} \int_1^{1+d_c} 2T_c \Delta T_c dx dy dz + \alpha \int_0^{L_s} \int_0^{W_s} Bi \Delta Bi dx dy \\
&+ \int_{\frac{L_s-l_c}{2}}^{\frac{L_s+l_c}{2}} \int_{\frac{W_s-w_c}{2}}^{\frac{W_s+w_c}{2}} \int_1^{1+d_c} \zeta_1 \left( \frac{\partial^2 \Delta T_c}{\partial x^2} + \frac{\partial^2 \Delta T_c}{\partial y^2} + \frac{\partial^2 \Delta T_c}{\partial z^2} + \frac{k_s}{k_c} \right) dx dy dz \\
&+ \int_0^{L_s} \int_0^{W_s} \int_0^1 \zeta_2 \left( \frac{\partial^2 \Delta T_s}{\partial x^2} + \frac{\partial^2 \Delta T_s}{\partial y^2} + \frac{\partial^2 \Delta T_s}{\partial z^2} \right) dx dy dz. \tag{2.43}
\end{aligned}$$

Integrating Eq.(2.43) by parts and applying the boundary conditions of the sensitivity problem the following adjoint problem is obtained:

$$\frac{\partial^2 \zeta_1}{\partial x^2} + \frac{\partial^2 \zeta_1}{\partial y^2} + \frac{\partial^2 \zeta_1}{\partial z^2} + 2T_c = 0 \tag{2.44}$$

$$\frac{\partial^2 \zeta_2}{\partial x^2} + \frac{\partial^2 \zeta_2}{\partial y^2} + \frac{\partial^2 \zeta_2}{\partial z^2} = 0 \tag{2.45}$$

$$\frac{\partial \zeta_1}{\partial x} \Big|_{x=\frac{L_s-l_c}{2}} = 0 \qquad \frac{\partial \zeta_1}{\partial x} \Big|_{x=\frac{L_s+l_c}{2}} = 0 \tag{2.46}$$

$$\frac{\partial \zeta_1}{\partial y} \Big|_{y=\frac{W_s-w_c}{2}} = 0 \qquad \frac{\partial \zeta_1}{\partial y} \Big|_{y=\frac{W_s+w_c}{2}} = 0 \tag{2.47}$$

$$\frac{\partial \zeta_2}{\partial x} \Big|_{x=0} = 0 \qquad \frac{\partial \zeta_2}{\partial x} \Big|_{x=L} = 0 \tag{2.48}$$

$$\frac{\partial \zeta_2}{\partial y} \Big|_{y=0} = 0 \qquad \frac{\partial \zeta_2}{\partial y} \Big|_{y=W} = 0 \tag{2.49}$$

$$\frac{\partial \zeta_1}{\partial z} \Big|_{z=1+d_c} = 0 \qquad \frac{\partial \zeta_2}{\partial z} \Big|_{z=0} = Bi \zeta_2|_{z=0} \tag{2.50}$$

$$\zeta_1|_{z=1} = \frac{k_c}{k_s} \zeta_2|_{z=1} \quad \frac{\partial \zeta_2}{\partial z} \Big|_{z=1} = \begin{cases} \frac{\partial \zeta_1}{\partial z} \Big|_{z=1} & \text{if } \begin{cases} \frac{L_s - l_c}{2} \leq x \leq \frac{L_s + l_c}{2} \\ \frac{W_s - w_c}{2} \leq y \leq \frac{W_s + w_c}{2} \end{cases} \\ 0 & \text{otherwise.} \end{cases} \quad (2.51)$$

The following integral is left after performing the integration by parts in Eq. (2.43) and identifying the adjoint problem:

$$\Delta J|_{Bi} = \int_0^{L_s} \int_0^{W_s} (\alpha Bi - \zeta_2(x, y, 0) T_s(x, y, 0)) \Delta Bi dx dy. \quad (2.52)$$

By the definition given in [1], the functional increment at  $Bi(x, y)$  can be written as:

$$\Delta J|_{Bi} = \int_0^{L_s} \int_0^{W_s} \nabla J \Delta Bi dx dy. \quad (2.53)$$

Hence we obtain the following expression for the gradient:

$$\nabla J = \alpha Bi - \zeta_2(x, y, 0) T_s(x, y, 0). \quad (2.54)$$

### 2.3.7 Computational algorithm

The computational procedure for the solution of this problem may be summarized as follows:

*step 1* Solve the direct problem given by Eq. (2.16)–(2.23) to obtain  $T_c$  and  $T_s$  for an initial guess of the control  $Bi$ ;

- step 2* Solve the adjoint problem given by Eq. (2.44)–(2.51) to obtain  $\zeta_1$  and  $\zeta_2$ ;
- step 3* Compute the gradient of the functional  $\nabla J$  from Eq. (2.54);
- step 4* Compute the conjugate coefficient  $\gamma^{(n)}$  from Eq. (2.30) and the search direction  $P^{(n)}$  from Eq. (2.29);
- step 5* Set  $\Delta Bi(x, y) = P^{(n)}(x, y)$  and solve the sensitivity problem given by Eq. (2.31)–(2.38) to obtain  $\Delta T_c$  and  $\Delta T_s$  respectively;
- step 6* Compute the search step size  $\beta^{(n)}$  from Eq. (2.41);
- step 7* Compute the new estimate for  $Bi$  from Eq. (2.28) and go back to *step 1* until a stopping criterion is achieved. The stopping criterion for our numerical experiments was chosen as  $\|Bi^{(n+1)} - Bi^{(n)}\| \leq \epsilon$ , where  $\epsilon$  is a prescribed tolerance which was set in our experiments to  $10^{-6}$ .

## 2.4 Implementation and numerical procedure

A finite difference scheme was implemented to solve the direct, sensitivity, and adjoint problems. The centered approximation for the derivatives was used leading to the following discrete heat transfer equations for the direct problem:

$$\begin{aligned} \frac{T_c^{i-1,j,k} - 2T_c^{i,j,k} + T_c^{i+1,j,k}}{\Delta x^2} &+ \frac{T_c^{i,j-1,k} - 2T_c^{i,j,k} + T_c^{i,j+1,k}}{\Delta y^2} \\ &+ \frac{T_c^{i,j,k-1} - 2T_c^{i,j,k} + T_c^{i,j,k+1}}{\Delta z^2} = -\frac{k_s}{k_c} \end{aligned}$$

$$\begin{aligned} & \frac{T_s^{i-1,j,k} - 2T_s^{i,j,k} + T_s^{i+1,j,k}}{\Delta x^2} + \frac{T_s^{i,j-1,k} - 2T_s^{i,j,k} + T_s^{i,j+1,k}}{\Delta y^2} \\ & + \frac{T_s^{i,j,k-1} - 2T_s^{i,j,k} + T_s^{i,j,k+1}}{\Delta z^2} = 0 \end{aligned}$$

$$\begin{aligned} \text{at } x = 0 & \quad T_s^{0,j,k} = T_s^{2,j,k} \\ \text{at } x = L_s & \quad T_s^{m-1,j,k} = T_s^{m+1,j,k} \\ \text{at } y = 0 & \quad T_s^{i,0,k} = T_s^{i,2,k} \\ \text{at } y = W_s & \quad T_s^{i,n-1,k} = T_s^{i,n+1,k} \\ \text{at } z = 0 & \quad \frac{T_s^{i,j,0} - T_s^{i,j,2}}{2\Delta z} = Bi T_s^{i,j,1} \\ \text{at } z = 1 & \quad T_s^{i,j,p} = T_c^{i,j,p} \\ & \quad T_s^{i,j,p-1} - T_s^{i,j,p+1} = \frac{k_c}{k_s} (T_c^{i,j,p-1} - T_c^{i,j,p+1}) \\ \text{at } x = \frac{L_s - l_c}{2} & \quad T_c^{\frac{m-m_0}{2},j,k} = T_c^{\frac{m-m_0}{2}+2,j,k} \\ \text{at } x = \frac{L_s + l_c}{2} & \quad T_c^{\frac{m+m_0}{2}-1,j,k} = T_c^{\frac{m+m_0}{2}+1,j,k} \\ \text{at } x = \frac{W_s - w_c}{2} & \quad T_c^{i,\frac{n-n_0}{2},k} = T_c^{i,\frac{n-n_0}{2}+2,k} \\ \text{at } x = \frac{W_s + w_c}{2} & \quad T_c^{i,\frac{n+n_0}{2}-1,k} = T_c^{i,\frac{n+n_0}{2}+1,k} \\ \text{at } z = 1 + d_c & \quad T_c^{i,j,p+p_0-1} = T_c^{i,j,p+p_0+1} \end{aligned}$$

where  $T_s^{i,j,k}$  and  $T_c^{i,j,k}$  represent the spreader and chip temperature, respectively corresponding to the  $(i, j, k)$  location of the mesh,  $m, n, p$ , represent the number of grid points in  $x, y$ , and  $z$  direction in the spreader and  $m_0, n_0, p_0$ , represent the number of grid points in  $x, y$ , and  $z$  direction in the chip. The step sizes for the two domains have the same values.

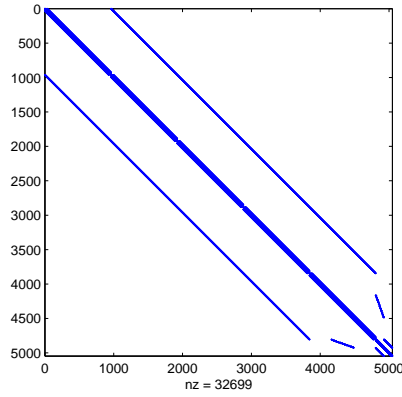


Figure 2.2: Structure of matrix  $\mathbf{A}$ .

The discretization yields a linear system of equations:

$$A\mathbf{T} = \mathbf{b}.$$

Here  $A$  is a  $d \times d$  matrix having the banded structure presented in Figure 2.2, where  $d = (m + 1)(n + 1)(p + 1) + (m_0 + 1)(n_0 + 1)p_0$ ,  $\mathbf{T}$  is the  $d$  vector of the temperatures at the grid points and  $\mathbf{b}$  is the  $d$  vector of the free terms corresponding to the heat source component. Similar discretizations were used for the sensitivity and adjoint problems. A Matlab code was implemented to solve the three coupled problems, using a mesh of  $31 \times 31 \times 5$  points for the spreader and  $11 \times 11 \times 4$  points for the chip.

## 2.5 Results and discussions

We now present some simulation results. Parameter values that were used in the simulation were:

- volumetric heat source:  $q_v = 144 \text{ W/mm}^3$

- heat source (chip) dimensions:  $3mm \times 3mm \times 0.15mm$
- heat sink (spreader) dimensions:  $9mm \times 9mm \times 0.3mm$
- chip thermal conductivity:  $k_c = 0.1 \text{ W/mmK}$
- spreader thermal conductivity:  $k_s = 0.1412 \text{ W/mmK}$

These values are typical of the ones for applications we have in mind. The controlled and uncontrolled solutions for the temperature distributions are compared for different values of  $\alpha$ . The uncontrolled solution is obtained by solving the direct problem presented in section 2.3.1 with a constant Biot number over the entire surface  $\Gamma$ . The value used in each case (for each value of the parameter  $\alpha$ ) would give the same cost as the cost of the optimal  $Bi$ . The distribution of the temperature difference  $T - T_\infty$  at the interface between the chip and spreader for the controlled case is lower and displays a flatter profile than the uncontrolled solution as we can see in Figure 4.1. We see that the difference between the two distributions increases with increasing penalty parameter  $\alpha$  (increasing the *cost* of the control). Small variations of the penalty parameter  $\alpha$  introduce significant variations of the temperature distribution inside the domain. The greater the value assigned to  $\alpha$  the larger the *cost* of employing a control, resulting in a smaller  $Bi$  hence a smaller contribution of convective cooling.

Figure 4.2 shows distributions of the Biot number for different values of the penalty parameter,  $\alpha = 0.1, 0.5, 1, 5, 50$ . The corresponding distributions of the temperature difference at the chip-spreader interface are presented in Figure 4.3. The profile of  $Bi$  resembles the temperature profile at any horizontal cross section through the spreader. The smaller the penalty parameter  $\alpha$ , the higher the Biot number and the lower the domain temperature.

The temperature of the hottest point, which is the center of the chip's upper face, corresponding to  $\alpha = 50$  is approximately  $50K$  higher than the one corresponding to  $\alpha = 0.1$ . These temperatures are approximately  $150K$  and  $50K$  lower than the uncontrolled temperatures, respectively.

Contour plots of the temperature distributions, through a vertical symmetry plane are presented in Figure 4.4 and show that the temperature difference between the hottest and coolest point increases with increasing  $\alpha$  and the contour curves are flatter for small values of  $\alpha$ .



## CHAPTER 3

### OPTIMAL DESIGN OF A MICRO HEAT PIPE

#### 3.1 Problem specification

In this chapter the analysis is extended to heat sinks equipped with micro heat pipes. The objective of this analysis is to estimate the geometry of a micro heat pipe (MHP) and the amount of cooling fluid inside the pipes that will maximize the heat removed from a heat source placed on the top surface of the heat sink (see Figure 3.1). Micro heat pipes are small sealed devices filled with a working fluid whose phase change is used to transfer thermal energy. A single micro heat pipe consists of a small non circular channel that uses the sharp angled corners as liquid arteries. The vaporization-condensation process causes the liquid-vapor interface to change along the pipe, resulting in a capillary pressure difference. The capillary pumping pressure drives the liquid from the condenser back to evaporator.

An optimal control technique similar to that presented in chapter 2 is used to solve two problems. In the first problem the solution of the heat equation is controlled by the convective boundary condition taking the Biot number and the geometrical parameters of the channel as controls. In the second problem an optimal  $Bi$  number distribution corresponding to the MHP maximum heat transport capacity is found. The optimal heat transfer coefficient can be obtained by prescribing the height and width of the channels, the number of channels, and the amount of working fluid that charges the channels. The importance of the channel geometry on the performance of a heat sink was pointed out by many previous investigators as presented in chapter 1. Only experimental work was done to study the influence of liquid charge on the performance of MHP sinks [36] and it was

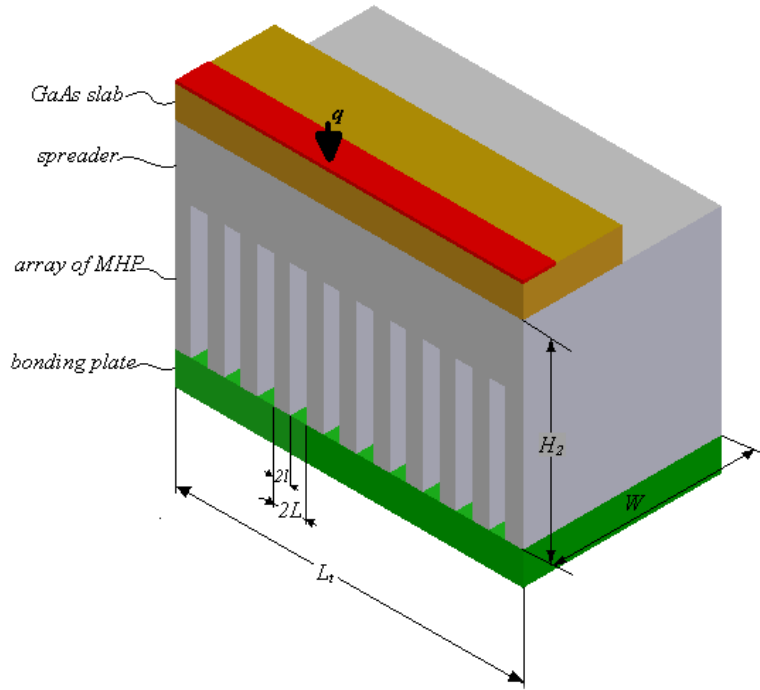


Figure 3.1: Schematic of a MHP sink.

shown that a too large amount of fluid leads to a condenser flooding, while a too low fluid charge leads to an evaporator dry-out and an increase in channel wall temperature.

### 3.2 The direct problem

#### 3.2.1 Heat transfer equations corresponding to the GaAs slab and silicon wafer

In this analysis the silicon wafer dimensions are constant and all the channels have a uniform rectangular cross section of width  $2l$  and height  $H_1$ . A constant heat flux  $q$  is supplied to a GaAs substrate through a  $L_t \times w_2$  heating area. The GaAs slab of width  $L_t$ , length  $w_1$ , and height  $H_3$  is placed on the top of the silicon wafer, covering the evaporator area of the micro heat pipes. Taking advantage of symmetry we consider the analysis of a cell consisting of half of the channel and half of the separating fin, see Figure 3.2.

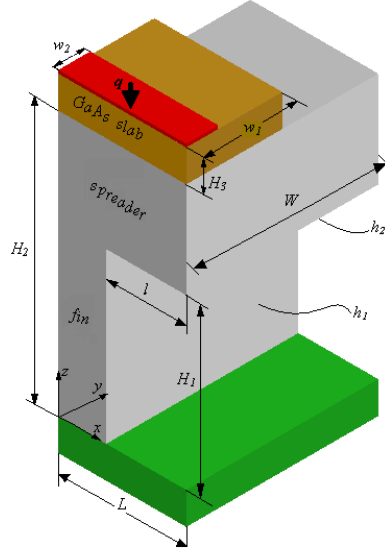


Figure 3.2: Computational domain.

The heat transfer equations and the corresponding boundary conditions are written for each subdomain depicted in Figure 3.2, i.e. GaAs slab, spreader, and fin. It is assumed that the heat entering through the  $L_t \times w_2$  heating area it is removed only from the channel surface through the evaporator area of the MHP, all the other surfaces being insulated. The dimensionless mathematical formulation of the heat conduction through the GaAs slab, silicon substrate, and fin is obtained by introducing the following dimensionless variables:

$$\bar{T}_A \rightarrow \frac{T_A - T_f}{qH_2/k_{Si}} \quad \bar{T}_B \rightarrow \frac{T_B - T_f}{qH_2/k_{Si}} \quad \bar{T}_C \rightarrow \frac{T_C - T_f}{qH_2/k_{Si}} \quad \bar{x} \rightarrow \frac{x}{H_2} \quad \bar{y} \rightarrow \frac{y}{H_2} \quad \bar{z} \rightarrow \frac{z}{H_2}.$$

Here  $T_A, T_B, T_C, T_f$  are the temperatures corresponding to the GaAs slab, silicon substrate, fin, and cooling fluid respectively,  $q$  is the heat flux entering the heat sink,  $k_{Si}$  is the coefficient of thermal conductivity for silicon, and the reference length  $H_2$  is the thickness of the silicon wafer. In what follows it is understood that all quantities - unless specified

otherwise - are in dimensionless form. The governing equations are:

$$\frac{\partial^2 T_A}{\partial x^2} + \frac{\partial^2 T_A}{\partial y^2} + \frac{\partial^2 T_A}{\partial z^2} = 0 \quad (3.1)$$

$$\frac{\partial^2 T_B}{\partial x^2} + \frac{\partial^2 T_B}{\partial y^2} + \frac{\partial^2 T_B}{\partial z^2} = 0 \quad (3.2)$$

$$\frac{\partial^2 T_C}{\partial x^2} + \frac{\partial^2 T_C}{\partial y^2} + \frac{\partial^2 T_C}{\partial z^2} = 0 \quad (3.3)$$

subject to the following boundary conditions:

$$\left. \frac{\partial T_A}{\partial x} \right|_{x=0} = 0 \quad \left. \frac{\partial T_A}{\partial x} \right|_{x=L} = 0 \quad (3.4)$$

$$\left. \frac{\partial T_A}{\partial y} \right|_{y=0} = 0 \quad \left. \frac{\partial T_A}{\partial y} \right|_{y=w_1} = 0 \quad (3.5)$$

$$\left. \frac{\partial T_B}{\partial x} \right|_{x=0} = 0 \quad \left. \frac{\partial T_B}{\partial x} \right|_{x=L-l} = 0 \quad (3.6)$$

$$\left. \frac{\partial T_B}{\partial y} \right|_{y=0} = 0 \quad \left. \frac{\partial T_B}{\partial y} \right|_{y=W} = 0 \quad (3.7)$$

$$\left. \frac{\partial T_C}{\partial x} \right|_{x=0} = 0 \quad \left. \frac{\partial T_C}{\partial x} \right|_{x=L-l} = \begin{cases} -Bi T_C|_{x=L-l} & \text{if } 0 \leq y \leq L_e \\ 0 & \text{if } L_e < y \leq W \end{cases} \quad (3.8)$$

$$\left. \frac{\partial T_C}{\partial y} \right|_{y=0} = 0 \quad \left. \frac{\partial T_C}{\partial y} \right|_{y=W} = 0 \quad (3.9)$$

$$\left. \frac{\partial T_C}{\partial z} \right|_{z=0} = 0 \quad \left. \frac{\partial T_A}{\partial z} \right|_{z=1+H_3} = \begin{cases} \frac{k_{Si}}{k_{GaAs}} & \text{if } 0 \leq y \leq w_2 \\ 0 & \text{if } w_2 < y \leq w_1 \end{cases} \quad (3.10)$$

and the conditions of temperature and flux continuity across the GaAs slab-silicon substrate interface,

$$T_B|_{z=1} = T_A|_{z=1} \quad \text{if } 0 \leq y \leq w_1 \quad (3.11)$$

$$\frac{\partial T_B}{\partial z} \Big|_{z=1} = \begin{cases} \frac{k_{GaAs}}{k_{Si}} \frac{\partial T_A}{\partial z} \Big|_{z=1} & \text{if } 0 \leq y \leq w_1 \\ 0 & \text{if } w_1 < y \leq W \end{cases} \quad (3.12)$$

and across the silicon substrate-fin interface,

$$T_B|_{z=H_1} = T_C|_{z=H_1} \quad \text{if } 0 \leq x \leq L - l \quad (3.13)$$

$$\frac{\partial T_B}{\partial z} \Big|_{z=H_1} = \begin{cases} \frac{\partial T_C}{\partial z} \Big|_{z=H_1} & \text{if } 0 \leq x \leq L - l \\ Bi T_B|_{z=H_1} & \text{if } \begin{cases} L - l < x \leq L \\ 0 \leq y \leq L_e \end{cases} \\ 0 & \text{if } \begin{cases} L - l < x \leq L \\ L_e < y \leq W. \end{cases} \end{cases} \quad (3.14)$$

For the convective boundary conditions corresponding to the silicon substrate and fin it is assumed that the convective heat transfer coefficients are equal,  $h_1 = h_2 = h$ , and vary only in  $y$ -direction. This is a simplifying assumption. In reality  $h$  is not constant at any cross section of the channel, it depends on the channel wall temperature which has a 2-D distribution. The convective boundary conditions are expressed in terms of the Biot number:

$$Bi = \frac{hH_2}{k_{Si}}. \quad (3.15)$$

If the Biot number is constant along the micro-channel cross section,  $\Gamma = \{x : L - l \leq x \leq L\} \cup \{z : 0 \leq z \leq H_1\}$ , and  $T_w$  is the channel wall temperature the heat removed from the source is:

$$\begin{aligned}
\int_0^W \int_{\Gamma} q_w ds dy &= \int_0^W \int_{\Gamma} \frac{\partial T_w}{\partial n} ds dy \\
&= \int_0^W \left( \int_0^{H_1} - \frac{\partial T_C}{\partial x} \Big|_{x=L-l} dz + \int_{L-l}^L \frac{\partial T_B}{\partial z} \Big|_{z=H_1} dx \right) dy \\
&= \int_0^W Bi(y) \left( \int_0^{H_1} T_C(y, z) \Big|_{x=L-l} dz + \int_{L-l}^L T_B(x, y) \Big|_{z=H_1} dx \right) dy.
\end{aligned} \tag{3.16}$$

At any cross section  $y$ , the heat flux is:

$$q_w|_y = \frac{1}{\Gamma} \int_{\Gamma} q_w ds = \frac{Bi(y)}{l + H_1} \left( \int_0^{H_1} T_C(y, z) \Big|_{x=L-l} dz + \int_{L-l}^L T_B(x, y) \Big|_{z=H_1} dx \right). \tag{3.17}$$

Hence the local Biot number is:

$$Bi(y) = \frac{q_w|_y (l + H_1)}{\int_0^{H_1} T_C(y, z) \Big|_{x=L-l} dz + \int_{L-l}^L T_B(x, y) \Big|_{z=H_1} dx}. \tag{3.18}$$

### 3.2.2 1-D Micro heat pipe model

The micro heat pipe, which was first proposed by Cotter [8], has the advantage of large latent energies associated with phase change. Another advantage of the micro heat pipes is a nearly uniform temperature maintained throughout the device due to the phase change. An overview of the state-of-the-art micro heat pipe sinks fabrication and analysis is provided by Tien et al. [66] and Faghri [12]. Numerous analyses have been performed on micro heat pipes, considering the thermodynamics of the liquid-vapor interface [61], [64], [17], [31], the Marangoni effects [64], and the disjoining pressure [29], [64], [57]. Sartre et al. [57] developed

a 3-D steady state model for predicting the heat transfer in a micro heat pipe array. They assumed that the extended meniscus is typically divided into three regions: a macroscopic region with a meniscus of constant mean curvature which is dominated by the capillary forces (intrinsic meniscus region), a transition region or microregion (evaporating thin film region) and a microscopic region which consists of an adsorbed film (non-evaporating region) where the disjoining forces predominate. The results presented for an aluminum/ammonia triangular micro heat pipe array show that the major part of the total heat input goes through the microregion. The mathematical model presented by Khrustalev and Faghri [29], [30] accounted for the effects of interfacial thermal resistance, disjoining pressure, and surface roughness for a given meniscus contact angle. The free surface temperature of the liquid film was determined using the extended Kelvin equation and the expression for interfacial resistance given by the kinetic theory. In this study a 1-D model similar to that proposed by Longtin et al. [41] for triangular cross section micro heat pipes is employed. Longtin's model used a uniform input heat flux while in this analysis the heat flux has a 1-D distribution. The model is developed for the evaporator and adiabatic sections and solved to yield pressure, velocity, and film thickness information in the lengthwise direction of the pipe. Equations for the conservation of mass, momentum, and energy are developed considering only axial variations. During operation the working fluid recedes into the corners of the pipe, generating the necessary capillary driving pressure. Evaporation in the evaporator and condensation in the condenser cause the liquid to accumulate in the condenser section of the device (Figure 3.3).

The amount of liquid- hence the interfacial radius of curvature- varies as a function of axial position  $y$ . The interfacial radius of curvature is related to the pressure difference

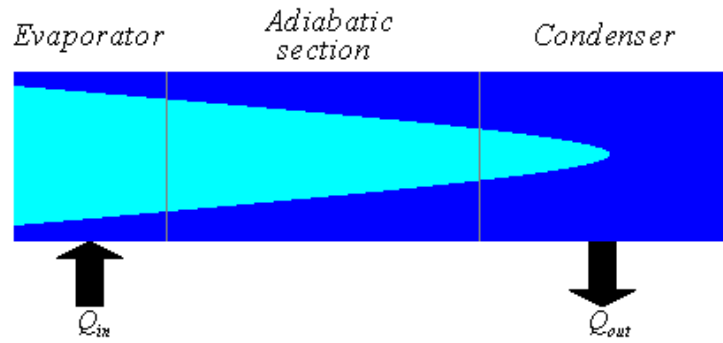


Figure 3.3: Schematic of a MHP.

between the liquid and the vapor phases by the Laplace-Young equation,

$$P_v(y) - P_l(y) = \frac{\sigma}{r(y)} \quad (3.19)$$

or by differentiating with respect to  $y$ ,

$$\frac{dP_v}{dy} - \frac{dP_l}{dy} = -\frac{\sigma}{r^2} \frac{dr}{dy}. \quad (3.20)$$

The derivation of the conservation of mass and momentum equations is performed employing the following assumptions:

- Both liquid and vapor flows are incompressible and the Reynolds number for both flows does not exceed 50;
- Steady state operation;
- Constant fluid properties;



- Negligible viscous dissipation as a consequence of the small velocities in both the liquid and the vapor phases;
- Constant vapor temperature  $T_v$ ;
- The mean radius of curvature is approximately equal to the radius of curvature normal to the pipe axis;
- The interfacial radius of curvature is constant at any given  $y$  location.

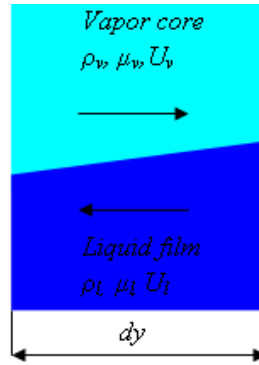


Figure 3.4: Control volume used to derive the conservation equations

The heat pipe is divided into a series of small control volumes of length  $dy$  for which the conservation principles are applied. Some geometrical parameters necessary in the derivation of the governing equations are defined as functions of the contact angle  $\theta$ , pipe corner angle  $\varphi = \pi/2$  and meniscus radius  $r(y)$  (see Figure 3.5).

The liquid cross sectional area (for the 2 corners of our computational domain) is:

$$\begin{aligned}
 A_l &= 2(A_\Delta - A_a) = 2\left(\frac{\eta^2}{2} - A_a\right) \\
 &= 2\left(\frac{\eta^2}{2} - A_{sect} + \frac{r^2 \sin\omega}{2}\right) \\
 &= r^2\left(2\sin^2\frac{\omega}{2} + \sin\omega - \omega\right) = c_l r^2(y). \tag{3.21}
 \end{aligned}$$

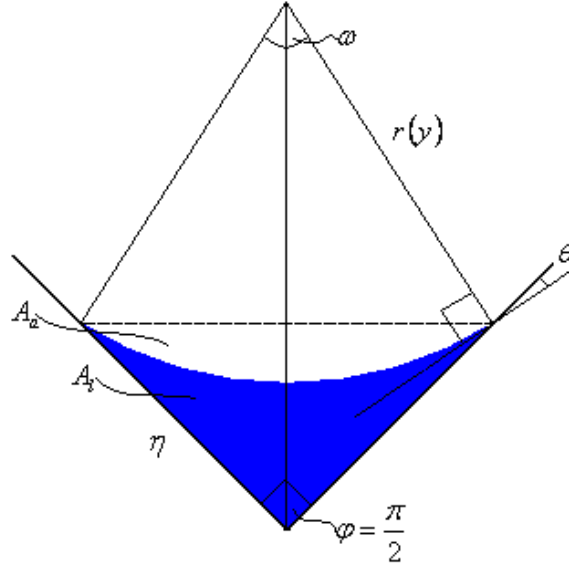


Figure 3.5: A cross section of the MHP with liquid recessed into the corner

The vapor cross sectional area is:

$$A_v = lH_1 - A_l = lH_1 - c_l r^2(y). \quad (3.22)$$

The wall area in contact with the liquid phase and vapor phase, respectively for a control volume of thickness  $dy$  is given by:

$$A_{lw} = 4\eta dy = 4\sqrt{2}\sin\frac{\omega}{2}r dy = c_{lw}r dy \quad (3.23)$$

$$A_{vw} = (2l + H_1 - 4\eta)dy = (2l + H_1 - 4\sqrt{2}\sin\frac{\omega}{2}r)dy = (2l + H_1 - c_{lw}r)dy \quad (3.24)$$

and the area of the liquid-vapor interface for a control volume  $dy$  is given by:

$$A_i = 2r\omega dy = c_i r dy. \quad (3.25)$$

In the above equations  $c_l$ ,  $c_{lw}$ , and  $c_i$  are geometrical constants defined by:

$$c_l = (2\sin^2\frac{\omega}{2} + \sin\omega - \omega), \quad c_{lw} = 4\sqrt{2}\sin\frac{\omega}{2}, \quad c_i = 2\omega. \quad (3.26)$$

It should be mentioned that the radius of curvature must increase monotonically from the evaporator to the condenser to avoid sign changes in the pressure gradient. A continuously increasing radius of curvature results in a continuously increasing liquid cross sectional area. If two liquid films meet in the evaporator or adiabatic section, the device will fail to operate because  $dr/dy$  changes sign. The radius of curvature at this point is called the maximum radius of curvature [41] and is given by:

$$r_{max} = \frac{\min(l, H_1/2)}{\sqrt{2}\sin(\frac{\pi}{4} - \theta)}. \quad (3.27)$$

**Conservation of energy.** The heat entering the computational domain through the  $L \times w_2$  area is removed by the heat pipe through the evaporator section. It is assumed that the heat load is uniformly distributed between the four corners of the pipe and is entirely removed through the evaporator section. The following equation is obtained when applying an energy balance on the computational domain (see Figure 3.2):

$$\begin{aligned} qLw_2 &= \int_0^{L_e} \int_{\Gamma} q_w ds dy \\ &= \int_0^{L_e} h(y) \int_{\Gamma} (T_w - T_f) ds dy \end{aligned} \quad (3.28)$$

where  $q$  is the heat flux applied to the heat sink,  $q_w$  is the heat flux at channel wall,  $T_w$  is the channel wall temperature,  $h$  is the convective heat transfer coefficient, and  $L_e$  is

the evaporator length. Since the micro heat pipe is nearly isothermal during operation, the liquid film is very thin, and the Reynolds numbers are very low we can neglect the conduction, convection and viscous dissipation in the liquid. The heat is transferred only by vaporization at the liquid-vapor interface. The assumption of constant vapor temperature along the pipes implies that only the liquid phase has an expression for the conservation of energy. Applying an energy balance on a control volume of length  $dy$ , we get:

$$\begin{aligned}
q_w|_y dy &= h(y) \left( \int_{L-l}^L (T_B|_{z=H_1} - T_f) dx + \int_0^{H_1} (T_C|_{x=L-l} - T_f) dz \right) dy \\
&= qH_2^2 Bi(y) \left( \int_0^{\bar{H}_1} \bar{T}_C|_{\bar{x}=\bar{L}-\bar{l}} d\bar{z} + \int_{\bar{L}-\bar{l}}^{\bar{L}} \bar{T}_B|_{\bar{z}=\bar{H}_1} d\bar{x} \right) d\bar{y} \\
&= \rho_l V_{il} A_i h_{fg} = \rho_l V_{il} h_{fg} c_i r dy
\end{aligned} \tag{3.29}$$

where  $\rho_l$  is the liquid density,  $V_{il}$  is the liquid interface velocity, and  $h_{fg}$  is the latent heat of vaporization. The overscored quantities are in dimensionless form. From the equation of energy conservation we can obtain the expression for the interfacial liquid velocity (in dimensional form):

$$V_{il} = \frac{qBi(\bar{y}) \left( \int_0^{\bar{H}_1} \bar{T}_C(\bar{y}, \bar{z})|_{\bar{x}=\bar{L}-\bar{l}} d\bar{z} + \int_{\bar{L}-\bar{l}}^{\bar{L}} \bar{T}_B(\bar{x}, \bar{y})|_{\bar{z}=\bar{H}_1} d\bar{x} \right)}{\rho_l h_{fg} c_i \bar{r}} \tag{3.30}$$

**Conservation of mass.** Referring to Figure 3.6 and using the geometrical parameters derived above, Eq.(3.21)-(3.26), after performing a mass balance on a control volume of thickness  $dy$  the following continuity equations are obtained for the liquid and vapor, respectively:

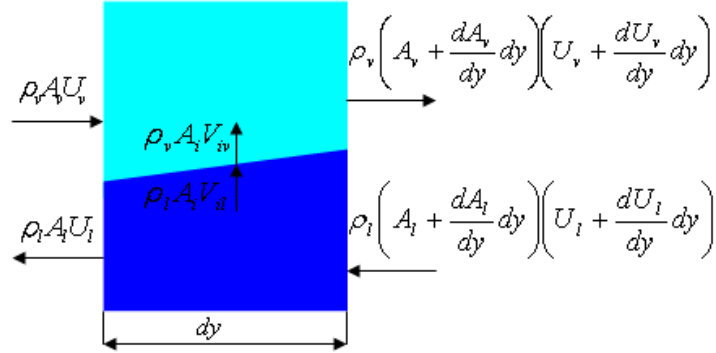


Figure 3.6: Conservation of mass

$$2U_l \frac{dr}{dy} + r \frac{dU_l}{dy} - \frac{c_i}{c_l} V_{il} = 0 \quad (3.31)$$

$$\left( lH_1 - c_l r^2 \right) \frac{dU_v}{dy} - 2c_l r \frac{dr}{dy} U_v - \frac{\rho_l}{\rho_v} c_l r V_{il} = 0 \quad (3.32)$$

The continuity of mass across the interface,  $\rho_l V_{il} = \rho_v V_{iv}$  is used in Eq.(3.32) to relate the vapor interface velocity to that of the liquid.

**Conservation of momentum.** Due to the small velocities in both phases the convective terms in the momentum equations are neglected. The body force (gravity) is significant only for the liquid phase. The surface forces on the control volume are the pressures acting on the cross sectional area and the shear stresses encountered at the liquid-vapor interface and wall (see Figure 3.7). A balance of the body and surface forces on the control volume

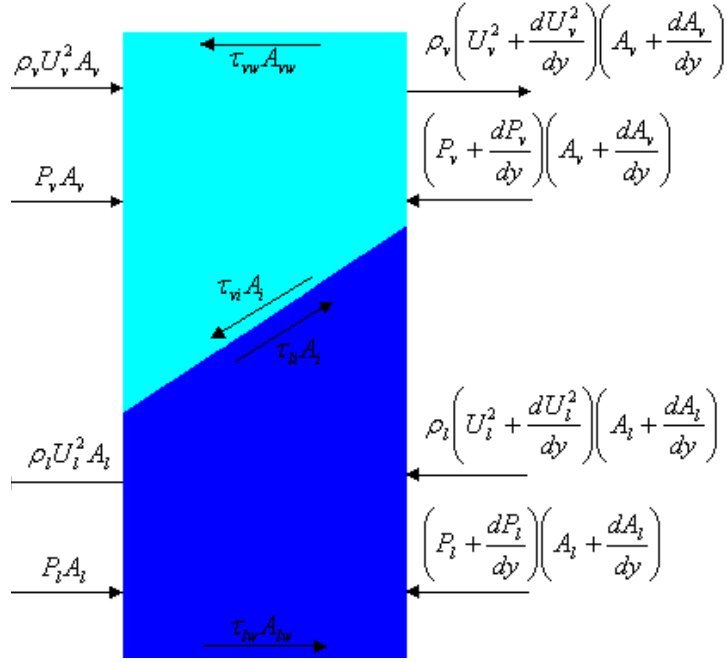


Figure 3.7: Conservation of momentum

yields the following equations for the liquid and vapor respectively:

$$2P_l \frac{dr}{dy} + \frac{dP_l}{dy} r - \frac{c_l}{c_l} \tau_{li} - \frac{c_{lw}}{c_l} \tau_{lw} + \rho_l g r \sin \theta_1 = 0 \quad (3.33)$$

$$-2P_v c_l r \frac{dr}{dy} + (lH_1 - c_l r^2) \frac{dP_v}{dy} + (2l + H_1 - c_l r) \tau_{vw} + c_l r \tau_{vi} = 0. \quad (3.34)$$

In the above equations  $\tau_{lw}$  and  $\tau_{vw}$  are the liquid-wall and vapor-wall shear stresses,  $\tau_{vi}$  is the shear stress at the liquid-vapor interface, and  $\theta_1$  is the pipe inclination angle with respect to gravity. Expressions for the shear stresses are derived by assuming that both flows are fully developed. This assumption is justified since the convective terms are small and the liquid and vapor cross sections vary slowly with  $y$ . The ratio of the vapor velocity to the liquid velocity scales with the inverse ratio of the densities,  $\rho_l/\rho_v$ . For this reason,

from the perspective of the vapor the liquid can be treated as another section of the wall. This assumption was also employed by Thomas et al. [65] in their study of the two phase laminar flow in trapezoidal grooves and by Khurstalev and Faghri [31] who modeled the opposite flows of the vapor and liquid in miniature heat pipes. The interfacial shear stress is computed for the vapor by assuming the liquid to be stationary. Since the liquid and vapor shear stresses at the interface are equal and have opposite directions, the liquid shear follows immediately. The interfacial shear stress due to countercurrent flow in a heat pipe decreases the maximum heat transport. For cases in which the vapor velocity is high this effect is more pronounced. Therefore the amount of liquid charge has a significant impact on the heat pipe performance. The hydraulic diameters for the two phases are computed using the parameters derived earlier in Eq.(3.21)-(3.26):

$$D_{H_l} = \frac{4A_l}{4\eta} = \frac{rc_l}{\sqrt{2}\sin\left(\frac{\pi}{4} - \theta\right)} \quad (3.35)$$

$$D_{H_v} = \frac{4A_v}{2l + H_1 - c_{lw}r + A_i/dy} = \frac{4(lH_1 - c_l r^2)}{2l + H_1 - c_{lw}r + c_l r}. \quad (3.36)$$

The shear stresses are expressed as:

$$\tau_{vi} = \tau_{vw} = \frac{1}{2}\rho_v U_v^2 f_v, \quad f_v = \frac{k_v}{Re_v}, \quad Re_v = \frac{\rho_v U_v D_{H_v}}{\mu_v} \quad (3.37)$$

$$\tau_{li} = -\tau_{vi} \quad (3.38)$$

$$\tau_{lw} = \frac{1}{2}\rho_l U_l^2 f_l, \quad f_l = \frac{k_l}{Re_l}, \quad Re_l = \frac{\rho_l U_l D_{H_l}}{\mu_l} \quad (3.39)$$

The component of the momentum due to the mass entering or leaving the interface during the phase change is neglected [47]. The constants  $k_v$  and  $k_l$  depend upon the geometry of the ducts. For the liquid flow a rectangular geometry is assumed. The following relation was obtained by Wu and Cheng [73] for a trapezoidal cross section:

$$k = 11.43 + 0.8e^{2.67W_b/W_t} \quad (3.40)$$

where  $W_b$  and  $W_t$  are the bottom and top widths of the trapezoidal profile, with  $W_b \leq W_t$ . If in the above equation we make  $W_b = W_t$ , corresponding to a rectangular profile a value of approximately 13 is obtained for  $k_l$ . For the vapor flow the constant  $k_v$  is obtained by averaging between the rectangular cross section displayed in the evaporator section and the almost circular profile attained at the end of the adiabatic section. For the circular cross section  $k = 16$  and hence the value resulting for  $k_v$  is 14.5. Replacing the expressions for  $\tau_{lw}$ ,  $\tau_{li}$ ,  $\tau_{vw}$ , and  $\tau_{vi}$  into the momentum Eq.(3.33)-(3.34) the following equations are obtained:

$$2P_l \frac{dr}{dy} + \frac{dP_l}{dy} r - \frac{c_i k_v U_v \mu_v}{c_l D_{H_v}} - \frac{c_{lw} k_l U_l \mu_l}{c_l D_{H_l}} + \rho_l g r \sin \theta_1 = 0 \quad (3.41)$$

$$-2P_v c_l r \frac{dr}{dy} + (lH_1 - c_l r^2) \frac{dP_v}{dy} + (2l + H_1 - c_{lw} r + c_i r) \frac{k_v U_v \mu_v}{D_{H_v}} = 0 \quad (3.42)$$

The transport Eq.(3.20), (3.31), (3.32), (3.33), (3.34) corresponding to the micro heat pipe are cast into dimensionless form by introducing the following dimensionless variables:

$$\bar{y} \rightarrow \frac{y}{H_2}, \quad \bar{r} \rightarrow \frac{r}{H_2}, \quad \bar{D}_H \rightarrow \frac{D_H}{H_2}$$

$$\bar{U}_l \rightarrow \frac{U_l}{U_{ref}} = \frac{U_l}{Q/(\rho_l D_H^2 h_{fg})}, \quad \bar{U}_v \rightarrow \frac{U_v}{U_{ref}} = \frac{U_v}{Q/(\rho_l D_H^2 h_{fg})},$$



$$\bar{V}_{il} \rightarrow \frac{V_{il}}{U_{ref}} = \frac{Bi(\bar{y}) \left( \int_0^{\bar{H}_1} \bar{T}_C(\bar{y}, \bar{z})|_{\bar{x}=\bar{L}-\bar{l}} d\bar{z} + \int_{\bar{L}-\bar{l}}^{\bar{L}} \bar{T}_B(\bar{x}, \bar{y})|_{\bar{z}=\bar{H}_1} d\bar{x} \right) \frac{D_H^2}{Lw_2}}{c_i \bar{r}} \quad (3.43)$$

$$\bar{P}_l \rightarrow \frac{P_l}{\sigma/D_H} = \frac{P_l}{P_{ref}} \quad \bar{P}_v \rightarrow \frac{P_v}{\sigma/D_H} = \frac{P_v}{P_{ref}}$$

where  $D_H = 2lH_1/(l + H_1)$  is the hydraulic diameter of the empty pipe,  $L_e$  is the evaporator length,  $Q$  is the input power,  $U_{ref} = Q/(\rho_l D_H^2 h_{fg})$  is the reference velocity, and  $P_{ref} = \sigma/D_H$  is the reference pressure. The equations in dimensionless form for the micro heat pipe are (the overbars are omitted):

$$\frac{dP_v}{dy} - \frac{dP_l}{dy} = \frac{2lH_1}{l + H_1} \frac{1}{r^2} \frac{dr}{dy} \quad (3.44)$$

$$2U_l \frac{dr}{dy} + r \frac{dU_l}{dy} - \frac{c_i}{c_l} V_{il} = 0 \quad (3.45)$$

$$(lH_1 - c_l r^2) \frac{dU_v}{dy} - 2c_l r \frac{dr}{dy} U_v - \frac{\rho_l}{\rho_v} c_i r V_{il} = 0 \quad (3.46)$$

$$2P_l \frac{dr}{dy} + \frac{dP_l}{dy} r - Ca \frac{c_i}{c_l} k_v \frac{\mu_v}{\mu_l} \frac{2l + H_1 - c_l w r + c_i r}{4(lH_1 - c_l r^2)} U_v D_H - Ca \frac{c_l w}{c_l^2} k_l \frac{\sqrt{2} \sin \frac{\omega}{2}}{r} U_l D_H + Bo \frac{D_H r \sin \theta}{W^2} = 0 \quad (3.47)$$

$$-2P_v c_l r \frac{dr}{dy} + (lH_1 - c_l r^2) \frac{dP_v}{dy} + Ca \frac{(2l + H_1 - c_l w r + c_i r)^2}{4(lH_1 - c_l r^2)} k_v D_H U_v = 0. \quad (3.48)$$

In the above equations (3.44)-(3.48), the geometrical parameters of the channel  $l$ ,  $H_1$ ,  $W$ ,  $D_H$  are in dimensionless form. The dimensionless groups introduced,

$$Ca = \frac{\mu_l U_{ref}}{\sigma}, \quad Bo = \frac{\rho_l g W^2}{\sigma}$$

represent the capillary number and Bond number, respectively. The capillary number  $Ca$  is the ratio of the viscous force to surface tension force and the Bond number  $Bo$  measures the contribution of the gravitational and capillary forces. Since the transport equations for the heat pipe are first order ordinary differential equations, boundary conditions are needed at only one point. The solution of these equations has two parts, one corresponding to the evaporator section and one to the adiabatic section. The boundary conditions for the adiabatic section are taken from the solution of the evaporator section at the evaporator-adiabatic interface. The boundary conditions used at the end of the evaporator ( $y = 0$ ) in nondimensional form are:

$$r|_{y=0} = r_0, \quad U_l|_{y=0} = 0, \quad U_v|_{y=0} = 0, \quad (3.49)$$

$$P_v|_{y=0} = P_v(T_v), \quad P_l|_{y=0} = P_v|_{y=0} - \frac{D_H}{r_0}.$$

The boundary vapor pressure  $P_v|_{y=0}$  is taken to be the saturation pressure of the vapor at temperature  $T_v$ . The liquid boundary pressure is related to the vapor boundary pressure by the Laplace-Young equation. The value for the meniscus radius at  $y = 0$ ,  $r_0$  is given as an initial guess [41].

The direct problem associated with the mathematical formulation given by Eq.(3.1)-(3.14), involves the determination of temperature fields in the GaAs substrate, silicon substrate, and fin from the knowledge of domain geometry and the physical properties of GaAs and silicon.

### 3.3 The optimal control problem with $Bi$ and geometrical parameters as controls

An optimum  $Bi$  distribution for a finned heat sink was found previously by Simionescu and Harris [59]. The analysis presented here uses two controls, i.e. the Biot number and the aspect ratio, being an extension of the previous work. In the optimal control problem  $Bi$  and  $p = l/H_1$  are the unknowns, where  $p$  is the channel aspect ratio, and Eq.(3.1)-(3.14) are constraints that have to be satisfied. The problem is to find the optimum channel geometry and the optimum Biot number that maximize the amount of heat removed from the heat source (or minimize the thermal resistance). The difference between this problem and the classic fin shape optimization problem studied previously [74], [22], [52] consists in the consideration of the heat removed from the interfin area. This amount of heat was neglected in previous works, but it is taken into account in this study since we made the assumption of uniform heat load distribution between the four corners of the pipe. The following functional is considered for minimization in our optimal control problem:

$$J = \int_0^W \int_0^L \int_1^{1+H_3} T_A^2 dx dy dz + \frac{\alpha}{2} \int_0^{L_e} Bi^2 dy. \quad (3.50)$$

Here  $T_A$  is the computed temperature within the GaAs slab, subject to the constraints dictated by the direct problem (3.1)-(3.14), and  $\alpha$  is a weighting coefficient penalizing  $Bi$ . The goal of optimization is to minimize the first term appearing in the definition of the functional  $J$ . The second term is added to account for the *cost* of the control parameter  $Bi$ . The nonnegative penalty parameter  $\alpha$  can be used to change the relative importance of the last term in Eq.(3.50).

### 3.3.1 Conjugate gradient algorithm

Minimizing sequences are constructed using the conjugate gradient method and the following iterative scheme (see [6]):

$$p^{(n+1)} = p^{(n)} - \beta_1^{(n)} P_1^{(n)} \quad (3.51)$$

$$Bi^{(n+1)} = Bi^{(n)} - \beta_2^{(n)} P_2^{(n)} \quad (3.52)$$

where  $\beta_1^{(n)}$  and  $\beta_2^{(n)}$  are the step sizes and  $P_1^{(n)}$  and  $P_2^{(n)}$  are the search directions which are determined from:

$$P_1^{(n)} = \left( \frac{\partial J}{\partial p} \right)^{(n)} + \gamma_1^{(n)} P_1^{(n-1)} \quad (3.53)$$

$$P_2^{(n)} = \left( \frac{\partial J}{\partial Bi} \right)^{(n)} + \gamma_2^{(n)} P_2^{(n-1)}. \quad (3.54)$$

The conjugate coefficients  $\gamma_1^{(n)}$  and  $\gamma_2^{(n)}$  are given by:

$$\gamma_1^{(n)} = \frac{\left[ \left( \frac{\partial J}{\partial p} \right)^{(n)} \right]^2}{\left[ \left( \frac{\partial J}{\partial p} \right)^{(n-1)} \right]^2} \quad \text{with} \quad \gamma_1^{(0)} = 0 \quad (3.55)$$

$$\gamma_2^{(n)} = \frac{\int_0^{L_e} \left[ \left( \frac{\partial J}{\partial Bi} \right)^{(n)} \right]^2 dy}{\int_0^{L_e} \left[ \left( \frac{\partial J}{\partial Bi} \right)^{(n-1)} \right]^2 dy} \quad \text{with} \quad \gamma_2^{(0)} = 0. \quad (3.56)$$

The iterative process described by Eq.(3.51)–(3.56) requires the step sizes  $\beta_1^{(n)}$  and  $\beta_2^{(n)}$  and the gradient of the functional,  $\nabla J^{(n)} = \left[ \left( \frac{\partial J}{\partial p} \right)^{(n)}, \left( \frac{\partial J}{\partial Bi} \right)^{(n)} \right]$ . These parameters will be computed from the sensitivity and adjoint problems, respectively.

### 3.3.2 Sensitivity problem and calculation of the search step sizes

The problem of finding the boundary configuration of the computational domain is a shape identification problem. Shape identification problems were previously studied by Huang and Shih [23], Huang and Chen [21], Huang and Chao [20], and Park and Shin [46]. In these works either one or multiple surface configurations were recovered using the conjugate gradient method. In this analysis the solution of the heat transfer is controlled by the convective boundary condition, taking the Biot number and the aspect ratio as controls. We need to solve two sensitivity problems corresponding to each control parameter. The sensitivity problems are obtained from the direct problem, Eq.(3.1)-(3.14), by perturbing the aspect ratio and Biot number, one at a time. When  $p$  is perturbed by  $\Delta p$ , the temperatures  $T_A$ ,  $T_B$ , and  $T_C$  are perturbed by  $\Delta T_A^1$ ,  $\Delta T_B^1$ , and  $\Delta T_C^1$ , respectively. If  $Bi$  undergoes a perturbation  $Bi + \Delta Bi$ , the temperatures  $T_A$ ,  $T_B$ , and  $T_C$  are perturbed by  $\Delta T_A^2$ ,  $\Delta T_B^2$ , and  $\Delta T_C^2$ , respectively. Then replacing in the direct problem  $p$  by  $p + \Delta p$ ,  $T_A$  by  $T_A + \Delta T_A^1$ ,  $T_B$  by  $T_B + \Delta T_B^1$ , and  $T_C$  by  $T_C + \Delta T_C^1$  and subtracting from the resulting equations the direct problem, the following sensitivity problem for the sensitivity functions  $\Delta T_A^1$ ,  $\Delta T_B^1$ , and  $\Delta T_C^1$  is obtained, if the second order terms are neglected:

$$\frac{\partial^2 \Delta T_A^1}{\partial x^2} + \frac{\partial^2 \Delta T_A^1}{\partial y^2} + \frac{\partial^2 \Delta T_A^1}{\partial z^2} = 0 \quad (3.57)$$

$$\frac{\partial^2 \Delta T_B^1}{\partial x^2} + \frac{\partial^2 \Delta T_B^1}{\partial y^2} + \frac{\partial^2 \Delta T_B^1}{\partial z^2} = 0 \quad (3.58)$$

$$\frac{\partial^2 \Delta T_C^1}{\partial x^2} + \frac{\partial^2 \Delta T_C^1}{\partial y^2} + \frac{\partial^2 \Delta T_C^1}{\partial z^2} = 0 \quad (3.59)$$

subject to the following boundary conditions,

$$\left. \frac{\partial \Delta T_A^1}{\partial x} \right|_{x=0} = 0 \qquad \left. \frac{\partial \Delta T_A^1}{\partial x} \right|_{x=L} = 0 \qquad (3.60)$$

$$\left. \frac{\partial \Delta T_A^1}{\partial y} \right|_{y=0} = 0 \qquad \left. \frac{\partial \Delta T_A^1}{\partial y} \right|_{y=w_1} = 0 \qquad (3.61)$$

$$\left. \frac{\partial \Delta T_B^1}{\partial x} \right|_{x=0} = 0 \qquad \left. \frac{\partial \Delta T_B^1}{\partial x} \right|_{x=W} = 0 \qquad (3.62)$$

$$\left. \frac{\partial \Delta T_B^1}{\partial y} \right|_{y=0} = 0 \qquad \left. \frac{\partial \Delta T_B^1}{\partial y} \right|_{y=W} = 0 \qquad (3.63)$$

$$\begin{aligned} \left. \frac{\partial \Delta T_C^1}{\partial x} \right|_{x=0} &= 0 \\ \Delta T_C^1 &= T_C(l + \Delta l) - T_C(l) \approx \left. \frac{\partial T_C}{\partial x} \right|_{x=L-l} H_1 \Delta p = -Bi T_C|_{x=L-l} H_1 \Delta p \\ \left. \frac{\partial \Delta T_C^1}{\partial x} \right|_{x=L-l} &= \begin{cases} -Bi \left. \frac{\partial T_C}{\partial x} \right|_{x=L-l} H_1 \Delta p & \text{if } 0 \leq y \leq L_e \\ 0 & \text{if } L_e < y \leq W \end{cases} \end{aligned} \qquad (3.64)$$

$$\left. \frac{\partial \Delta T_C^1}{\partial y} \right|_{y=0} = 0 \qquad \left. \frac{\partial \Delta T_C^1}{\partial y} \right|_{y=W} = 0 \qquad (3.65)$$

$$\left. \frac{\partial \Delta T_C^1}{\partial z} \right|_{z=0} = 0 \qquad \left. \frac{\partial \Delta T_A^1}{\partial z} \right|_{z=1+H_3} = 0 \qquad (3.66)$$

and the conditions of temperature and flux continuity across the GaAs slab-silicon substrate interface,

$$\Delta T_B^1 \Big|_{z=1} = \Delta T_A^1 \Big|_{z=1} \qquad \text{if } 0 \leq y \leq w_1 \qquad (3.67)$$

$$\left. \frac{\partial \Delta T_B^1}{\partial z} \right|_{z=1} = \begin{cases} \frac{k_{GaAs}}{k_{Si}} \left. \frac{\partial \Delta T_A^1}{\partial z} \right|_{z=1} & \text{if } 0 \leq y \leq w_1 \\ 0 & \text{if } w_1 < y \leq W \end{cases} \quad (3.68)$$

and across the silicon substrate-fin interface,

$$\Delta T_B^1 \Big|_{z=H_1} = \Delta T_C^1 \Big|_{z=H_1} \quad \text{if } 0 \leq x \leq L-l \quad (3.69)$$

$$\left. \frac{\partial \Delta T_B^1}{\partial z} \right|_{z=H_1} = \begin{cases} \left. \frac{\partial \Delta T_C^1}{\partial z} \right|_{z=H_1} & \text{if } 0 \leq x \leq L-l \\ Bi \Delta T_B^1 \Big|_{z=H_1} & \text{if } \begin{cases} L-l < x \leq L \\ 0 < y \leq L_e \end{cases} \\ 0 & \text{if } \begin{cases} L-l < x \leq L \\ L_e < y \leq L. \end{cases} \end{cases} \quad (3.70)$$

The solution of the sensitivity problem corresponding to a variation of the Biot number  $\Delta Bi$  is obtained by solving the following equations:

$$\frac{\partial^2 \Delta T_A^2}{\partial x^2} + \frac{\partial^2 \Delta T_A^2}{\partial y^2} + \frac{\partial^2 \Delta T_A^2}{\partial z^2} = 0 \quad (3.71)$$

$$\frac{\partial^2 \Delta T_B^2}{\partial x^2} + \frac{\partial^2 \Delta T_B^2}{\partial y^2} + \frac{\partial^2 \Delta T_B^2}{\partial z^2} = 0 \quad (3.72)$$

$$\frac{\partial^2 \Delta T_C^2}{\partial x^2} + \frac{\partial^2 \Delta T_C^2}{\partial y^2} + \frac{\partial^2 \Delta T_C^2}{\partial z^2} = 0 \quad (3.73)$$

with the corresponding boundary conditions,

$$\left. \frac{\partial \Delta T_A^2}{\partial x} \right|_{x=0} = 0 \quad \left. \frac{\partial \Delta T_A^2}{\partial x} \right|_{x=L} = 0 \quad (3.74)$$

$$\left. \frac{\partial \Delta T_A^2}{\partial y} \right|_{y=0} = 0 \qquad \left. \frac{\partial \Delta T_A^2}{\partial y} \right|_{y=w_1} = 0 \qquad (3.75)$$

$$\left. \frac{\partial \Delta T_B^2}{\partial x} \right|_{x=0} = 0 \qquad \left. \frac{\partial \Delta T_B^2}{\partial x} \right|_{x=W} = 0 \qquad (3.76)$$

$$\left. \frac{\partial \Delta T_B^2}{\partial y} \right|_{y=0} = 0 \qquad \left. \frac{\partial \Delta T_B^2}{\partial y} \right|_{y=W} = 0 \qquad (3.77)$$

$$\left. \frac{\partial \Delta T_C^2}{\partial x} \right|_{x=0} = 0 \qquad \left. \frac{\partial \Delta T_C^2}{\partial x} \right|_{x=L-l} = \begin{cases} Bi \Delta T_C^2|_{x=L-l} + \Delta Bi T_C|_{x=L-l} & \text{if } 0 \leq y \leq L_e \\ 0 & \text{if } L_e < y \leq W \end{cases} \qquad (3.78)$$

$$\left. \frac{\partial \Delta T_C^2}{\partial y} \right|_{y=0} = 0 \qquad \left. \frac{\partial \Delta T_C^2}{\partial y} \right|_{y=W} = 0 \qquad (3.79)$$

$$\left. \frac{\partial \Delta T_C^2}{\partial z} \right|_{z=0} = 0 \qquad \left. \frac{\partial \Delta T_A^2}{\partial z} \right|_{z=1+H_3} = 0 \qquad (3.80)$$

and the conditions of temperature and flux continuity across the GaAs slab-silicon substrate interface,

$$\Delta T_B^2|_{z=1} = \Delta T_A^2|_{z=1} \qquad \text{if } 0 \leq y \leq w_1 \qquad (3.81)$$

$$\left. \frac{\partial \Delta T_B^2}{\partial z} \right|_{z=1} = \begin{cases} \frac{k_{GaAs}}{k_{Si}} \left. \frac{\partial \Delta T_A^2}{\partial z} \right|_{z=1} & \text{if } 0 \leq y \leq w_1 \\ 0 & \text{if } w_1 < y \leq W \end{cases} \qquad (3.82)$$

and across the silicon substrate-fin interface,

$$\Delta T_B^2|_{z=H_1} = \Delta T_C^2|_{z=H_1} \qquad \text{if } 0 \leq x \leq L-l \qquad (3.83)$$



$$\frac{\partial \Delta T_B^2}{\partial z} \Big|_{z=H_1} = \begin{cases} \frac{\partial \Delta T_C^2}{\partial z} \Big|_{z=H_1} & \text{if } 0 \leq x \leq L-l \\ Bi \Delta T_B^2 \Big|_{z=H_1} + \Delta Bi T_B \Big|_{z=H_1} & \text{if } \begin{cases} L-l < x \leq L \\ 0 < y \leq L_e \end{cases} \\ 0 & \text{if } \begin{cases} L-l < x \leq L \\ L_e < y \leq L. \end{cases} \end{cases} \quad (3.84)$$

The functional  $J^{(n+1)}$  for the  $(n+1)$ th iteration is written by replacing  $p^{(n+1)}$  and  $Bi^{(n+1)}$  with the expressions given by Eq.(3.51)-(3.52):

$$J^{(n+1)} = \int_1^{1+H_3} \int_0^{w_1} \int_0^L \left[ T_A(x, y, z, p^{(n)} - \beta_1^{(n)} P_1^{(n)}, Bi^{(n)} - \beta_2^{(n)} P_2^{(n)}) \right]^2 dx dy dz + \frac{\alpha}{2} \int_0^{L_e} (Bi^{(n)} - \beta_2^{(n)} P_2^{(n)})^2 dy. \quad (3.85)$$

By expanding in Taylor series  $T_A$ ,  $p$ , and  $Bi$  the following expression is obtained for the functional  $J$  at the  $(n+1)$ th iteration:

$$J^{(n+1)} = \int_1^{1+H_3} \int_0^{w_1} \int_0^L \left[ T_A(x, y, z, p^{(n)}, Bi^{(n)}) - \beta_1^{(n)} \Delta T_A^1(P_1^{(n)}) - \beta_2^{(n)} \Delta T_A^2(P_2^{(n)}) \right]^2 dx dy dz + \frac{\alpha}{2} \int_0^{L_e} (Bi^{(n)} - \beta_2^{(n)} P_2^{(n)})^2 dy. \quad (3.86)$$

The search step sizes  $\beta_1$  and  $\beta_2$  are found from the line search in each direction at each iteration by taking partial derivatives of Eq.(3.86) with respect to  $\beta_1$  and  $\beta_2$  and equating the obtained expressions to zero. The following system of equations is obtained:

$$\beta_1^{(n)} = \frac{\int_1^{1+H_3} \int_0^{w_1} \int_0^L 2 \Delta T_A^1 (T_A - \beta_2 \Delta T_A^2) dx dy dz}{\int_1^{1+H_3} \int_0^{w_1} \int_0^L 2 (\Delta T_A^1)^2 dx dy dz} \quad (3.87)$$

$$\beta_2^{(n)} = \frac{\int_1^{1+H_3} \int_0^{w_1} \int_0^L 2\Delta T_A^2 (T_A - \beta_1 \Delta T_A^1) dx dy dz + \frac{\alpha}{2} \int_0^{L_e} B i^{(n)} P_2^{(n)} dy}{\int_1^{1+H_3} \int_0^{w_1} \int_0^L 2(\Delta T_A^2)^2 dx dy dz + \frac{\alpha}{2} \int_0^{L_e} (P_2^{(n)})^2 dy}. \quad (3.88)$$

### 3.3.3 Adjoint problems

The Lagrangian associated with the optimization problem defined by Eq.(3.50), the constraints (3.1)-(3.14), and the control parameter  $p$  is:

$$\begin{aligned} J|_p &= \int_1^{1+H_3} \int_0^W \int_0^L T_A^2 dx dy dz + \frac{\alpha}{2} \int_0^{L_e} B i^2 dy \\ &+ \int_1^{1+H_3} \int_0^W \int_0^L \lambda_1 \left( \frac{\partial^2 T_A}{\partial x^2} + \frac{\partial^2 T_A}{\partial y^2} + \frac{\partial^2 T_A}{\partial z^2} \right) dx dy dz \\ &+ \int_{H_1}^1 \int_0^W \int_0^L \lambda_2 \left( \frac{\partial^2 T_B}{\partial x^2} + \frac{\partial^2 T_B}{\partial y^2} + \frac{\partial^2 T_B}{\partial z^2} \right) dx dy dz \\ &+ \int_0^{H_1} \int_0^W \int_0^{L-pH_1} \lambda_3 \left( \frac{\partial^2 T_C}{\partial x^2} + \frac{\partial^2 T_C}{\partial y^2} + \frac{\partial^2 T_C}{\partial z^2} \right) dx dy dz \end{aligned} \quad (3.89)$$

where  $\lambda_1$ ,  $\lambda_2$ , and  $\lambda_3$  are Lagrange multipliers. The differential of Lagrangian corresponding to  $\Delta p$  is:

$$\begin{aligned} J|_{p+\Delta p} - J|_p &= \int_1^{1+H_3} \int_0^W \int_0^L 2T_A \Delta T_A^1 dx dy dz \\ &+ \int_1^{1+H_3} \int_0^W \int_0^L \lambda_1 \left( \frac{\partial^2 \Delta T_A^1}{\partial x^2} + \frac{\partial^2 \Delta T_A^1}{\partial y^2} + \frac{\partial^2 \Delta T_A^1}{\partial z^2} \right) dx dy dz \\ &+ \int_{H_1}^1 \int_0^W \int_0^L \lambda_2 \left( \frac{\partial^2 \Delta T_B^1}{\partial x^2} + \frac{\partial^2 \Delta T_B^1}{\partial y^2} + \frac{\partial^2 \Delta T_B^1}{\partial z^2} \right) dx dy dz \\ &+ \int_0^{H_1} \int_0^W \int_0^{L-H_1 p} \lambda_3 \left( \frac{\partial^2 \Delta T_C^1}{\partial x^2} + \frac{\partial^2 \Delta T_C^1}{\partial y^2} + \frac{\partial^2 \Delta T_C^1}{\partial z^2} \right) dx dy dz. \end{aligned} \quad (3.90)$$

Integration of the above expression leads to the following adjoint problem after boundary conditions from the sensitivity problem (3.57)-(3.70) are applied:

$$\frac{\partial^2 \lambda_1}{\partial x^2} + \frac{\partial^2 \lambda_1}{\partial y^2} + \frac{\partial^2 \lambda_1}{\partial z^2} + 2T_A = 0 \quad (3.91)$$

$$\frac{\partial^2 \lambda_2}{\partial x^2} + \frac{\partial^2 \lambda_2}{\partial y^2} + \frac{\partial^2 \lambda_2}{\partial z^2} = 0 \quad (3.92)$$

$$\frac{\partial^2 \lambda_3}{\partial x^2} + \frac{\partial^2 \lambda_3}{\partial y^2} + \frac{\partial^2 \lambda_3}{\partial z^2} = 0 \quad (3.93)$$

subject to the following boundary conditions,

$$\left. \frac{\partial \lambda_1}{\partial x} \right|_{x=0} = 0 \quad \left. \frac{\partial \lambda_1}{\partial x} \right|_{x=L} = 0 \quad (3.94)$$

$$\left. \frac{\partial \lambda_1}{\partial y} \right|_{y=0} = 0 \quad \left. \frac{\partial \lambda_1}{\partial y} \right|_{y=w_1} = 0 \quad (3.95)$$

$$\left. \frac{\partial \lambda_2}{\partial x} \right|_{x=0} = 0 \quad \left. \frac{\partial \lambda_2}{\partial x} \right|_{x=L-l} = 0 \quad (3.96)$$

$$\left. \frac{\partial \lambda_2}{\partial y} \right|_{y=0} = 0 \quad \left. \frac{\partial \lambda_2}{\partial y} \right|_{y=W} = 0 \quad (3.97)$$

$$\left. \frac{\partial \lambda_3}{\partial x} \right|_{x=0} = 0 \quad \left. \frac{\partial \lambda_3}{\partial x} \right|_{x=L-l} = 0 \quad (3.98)$$

$$\left. \frac{\partial \lambda_3}{\partial y} \right|_{y=0} = 0 \quad \left. \frac{\partial \lambda_3}{\partial y} \right|_{y=W} = 0 \quad (3.99)$$

$$\left. \frac{\partial \lambda_3}{\partial z} \right|_{z=0} = 0 \quad \left. \frac{\partial \lambda_1}{\partial z} \right|_{z=1+H_3} = 0 \quad (3.100)$$

and the conditions of temperature and flux continuity across the GaAs slab-silicon substrate interface,

$$\lambda_2|_{z=1} = \frac{k_{GaAs}}{k_{Si}} \lambda_1|_{z=1} \quad \text{if } 0 \leq y \leq w_1 \quad (3.101)$$

$$\frac{\partial \lambda_2}{\partial z} \Big|_{z=1} = \begin{cases} \frac{\partial \lambda_1}{\partial z} \Big|_{z=1} & \text{if } 0 \leq y \leq w_1 \\ 0 & \text{if } w_1 < y \leq W \end{cases} \quad (3.102)$$

and across the silicon substrate-fin interface,

$$\lambda_2|_{z=H_1} = \lambda_3|_{z=H_1} \quad \text{if } 0 \leq x \leq L-l \quad (3.103)$$

$$\frac{\partial \lambda_2}{\partial z} \Big|_{z=H_1} = \begin{cases} \frac{\partial \lambda_2}{\partial z} \Big|_{z=H_1} & \text{if } 0 \leq x \leq L-l \\ Bi\lambda_2|_{z=H_1} & \text{if } \begin{cases} L-l < x \leq L \\ 0 \leq y \leq L_e \end{cases} \\ 0 & \text{if } \begin{cases} L-l < x \leq L \\ L_e < y \leq W. \end{cases} \end{cases} \quad (3.104)$$

After identifying the adjoint problem, the following integral term is left:

$$\begin{aligned} \Delta J|_p &= J|_{p+\Delta p} - J|_p \\ &= \int_0^{H_1} \int_0^{L_e} Bi \frac{\partial T_C}{\partial x} \lambda_3 \Big|_{x=L-pH_1} \Delta p dy dz \\ &= \int_0^{H_1} \int_0^{L_e} \frac{\partial J}{\partial p} \Delta p dy dz \end{aligned} \quad (3.105)$$

and the following expression for  $\frac{\partial J}{\partial p}$  is obtained,

$$\frac{\partial J}{\partial p} = Bi \frac{\partial T_C}{\partial x} \lambda_3 \Big|_{x=L-pH_1}. \quad (3.106)$$

The adjoint problem corresponding to  $Bi$  is obtained in a similar way. The associated Lagrangian in this case is:

$$\begin{aligned} J|_{Bi} &= \int_1^{1+H_3} \int_0^W \int_0^L T_A^2 dx dy dz + \frac{\alpha}{2} \int_0^{L_e} Bi^2 dy \\ &+ \int_1^{1+H_3} \int_0^W \int_0^L \xi_1 \left( \frac{\partial^2 T_A}{\partial x^2} + \frac{\partial^2 T_A}{\partial y^2} + \frac{\partial^2 T_A}{\partial z^2} \right) dx dy dz \\ &+ \int_{H_1}^1 \int_0^W \int_0^L \xi_2 \left( \frac{\partial^2 T_B}{\partial x^2} + \frac{\partial^2 T_B}{\partial y^2} + \frac{\partial^2 T_B}{\partial z^2} \right) dx dy dz \\ &+ \int_0^{H_1} \int_0^W \int_0^{L-pH_1} \xi_3 \left( \frac{\partial^2 T_C}{\partial x^2} + \frac{\partial^2 T_C}{\partial y^2} + \frac{\partial^2 T_C}{\partial z^2} \right) dx dy dz \end{aligned} \quad (3.107)$$

and the differential of Lagrangian corresponding to  $\Delta Bi$  is:

$$\begin{aligned} J|_{Bi+\Delta Bi} - J|_{Bi} &= \int_1^{1+H_3} \int_0^W \int_0^L 2T_A \Delta T_A^2 dx dy dz + \alpha \int_0^{L_e} Bi \Delta Bi dy \\ &+ \int_1^{1+H_3} \int_0^W \int_0^L \xi_1 \left( \frac{\partial^2 \Delta T_A^2}{\partial x^2} + \frac{\partial^2 \Delta T_A^2}{\partial y^2} + \frac{\partial^2 \Delta T_A^2}{\partial z^2} \right) dx dy dz \\ &+ \int_{H_1}^1 \int_0^W \int_0^L \xi_2 \left( \frac{\partial^2 \Delta T_B^2}{\partial x^2} + \frac{\partial^2 \Delta T_B^2}{\partial y^2} + \frac{\partial^2 \Delta T_B^2}{\partial z^2} \right) dx dy dz \\ &+ \int_0^{H_1} \int_0^W \int_0^{L-pH_1} \xi_3 \left( \frac{\partial^2 \Delta T_C^2}{\partial x^2} + \frac{\partial^2 \Delta T_C^2}{\partial y^2} + \frac{\partial^2 \Delta T_C^2}{\partial z^2} \right) dx dy dz. \end{aligned} \quad (3.108)$$

The following adjoint problem is obtained after performing the integration by parts in Eq.(3.108):

$$\frac{\partial^2 \xi_1}{\partial x^2} + \frac{\partial^2 \xi_1}{\partial y^2} + \frac{\partial^2 \xi_1}{\partial z^2} + 2T_A = 0 \quad (3.109)$$

$$\frac{\partial^2 \xi_2}{\partial x^2} + \frac{\partial^2 \xi_2}{\partial y^2} + \frac{\partial^2 \xi_2}{\partial z^2} = 0 \quad (3.110)$$

$$\frac{\partial^2 \xi_3}{\partial x^2} + \frac{\partial^2 \xi_3}{\partial y^2} + \frac{\partial^2 \xi_3}{\partial z^2} = 0 \quad (3.111)$$

subject to the following boundary conditions,

$$\left. \frac{\partial \xi_1}{\partial x} \right|_{x=0} = 0 \quad \left. \frac{\partial \xi_1}{\partial x} \right|_{x=L} = 0 \quad (3.112)$$

$$\left. \frac{\partial \xi_1}{\partial y} \right|_{y=0} = 0 \quad \left. \frac{\partial \xi_1}{\partial y} \right|_{y=w_1} = 0 \quad (3.113)$$

$$\left. \frac{\partial \xi_2}{\partial x} \right|_{x=0} = 0 \quad \left. \frac{\partial \xi_2}{\partial x} \right|_{x=L} = 0 \quad (3.114)$$

$$\left. \frac{\partial \xi_2}{\partial y} \right|_{y=0} = 0 \quad \left. \frac{\partial \xi_2}{\partial y} \right|_{y=W} = 0 \quad (3.115)$$

$$\left. \frac{\partial \xi_3}{\partial x} \right|_{x=0} = 0 \quad \left. \frac{\partial \xi_3}{\partial x} \right|_{x=L-l} = \begin{cases} -Bi \xi_3|_{x=L-l} & \text{if } 0 \leq y \leq L_e \\ 0 & \text{if } L_e < y \leq W \end{cases} \quad (3.116)$$

$$\left. \frac{\partial \xi_3}{\partial y} \right|_{y=0} = 0 \quad \left. \frac{\partial \xi_3}{\partial y} \right|_{y=W} = 0 \quad (3.117)$$

$$\left. \frac{\partial \xi_3}{\partial z} \right|_{z=0} = 0 \quad \left. \frac{\partial \xi_1}{\partial z} \right|_{z=1+H_3} = 0 \quad (3.118)$$

and the conditions of temperature and flux continuity across the GaAs slab-silicon substrate interface,

$$\xi_1|_{z=1} = \frac{k_{GaAs}}{k_{Si}} \xi_2|_{z=1} \quad \text{if } 0 \leq y \leq w_1 \quad (3.119)$$

$$\frac{\partial \xi_2}{\partial z} \Big|_{z=1} = \begin{cases} \frac{\partial \xi_1}{\partial z} \Big|_{z=1} & \text{if } 0 \leq y \leq w_1 \\ 0 & \text{if } w_1 < y \leq W \end{cases} \quad (3.120)$$

and across the silicon substrate-fin interface,

$$\xi_2|_{z=H_1} = \xi_3|_{z=H_1} \quad \text{if } 0 \leq x \leq L-l \quad (3.121)$$

$$\frac{\partial \xi_2}{\partial z} \Big|_{z=H_1} = \begin{cases} \frac{\partial \xi_3}{\partial z} \Big|_{z=H_1} & \text{if } 0 \leq x \leq L-l \\ Bi \xi_2|_{z=H_1} & \text{if } \begin{cases} L-l < x \leq L \\ 0 < y \leq L_e \end{cases} \\ 0 & \text{if } \begin{cases} L-l < x \leq L \\ L_e < y \leq L. \end{cases} \end{cases} \quad (3.122)$$

After identifying the adjoint problem, the following integral term is left:

$$\begin{aligned} \Delta J|_{Bi} &= J|_{Bi+\Delta Bi} - J|_{Bi} \\ &= \int_0^{L_e} \left( \alpha Bi - \int_0^{H_1} \xi_3 T_C|_{x=L-pH_1} dz - \int_{L-pH_1}^L \xi_2 T_B|_{z=H_1} dx \right) \Delta Bi dy \end{aligned} \quad (3.123)$$

and the following expression for  $\frac{\partial J}{\partial Bi}$  is obtained,

$$\frac{\partial J}{\partial Bi} = \alpha Bi - \int_0^{H_1} \xi_3 T_C|_{x=L-pH_1} dz - \int_{L-pH_1}^L \xi_2 T_B|_{z=H_1} dx. \quad (3.124)$$

### 3.3.4 Computational algorithm

The computational procedure for the solution of this problem may be summarized as follows:

- step 1* Solve the direct problem given by Eq.(3.1)-(3.14) to obtain  $T_A$ ,  $T_B$  and  $T_C$  for an initial guess of the controls  $p$  and  $Bi$ ;
- step 2* Solve the adjoint problems given by Eq.(3.91)-(3.104) and Eq.(3.109)-(3.122), respectively to obtain  $\lambda_1$ ,  $\lambda_2$ ,  $\lambda_3$ ,  $\xi_1$ ,  $\xi_2$ , and  $\xi_3$ ;
- step 3* Compute the gradients of the functional  $\frac{\partial J}{\partial p}$  and  $\frac{\partial J}{\partial Bi}$  from Eq.(3.106) and Eq.(3.124), respectively;
- step 4* Compute the conjugate coefficients  $\gamma_1^{(n)}$  and  $\gamma_2^{(n)}$  from Eq.(3.55) and Eq.(3.56), and the search directions  $P_1^{(n)}$  and  $P_2^{(n)}$  from Eq.(3.53) and Eq.(3.54);
- step 5* Set  $\Delta p = P_1^{(n)}$ ,  $\Delta Bi = P_2^{(n)}$  and solve the sensitivity problems given by Eq.(3.57)-(3.70) and Eq.(3.71)-(3.84) to obtain  $\Delta T_A^1$ ,  $\Delta T_B^1$ ,  $\Delta T_C^1$  and  $\Delta T_A^2$ ,  $\Delta T_B^2$ ,  $\Delta T_C^2$ , respectively;
- step 6* Compute the search step sizes  $\beta_1^{(n)}$  and  $\beta_2^{(n)}$  from Eq.(3.87) and Eq.(3.88);
- step 7* Compute the new estimates for  $p$  and  $Bi$  from Eq.(3.51) and Eq.(3.52) and go back to *step 1* until a stopping criterion is achieved. The stopping criterion was chosen as  $\|p^{(n+1)} - p^{(n)}\| \leq \epsilon_1$ ,  $\|Bi^{(n+1)} - Bi^{(n)}\| \leq \epsilon_2$ , where  $\epsilon_1$  and  $\epsilon_2$  are prescribed tolerances which were set to  $10^{-6}$  and  $10^{-7}$ , respectively.



### 3.3.5 Implementation and numerical procedure

The direct, adjoint, and sensitivity problems are solved using a centered finite difference scheme. The following geometrical and thermophysical parameters are given:

- GaAs dimensions:  $L_t \times w_1 \times H_3 = 9mm \times 3.6mm \times 0.075mm$ ;
- Si wafer dimensions:  $L_t \times W \times H_2 = 9mm \times 9mm \times 0.3mm$ ;
- Coefficient of thermal conductivity for GaAs:  $k_{GaAs} = 0.1W/mmK$ ;
- Coefficient of thermal conductivity for Si:  $k_{Si} = 0.1421W/mmK$ ;
- Input heat flux:  $q = 12W/mm^2$ .

A Matlab code is implemented to solve the three coupled problems using a mesh of  $15 \times 11 \times 4$  for the GaAs slab and  $15 \times 25 \times 12$  for the Si substrate.

### 3.3.6 Results and discussions

The optimization of the MHP sink is performed for 4 different channel heights,  $H_1 = 75\mu m, 100\mu m, 125\mu m, 150\mu m$ . The number of channels is also varied to study the sensitivity of the heat sink performance on the number of channels. The optimum channel to fin width ratio is 1, this finding being in agreement with the results obtained by previous investigators [68], [32], [53]. The obtained aspect ratios result in reasonable fin widths and arrays of fins that can be manufactured. Distributions of optimum  $Bi$  are found for each case study, considering five values of the weighting coefficient,  $\alpha = 0.1, 0.5, 1, 5, 50$ . It is noticed that the optimum Biot number distribution decreases with increasing channel depth and increases with decreasing number of channels (see Figures 4.5-4.8). As in the planar heat sink case studied in the previous chapter,  $Bi$  decreases with the increase of cost  $\alpha$ .

The controlled and uncontrolled temperature distributions on the top surface of the Si substrate through the symmetry plane of the fin are compared for different values of the weighting coefficient  $\alpha$  (see Figures 4.9-4.12). The uncontrolled temperature is obtained using a constant Biot number,  $BI$  along the boundary, that gives the same cost as the optimal  $Bi$ . It can be noticed that the controlled temperatures display flatter profiles, resulting in smaller temperature gradients. Underneath the heat source, the controlled temperature is lower than the uncontrolled temperature. The difference between the two temperatures corresponding to the hottest point is about  $4K - 10K$ . This difference is much smaller than in the planar spreader case, suggesting that the heat transfer coefficient of a finned structure approaches by design an optimum distribution. Since the differences between the controlled and uncontrolled temperatures are small, the constant Biot number  $BI$  is used to assess the effect of the number of channels on the performance of the MHP sink. The structure with  $N = 60$  channels is taken as reference and variation percentages of  $BI$  are computed when the number of channels is changed to  $N = 58, 56$  and  $30$ , respectively (see Table 4.1). For a given number of channels no significant variations are noticed for different values of  $\alpha$ . As can be observed from Figures 4.9-4.12, for a given channel depth  $H_1$  and weighting coefficient  $\alpha$  the same temperature distributions (controlled and uncontrolled) are obtained for values of the Biot number that increase with decreasing number of channels.

For the same number of channels lower temperatures are obtained for larger values of the channel depth. By increasing the channel depth the surface exposed to convective cooling is expanded.

Comparing the thermal performance of the planar spreader studied in the previous chapter and the finned heat sinks, it can be concluded that the same temperatures can be

attained for smaller  $Bi$  using the finned heat sinks. This is due to an increase in area for heat dissipation.

### 3.4 Liquid charge corresponding to maximum heat transport capacity of the pipe

In this section we will compute the liquid charges corresponding to the maximum heat transport capacity of the MHPs having the optimum geometry found in the previous section. It is expected that the optimum  $Bi$  found in the previous section leads to an amount of heat removed from the source greater than the heat transport capacity of the MHP. The maximum heat transport capacity of the pipe is found iteratively, decreasing the optimum  $Bi$  by a quantity  $\Delta Bi^{(i)} = i \times 10^{-7} \times Bi$ ,  $i = 0..10^7$ .

$$Q_{inMHP}^{(i)} = q_{in} (H_1 + l) \int_0^{L_e} (Bi - \Delta Bi^{(i)}) T_w dy. \quad (3.125)$$

In the above equation  $q_{in}$  is the heat flux entering the heat sink and  $T_w$  is the channel wall temperature. The maximum heat applied to the MHP for which the pressure gradients  $\frac{dP_l}{dy}$ ,  $\frac{dP_v}{dy}$  do not change signs along the evaporator and adiabatic sections, and the meniscus radius at the end of the adiabatic section does not exceed the  $r_{max}$  value (see Eq.(3.27)) is the maximum heat transport capacity of the MHP. A new optimum  $Bi$  is computed taking the maximum heat transport capacity of the pipe as the input heat for the heat sink. The liquid charge is found by adding the amount of liquid in the evaporator, adiabatic section, and condenser and the amount of liquid that vaporizes:

$$\begin{aligned}
m_{liquid} &= \left( 2 \int_0^{L_e+L_a} A_l dy + 2lH_1 (W - L_e - L_a) \right) \rho_l \\
&+ \left( 2lH_1 (L_e + L_a) - 2 \int_0^{L_e+L_a} A_l dy \right) \rho_v.
\end{aligned} \tag{3.126}$$

### 3.4.1 Computational procedure

The algorithm used in computing the optimum liquid charge may be summarized as follows:

*step 1* For a given  $r|_{y=0} = r_0$  set the heat entering the MHP to  $Q_{inMHP}^0$  ( $i=0$ );

*step 2* Solve the transport Eq.(3.44)-(3.48) for the MHP to obtain the distributions for  $P_l$ ,  $P_v$ ,  $U_l$ ,  $U_v$ , and  $r$ ;

*step 3* Check the conditions for the pressure gradients and the radius of curvature:

$$\frac{dP_l}{dy} < 0, \quad \frac{dP_v}{dy} > 0, \quad r \leq r_{crit} \quad y \leq L_e + L_a; \tag{3.127}$$

*step 4* If all of the above conditions are satisfied, then the heat transport capacity of the MHP is  $Q_{max} = Q_{inMHP}^i$ , otherwise increase  $\Delta Bi$  (set the input heat to  $Q_{inMHP}^{(i+1)}$ ) and repeat *step 2-step 4* until the above conditions are satisfied simultaneously;

*step 5* Take  $Q_{max}$  as the input heat for the MHP heat sink and compute the optimum  $Bi$  using a conjugate gradient algorithm, similar to those presented in the previous sections;

*step 6* Compute the liquid charge using Eq.(3.126).

### 3.4.2 Results and discussions

In this analysis water was considered as working fluid. The following geometrical and thermophysical parameters are used:

- MHP height:  $H_1 = 75\mu m, 100\mu m, 125\mu m, 150\mu m$ ;
- MHP width:  $l = pH_1$ , where  $p$  is the optimum aspect ratio found in the previous section;
- MHP length:  $W = 9mm$ ;
- Evaporator length:  $L_e = 1.8mm$ ;
- Adiabatic section length:  $L_a = 3mm$ ;
- Liquid density:  $\rho_l = 983.284kg/m^3$ ;
- Vapor density:  $\rho_v = 0.130366kg/m^3$
- Liquid viscosity:  $\mu_l = 466.4 \cdot 10^{-6}kg/ms$ ;
- Vapor viscosity:  $\mu_v = 10.93 \cdot 10^{-6}kg/ms$ ;
- Surface tension:  $\sigma = 0.06624N/m$ ;
- Contact angle:  $\theta = \pi/6$ ;
- Tilt angle:  $\theta_1 = \pi/18$
- Latent heat of vaporization:  $h_{fg} = 2358.48kJ/kg$ .

The properties for water are taken at  $55^{\circ}C$ .

The transport equations (3.44)-(3.48) for the MHP are solved using a Runge-Kutta scheme. Distributions of the meniscus radius over the axial direction for the evaporator and adiabatic sections are shown in Figure 4.13. These distributions correspond to the maximum heat transport capacity of MHP sinks with  $N = 60$  channels and different channel depths. It is noticed that the meniscus radius increases with increasing channel depth. Figures 4.14-4.17 show the velocity distributions of the liquid and vapor phases computed for the maximum heat transport capacity of the above mentioned heat sink designs. Higher velocities are achieved for greater channel depths. The increase of radius of curvature in the axial direction causes an increase in liquid cross section area in this direction and a decrease in vapor area. Consequently the vapor velocity increases in  $y$  direction while the liquid velocity decreases. The vapor velocity is about two orders of magnitude greater than the liquid velocity. This is due to the high liquid/vapor density ratio. Pressure distributions for the liquid and vapor phases are presented in Figure 4.18. The vapor pressure drop is about one order of magnitude less than that of the liquid phase.

Optimal distributions of  $Bi$  corresponding to the maximum heat transport capacity of the MHP are presented in Figures 4.19-4.22 for heat sinks with different number of channels and different channel depths. The new optimum  $Bi$  represents only a fraction of the optimum  $Bi$  computed in the previous section ('ideal'  $Bi$ ). For a given number of channels the optimum  $Bi$  increases with increasing channel depth  $H_1$ . Values of the liquid charge corresponding to the maximum heat transport capacity of the pipe are plotted in Figure 4.25. For a given number of channels the optimum liquid charge increases with increasing channel depth. Small increases in the liquid charge are noticed for increasing

weighting coefficient  $\alpha$ . The optimum liquid charge increases with decreasing number of channels.

The maximum heat transport capacity is expressed as a fraction  $q_r$  of the input heat. Variations of the MHP heat transport capacity for different design parameters are shown in Figure 4.27. For a given number of channels, the heat transport capacity increases with increasing channel depth and weighting coefficient  $\alpha$ .

The sensitivity of the MHP performance on the value of the meniscus radius at  $y = 0$  is also studied. Four values of  $r_0$  were considered,  $7.7\mu m$ ,  $8\mu m$ ,  $8.5\mu m$  and  $9.5\mu m$ . The results obtained for the optimum liquid charge (see Figure 4.23) and maximum heat transport capacity (see Figure 4.24) do not display significant variations when  $r_0$  is varied within 25%.

### 3.5 Conclusions

In this work the performance of several configurations of rectangular cross section micro heat pipe sinks using water as working fluid was investigated. The geometry and the convective heat transfer coefficient were optimized. The critical path to an optimum design started with the analysis of a planar heat spreader for which an optimum convective heat transfer coefficient corresponding to a maximum amount of heat removed from a heat source was obtained. An optimal control technique was employed to solve this problem, using Biot number as control. The existence and uniqueness of a solution and of an optimal control were proven. Then the analysis was extended to finned heat sinks for which an optimization of the convective heat transfer coefficient and the aspect ratio was performed.

The last part of this study focused on obtaining the amount of liquid charge corresponding to the maximum heat transport capacity of the micro heat pipes.

For the planar spreader, distributions of the Biot number corresponding to different values of the weighting coefficient  $\alpha$  were presented, showing that  $Bi$  decreases with increasing  $\alpha$ . The greater the value assigned to  $\alpha$ , the greater the *cost* of employing a control, and the smaller the contribution of convective cooling. Controlled and uncontrolled temperature distributions were compared. The controlled temperatures displayed lower and flatter profiles than the uncontrolled temperatures. The difference between the two profiles increased with increasing penalty parameter  $\alpha$ .

A similar optimal control technique was used to optimize the geometry and the convective coefficient of finned heat sinks. The results show that the optimum aspect ratio corresponds to a channel to fin width ratio equal to 1. The distributions of the optimum Biot number are lower than in the case of a planar spreader, due to an increase in heat transfer area. An analysis of heat sink configurations with different channel depths, i.e.  $75\mu m$ ,  $100\mu m$ ,  $125\mu m$ , and  $150\mu m$ , showed that the performance of the heat sink increases with increasing channel depth. The performance sensitivity on the number of channels was studied. The sink with 60 channels was taken as reference and computations of the variation percentage of Biot number were performed when the number of channels was changed to 58, 56, and 30. When the number of channels was reduced to half, the Biot number was increased by 35%-43%, suggesting that the performance of a heat sink increases with increasing channel density.

The maximum heat transport capacities of MHP sinks with an optimum geometry were computed, and found to be about 5% – 15% of the original input heat flux of  $12W/mm^2$ , i.e.



between  $0.6W/mm^2$  and  $1.8W/mm^2$ . The heat transport capacity increases with increasing channel density and increasing aspect ratio. The liquid charge found was about 9% – 11% (see Figure 4.26) of the pipe volume.

The algorithm used in computing the liquid charge can be applied to any working fluid. The only change that has to be made in the simulation consists in replacing the thermophysical properties of water with the ones corresponding to the new working fluid. For applications where the removal of higher heat fluxes is necessary, different working fluids have to be used, such as mercury [44].

This study can provide guidance and a methodology for design of efficient heat sinks using micro heat pipes. The design procedure can be followed as given:

- Choose the depth of the micro-channels. Typical values are in the range of  $100\mu m$ , but can vary from  $50\mu m$  up to several hundred microns. The determining factor lies in the thickness of the spreader and the location of heat generation. In general, the channels should be as close to the heat source as possible.
- For the given dimensions of the heat sink, length by width (with the width being defined as the dimension transverse of the direction of the heat pipe channel axial dimension) prescribe the number of channels and find the channel width using the recommended pitch ratio (channel to fin width ratio) of 1 as described in section 3.3, e.g. for a  $10mm$  (width) by  $10mm$  (length) heat spreader with a  $0.5mm$  border on all edges and  $100\mu m$  deep channels, if the recommended number of channels is 60 across the width, then the channel width is  $75\mu m$ . The number of channels is selected considering the amount of heat that has to be dissipated. For example, the above mentioned configuration is able to handle a heat flux of  $0.9W/mm^2$  (see Figure 4.27).

- The corresponding liquid charge can be found using the algorithm described in section 3.4.1. This value is somewhere between 9 and 11%.

As designers we look for a heat sink configuration able to spread the largest amount of heat for a particular application. From the study presented earlier the best performance was achieved by a heat sink with 60 channels using a channel depth of  $150\mu m$ , which was able to handle a heat flux of  $1.8W/mm^2$  for a 11% volume charge.

CHAPTER 4

APPENDIX

Table 4.1: Variation percentage of  $BI$  for different number of channels

|          | $H_1 = 75\mu m$ | $H_1 = 100\mu m$ | $H_1 = 125\mu m$ | $H_1 = 150\mu m$ |
|----------|-----------------|------------------|------------------|------------------|
| $N = 58$ | 1.8124%         | 1.9558%          | 2.1194%          | 2.2216%          |
| $N = 56$ | 3.8110%         | 3.9912%          | 4.1710%          | 4.3048%          |
| $N = 30$ | 34.9441%        | 39.3297%         | 40.7426%         | 43.2075%         |

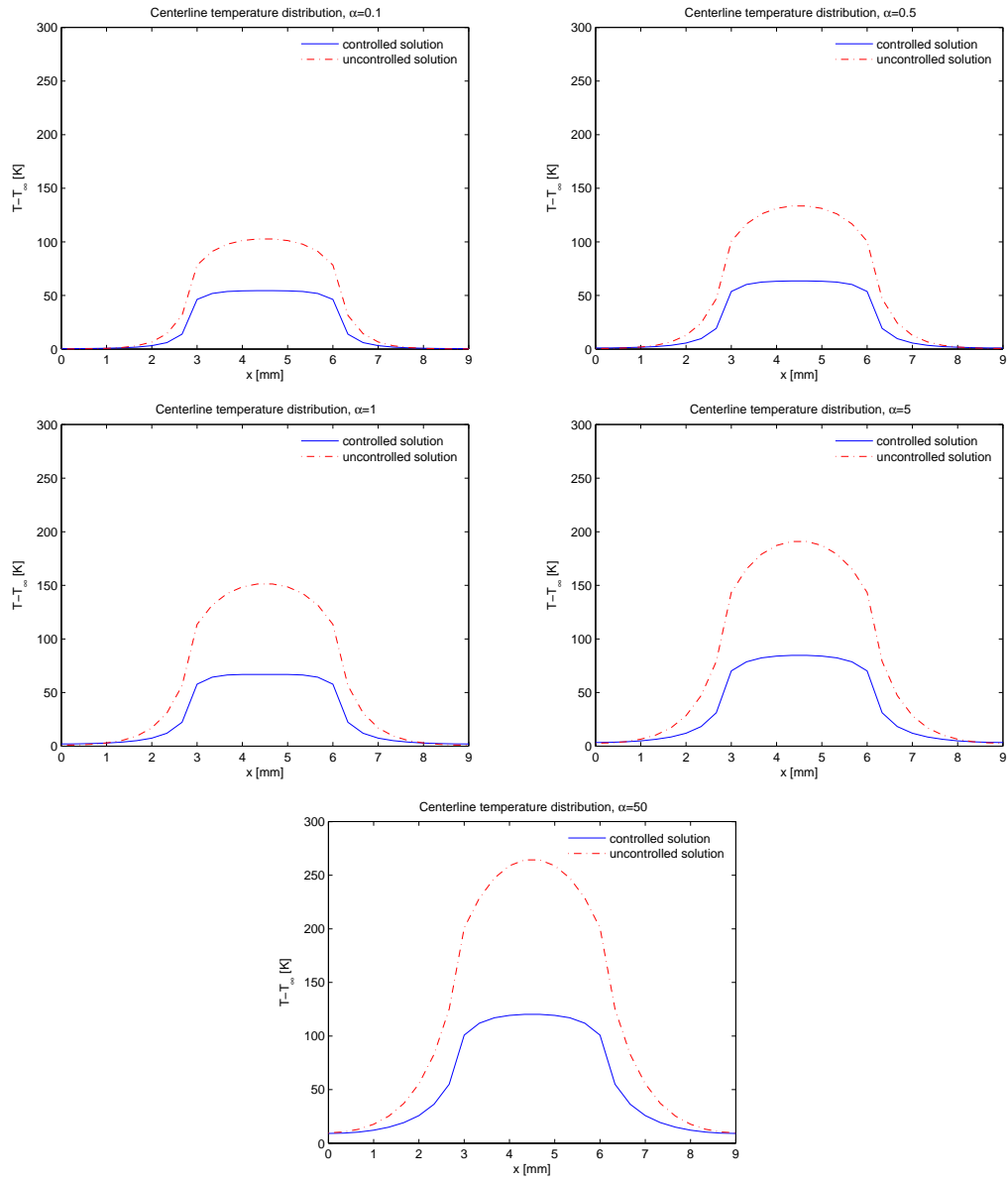


Figure 4.1: Graphs of controlled and uncontrolled solutions for different values of  $\alpha$ .

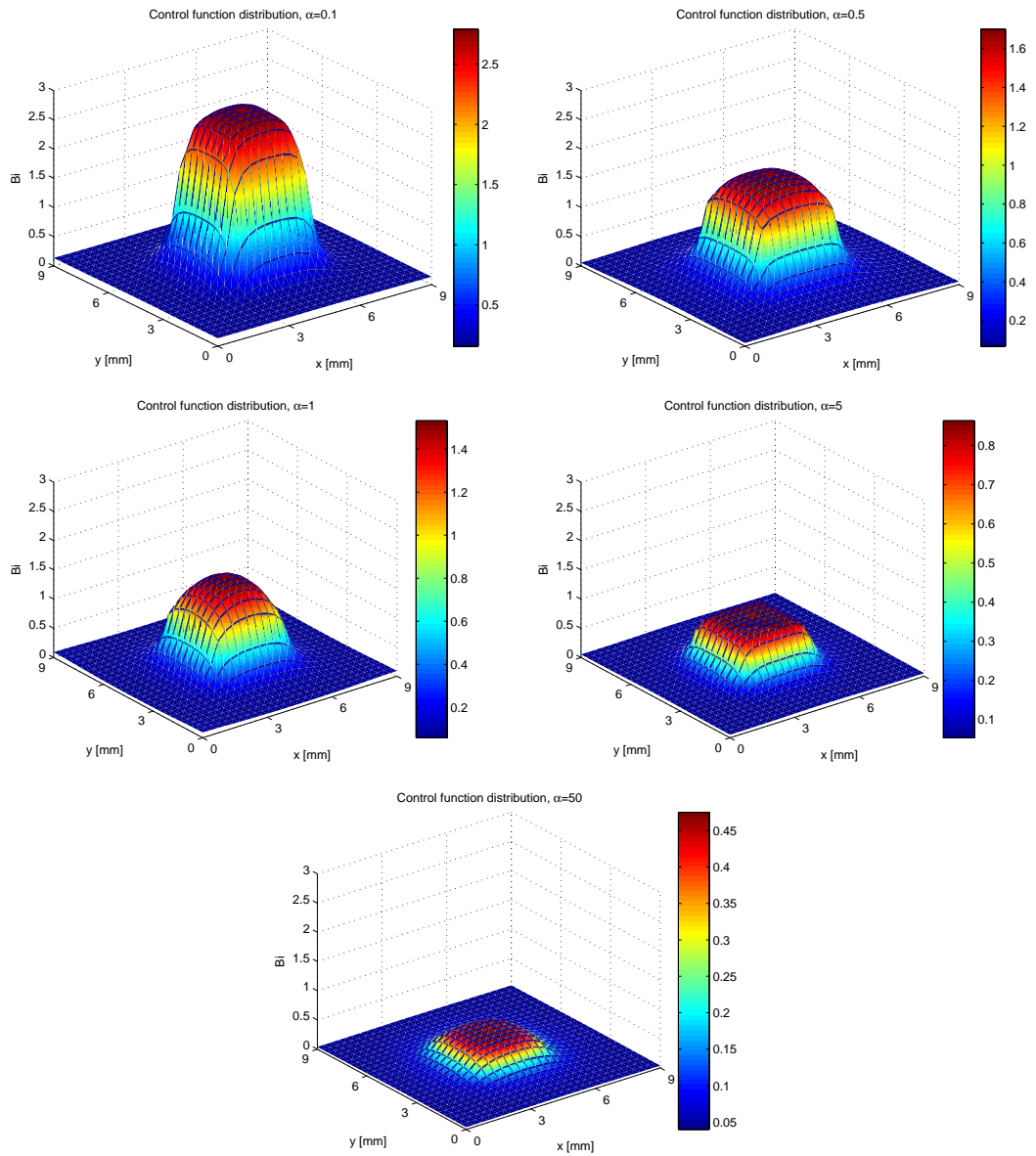


Figure 4.2: Distributions of  $Bi$  for different values of  $\alpha$ .

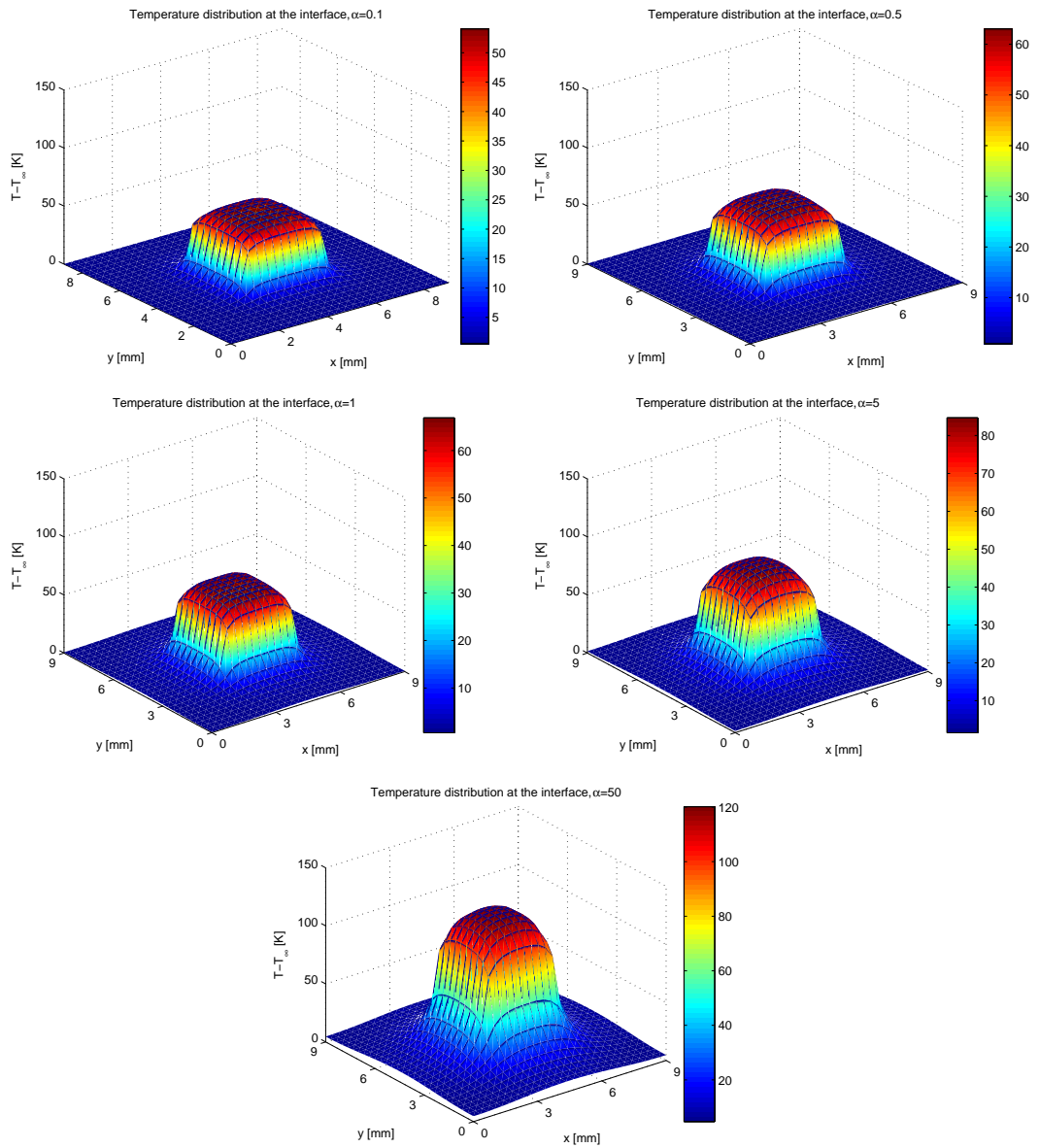


Figure 4.3: Distributions of  $T - T_\infty$  at the chip-spreader interface for different values of  $\alpha$ .

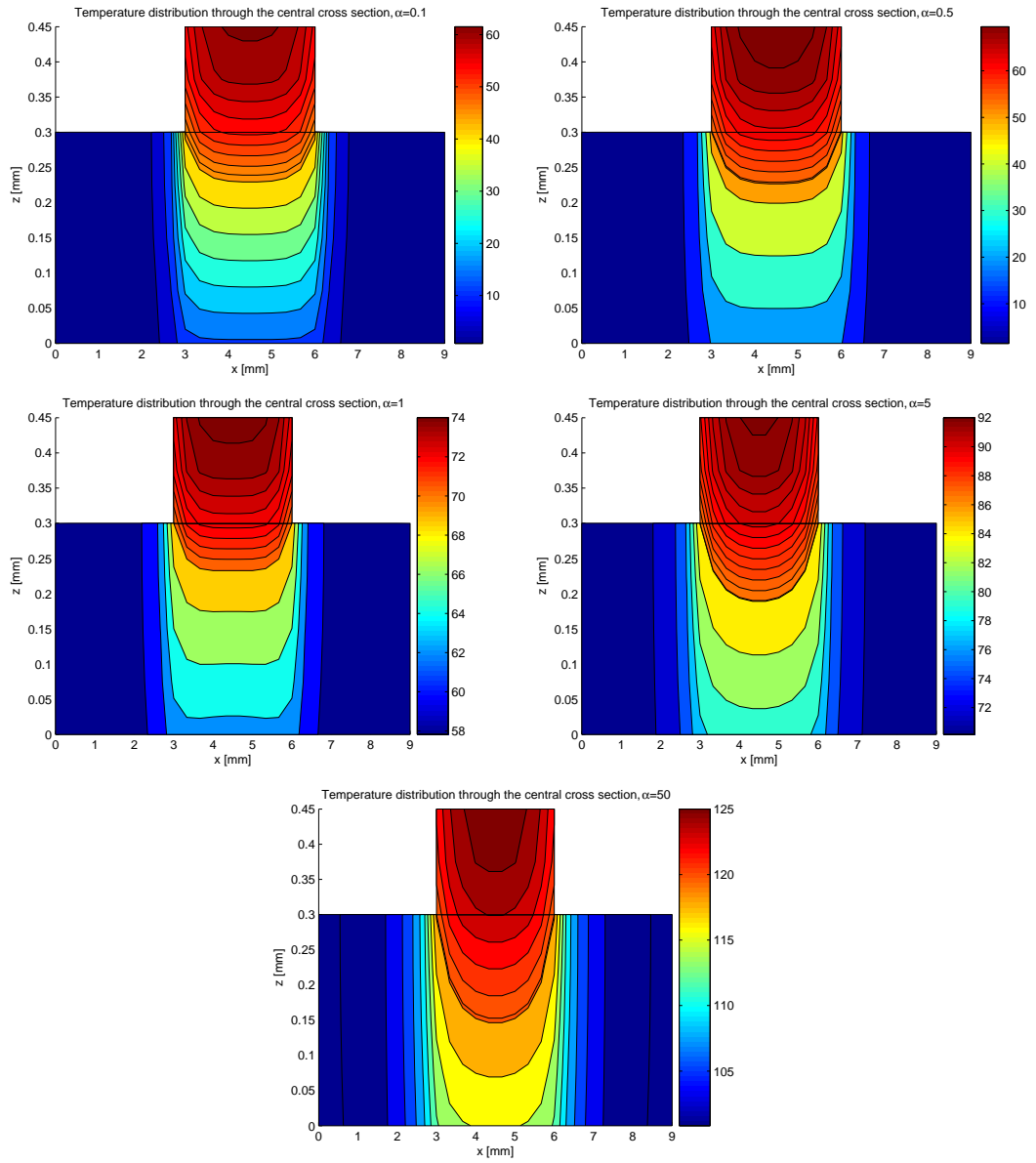


Figure 4.4: Distributions of  $T - T_\infty$  through a vertical symmetry plane for different values of  $\alpha$ .

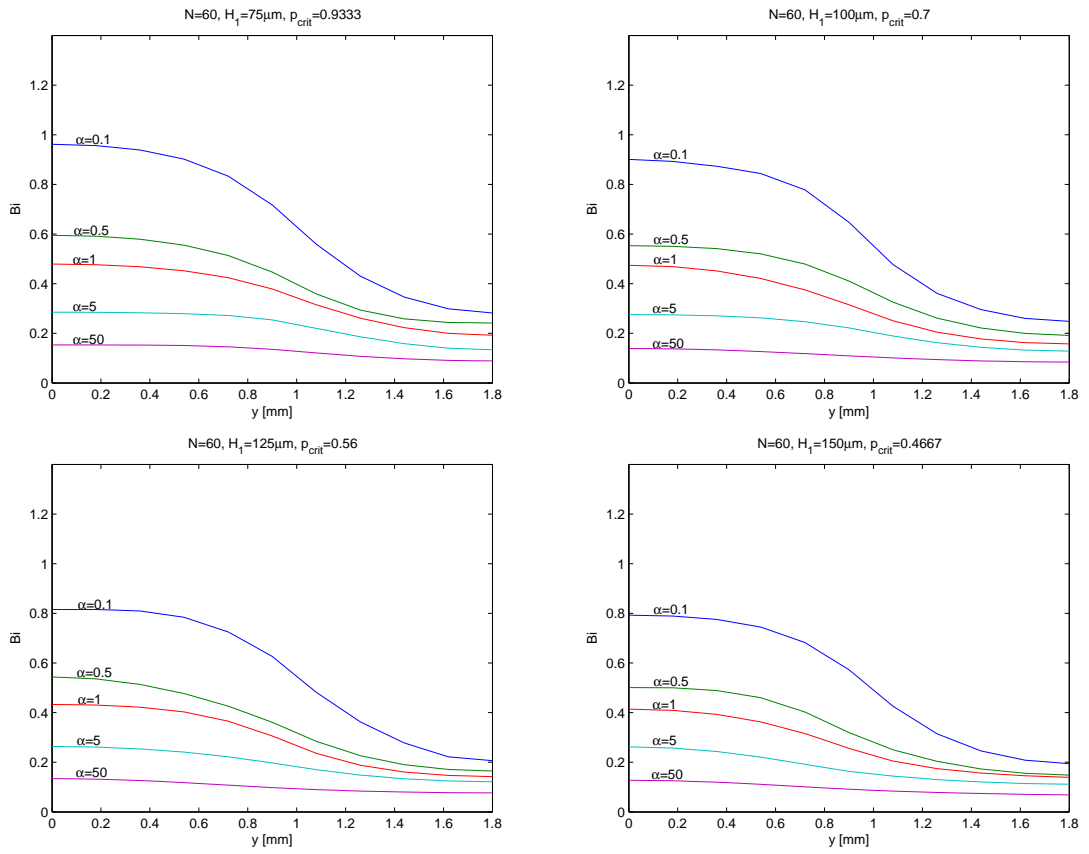


Figure 4.5: Distributions of optimal  $Bi$  corresponding to  $N = 60$  and different channel depths.



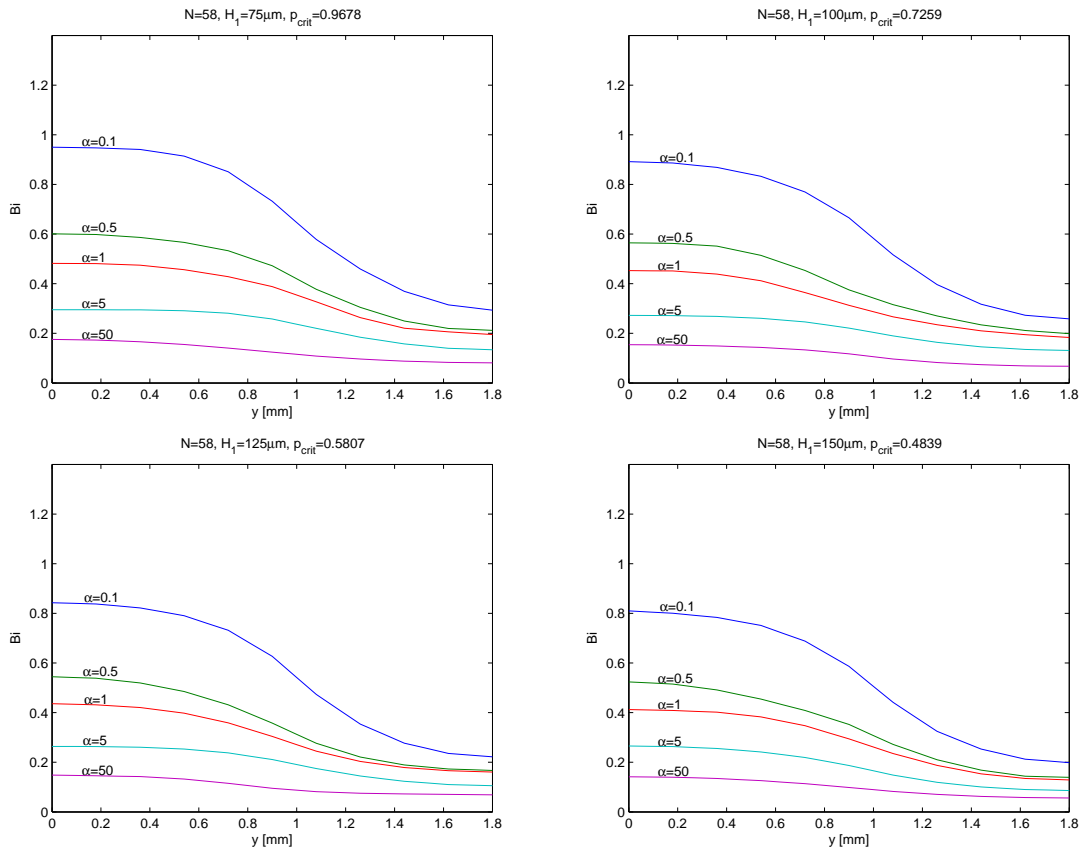


Figure 4.6: Distributions of optimal  $Bi$  corresponding to  $N = 58$  and different channel depths.

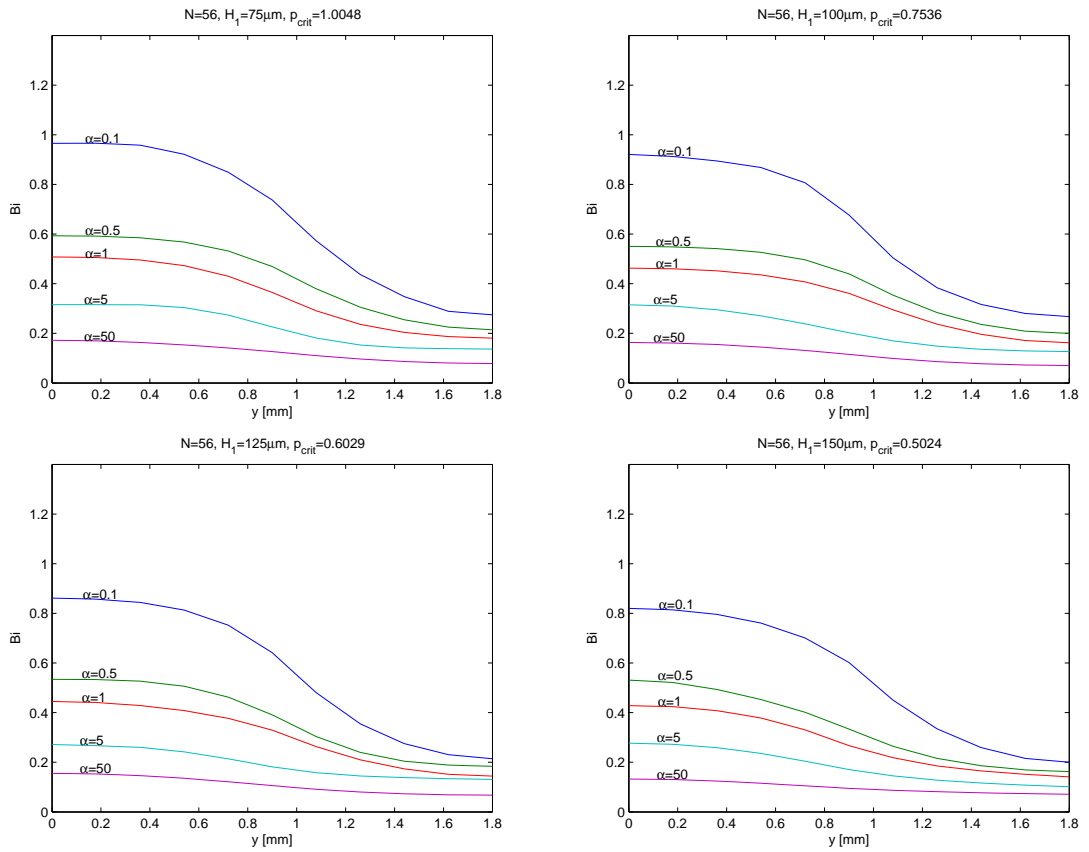


Figure 4.7: Distributions of optimal  $Bi$  corresponding to  $N = 56$  and different channel depths.

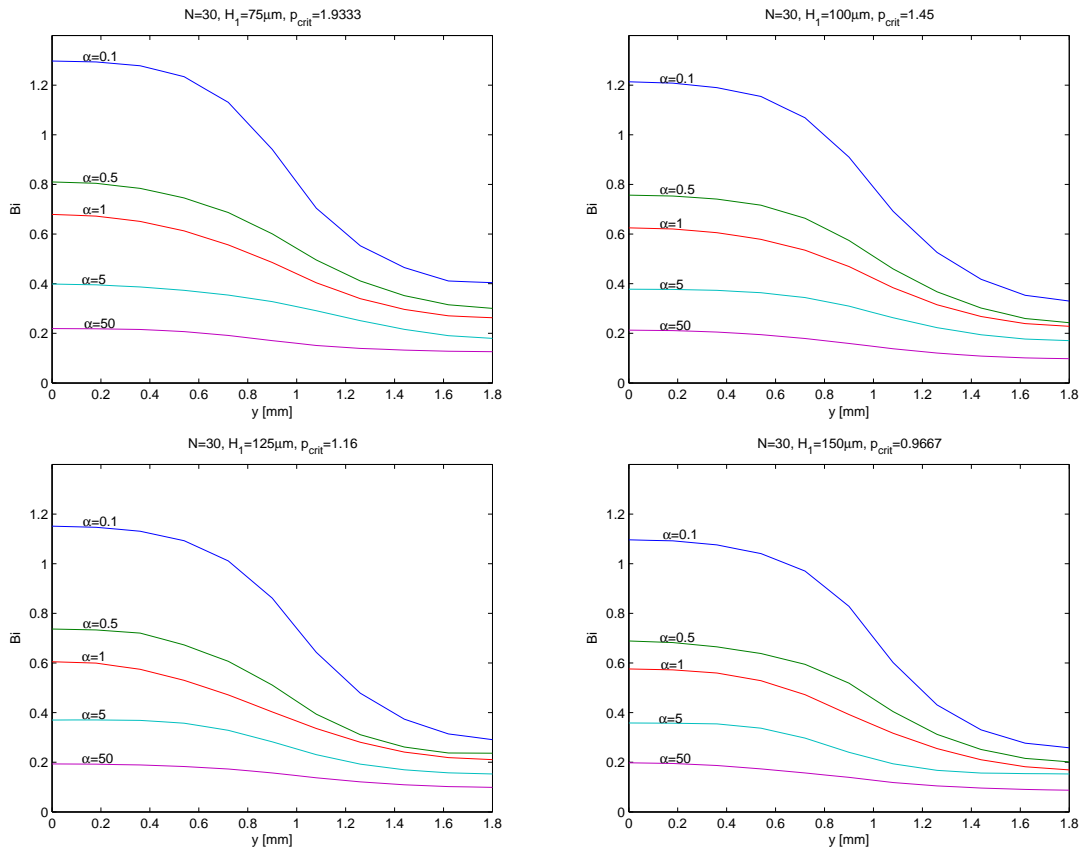


Figure 4.8: Distributions of optimal  $Bi$  corresponding to  $N = 30$  and different channel depths.

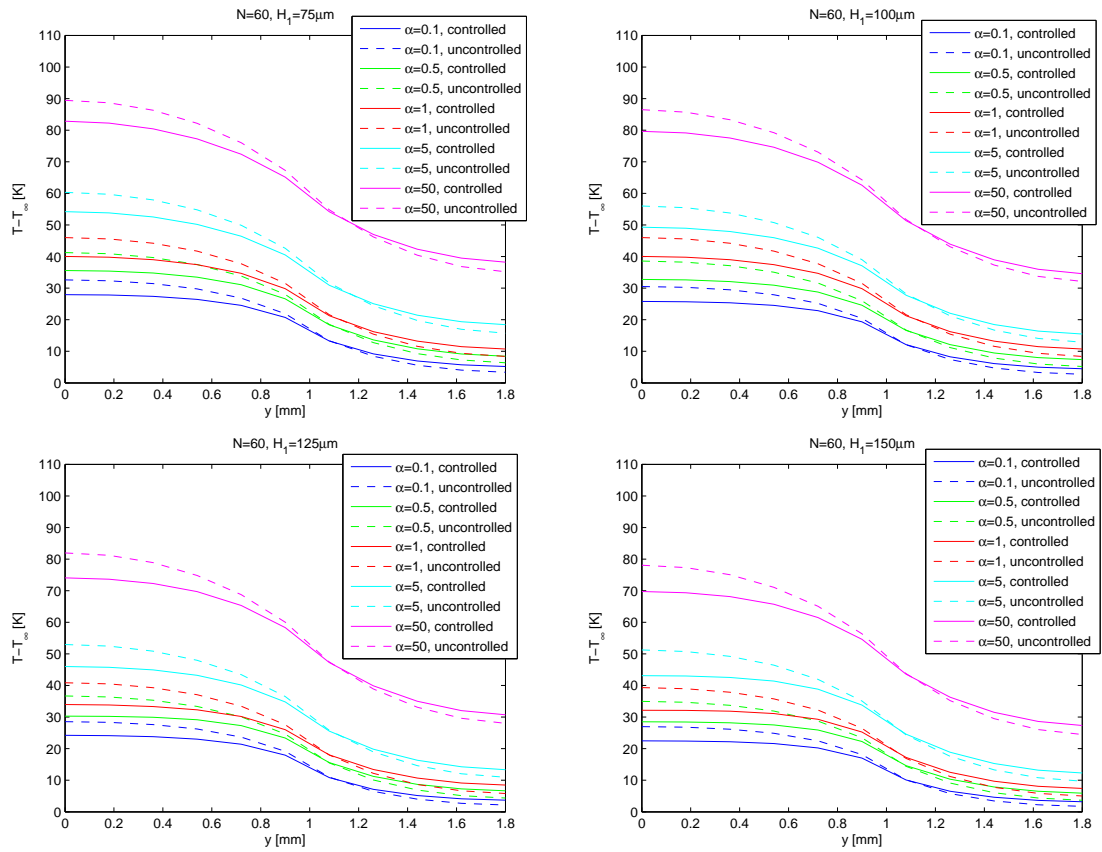


Figure 4.9: Temperature distributions  $T - T_\infty$  corresponding to  $N = 60$ .

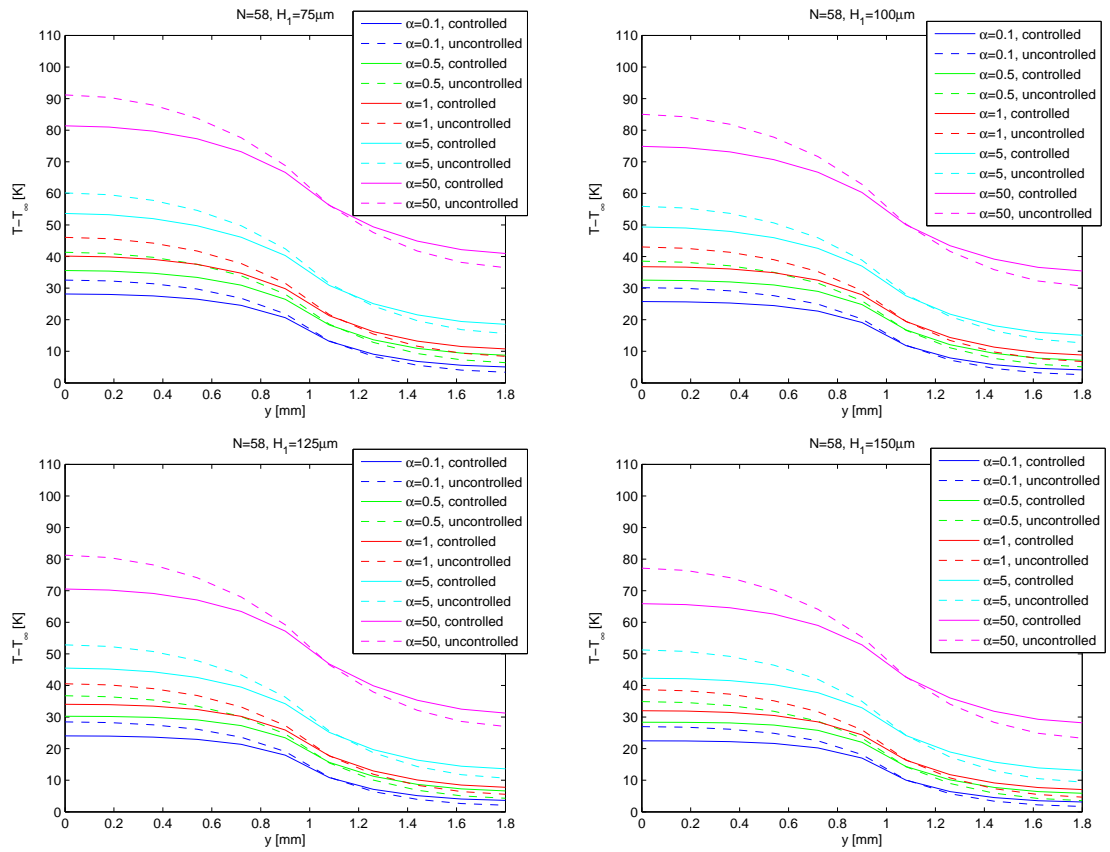


Figure 4.10: Temperature distributions  $T - T_\infty$  corresponding to  $N = 58$ .

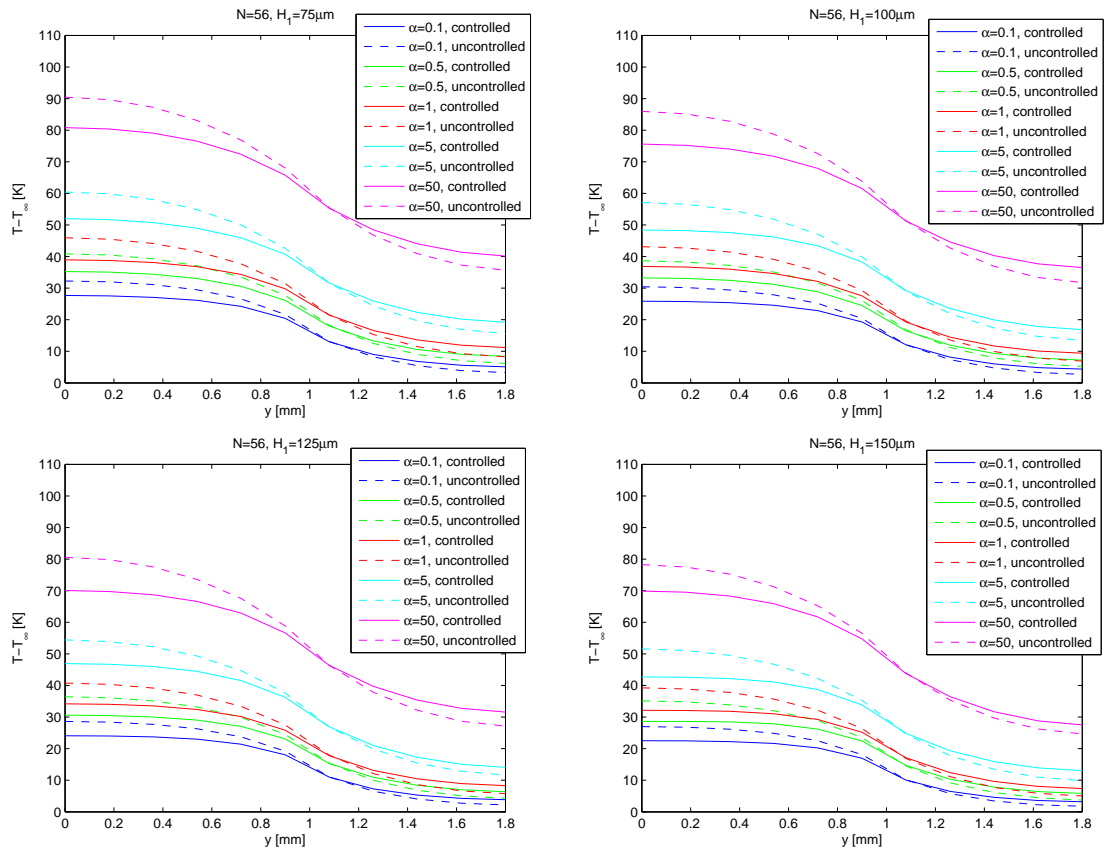


Figure 4.11: Temperature distributions  $T - T_\infty$  corresponding to  $N = 56$ .

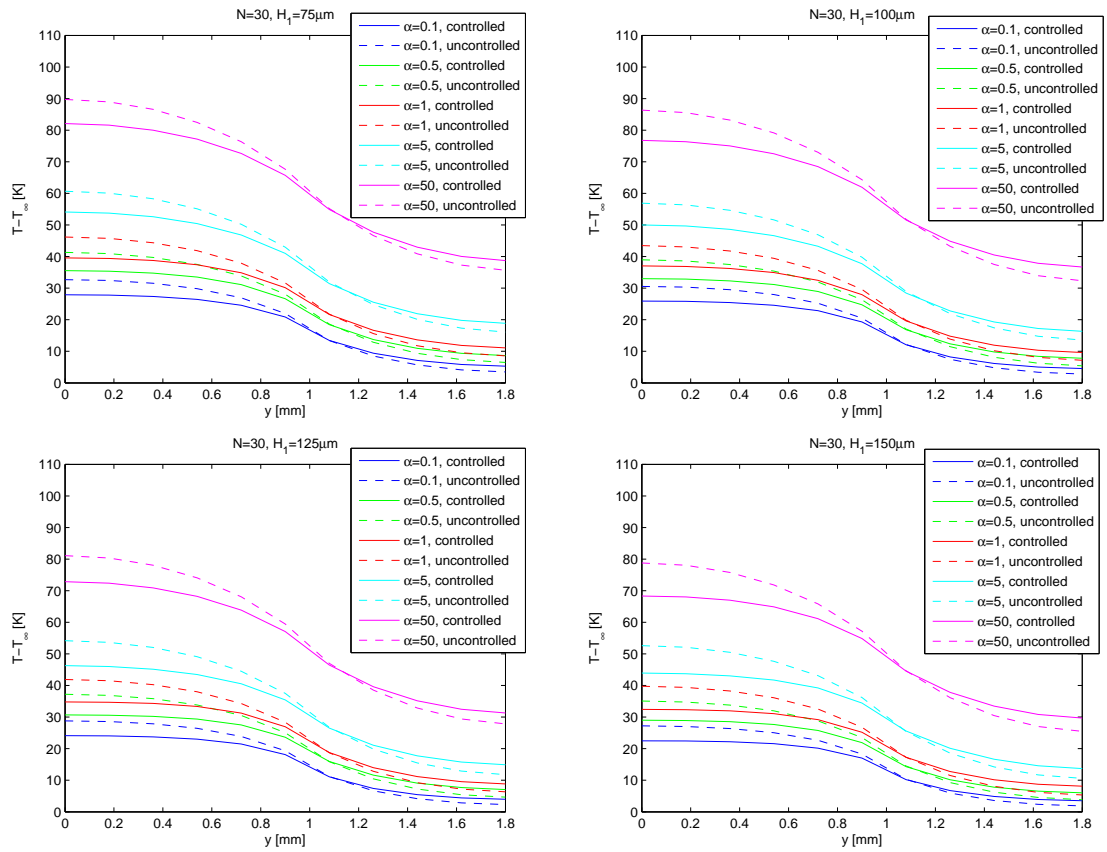


Figure 4.12: Temperature distributions  $T - T_\infty$  corresponding to  $N = 30$ .

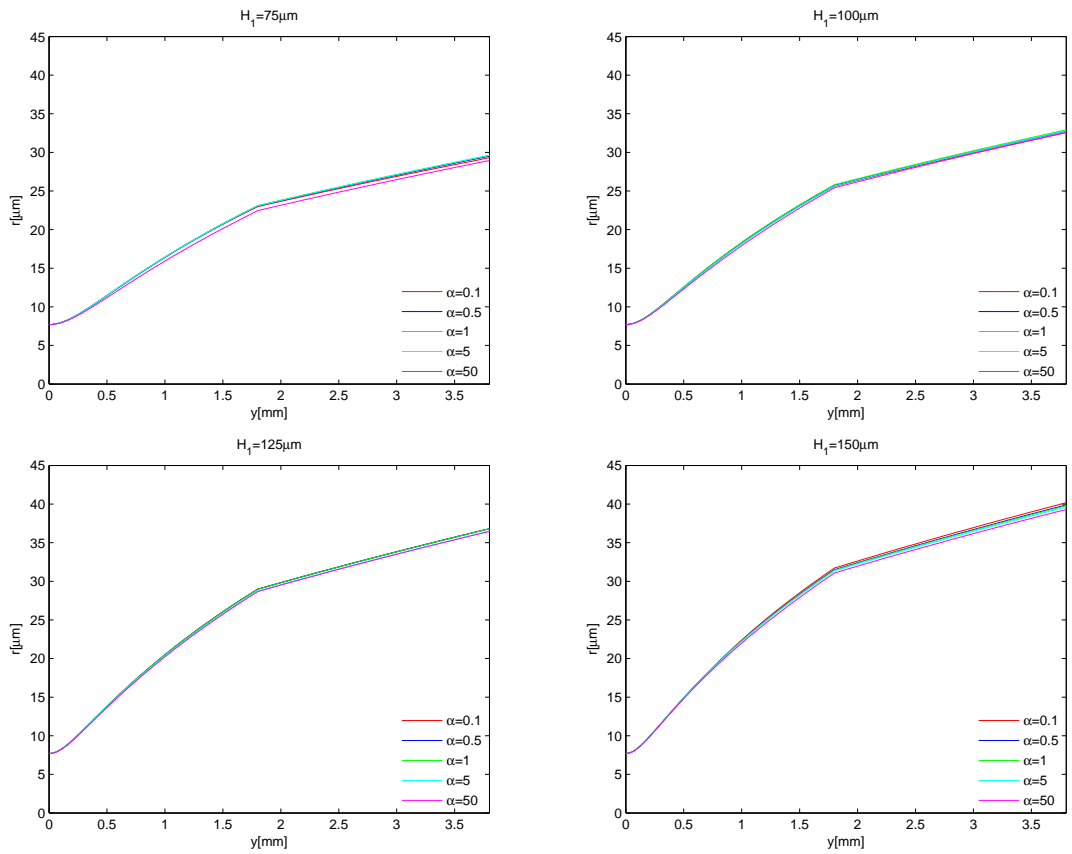


Figure 4.13: Distribution of the meniscus radius for different values of  $\alpha$  and channel depths ( $N = 60$ ).



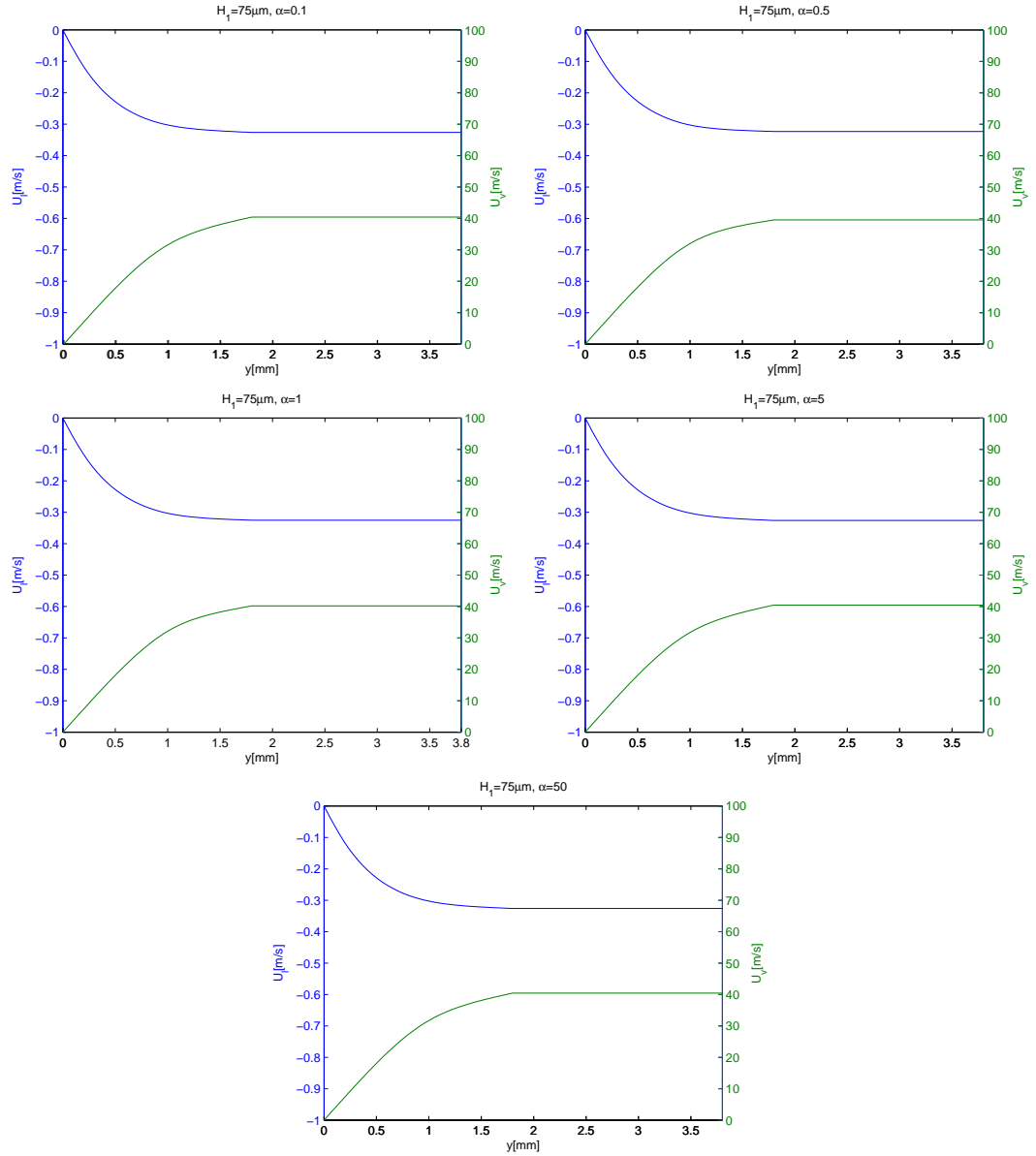


Figure 4.14: Distributions of the liquid and vapor velocities for  $H_1 = 75 \mu\text{m}$  and different values of  $\alpha$  ( $N = 60$ ).

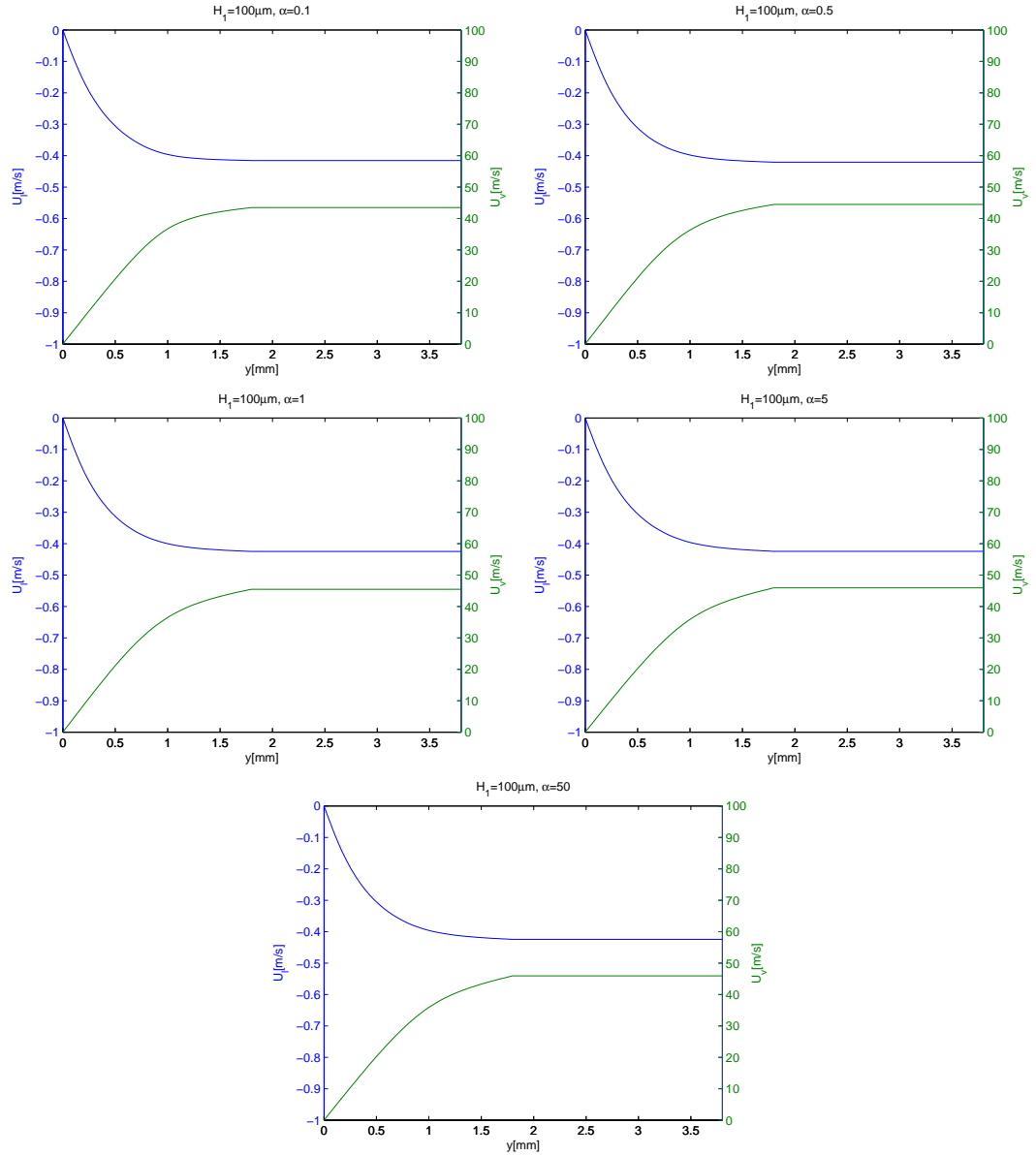


Figure 4.15: Distributions of the liquid and vapor velocities for  $H_1 = 100 \mu\text{m}$  and different values of  $\alpha$  ( $N = 60$ ).

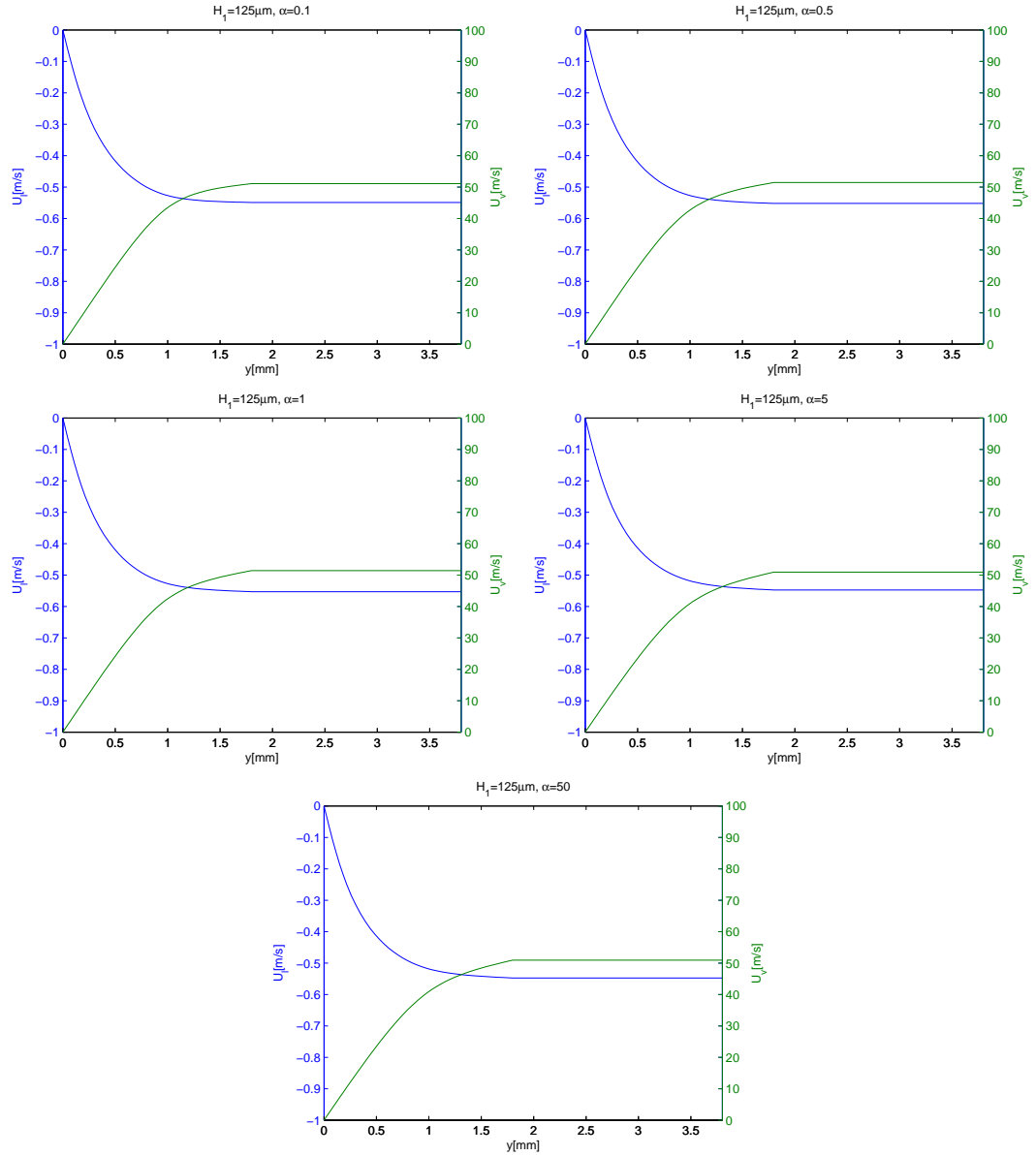


Figure 4.16: Distributions of the liquid and vapor velocities for  $H_1 = 125 \mu\text{m}$  and different values of  $\alpha$  ( $N = 60$ ).

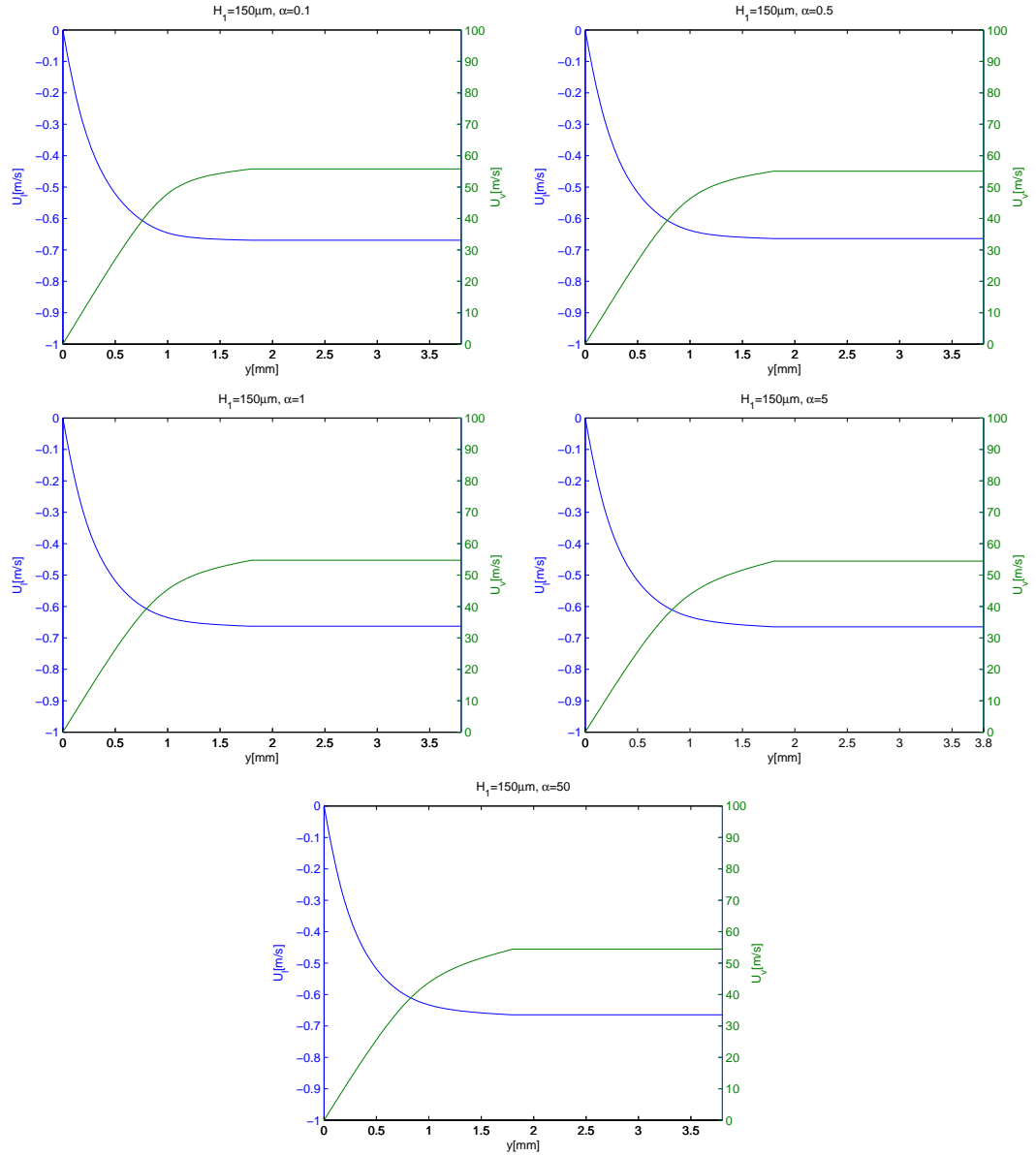


Figure 4.17: Distributions of the liquid and vapor velocities for  $H_1 = 150 \mu\text{m}$  and different values of  $\alpha$  ( $N = 60$ ).

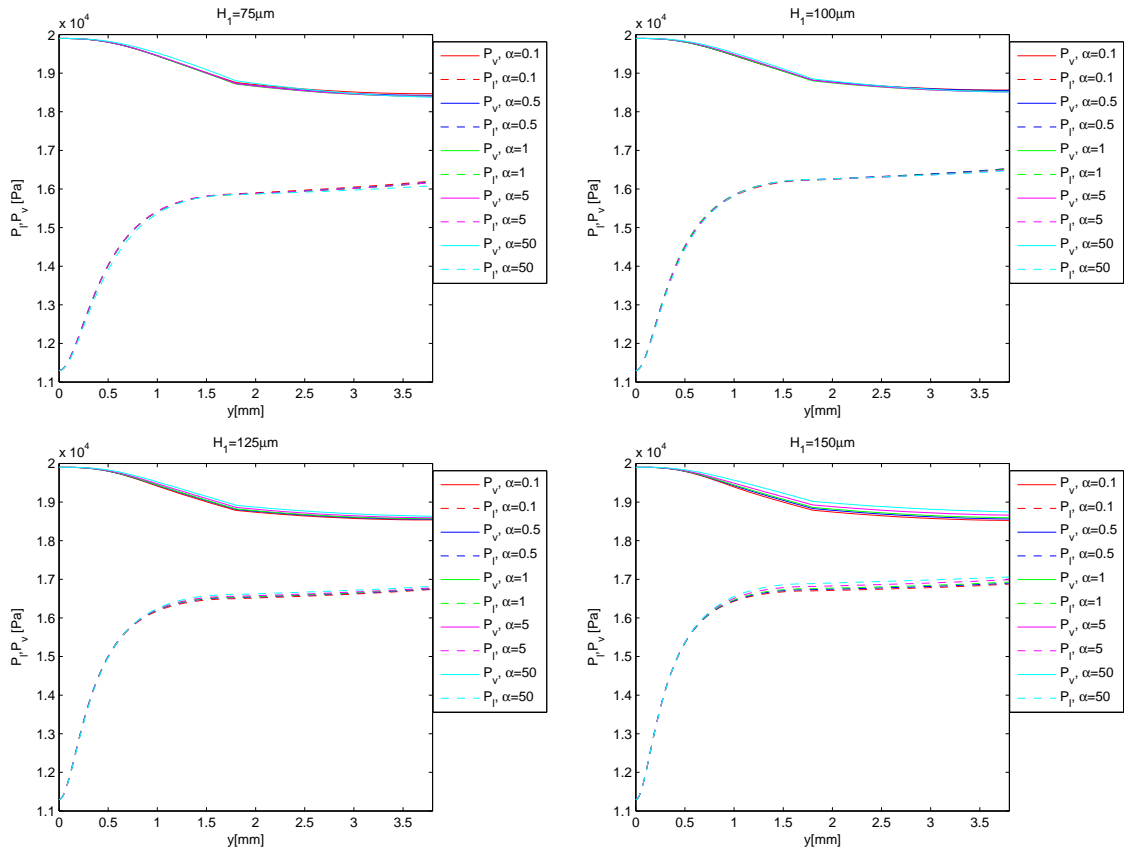


Figure 4.18: Distributions of the liquid and vapor pressures for different values of  $\alpha$  and channel depths ( $N = 60$ ).

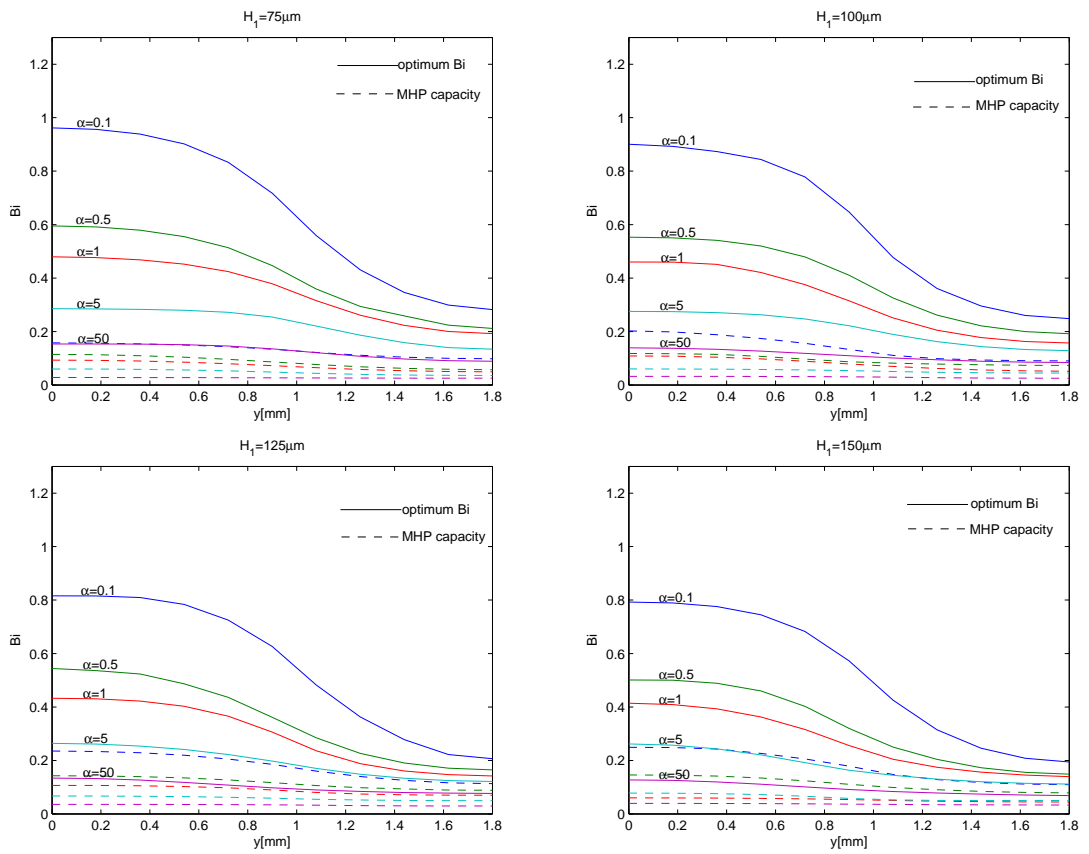


Figure 4.19: Distributions of the 'ideal' optimum  $Bi$  and the optimum  $Bi$  corresponding to the maximum heat transport capacity of the pipe, for  $N = 60$  and different channel depths.

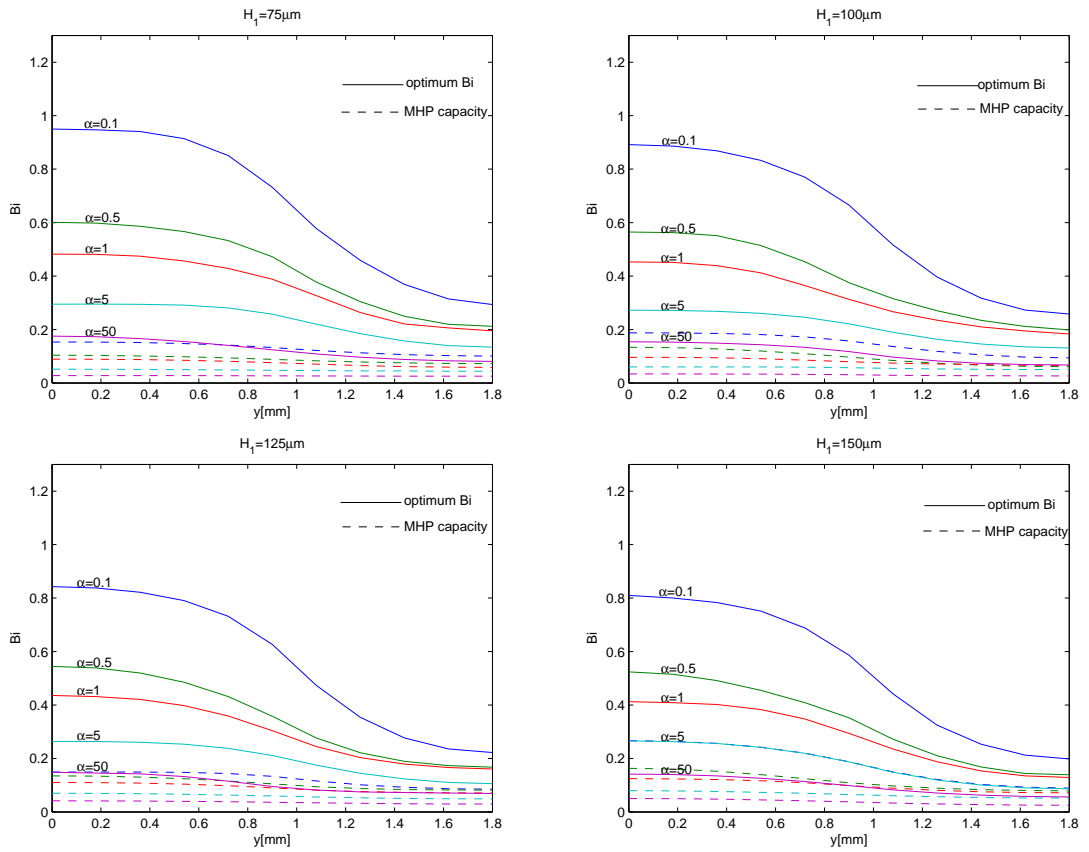


Figure 4.20: Distributions of the 'ideal' optimum  $Bi$  and the optimum  $Bi$  corresponding to the maximum heat transport capacity of the pipe, for  $N = 58$  and different channel depths.

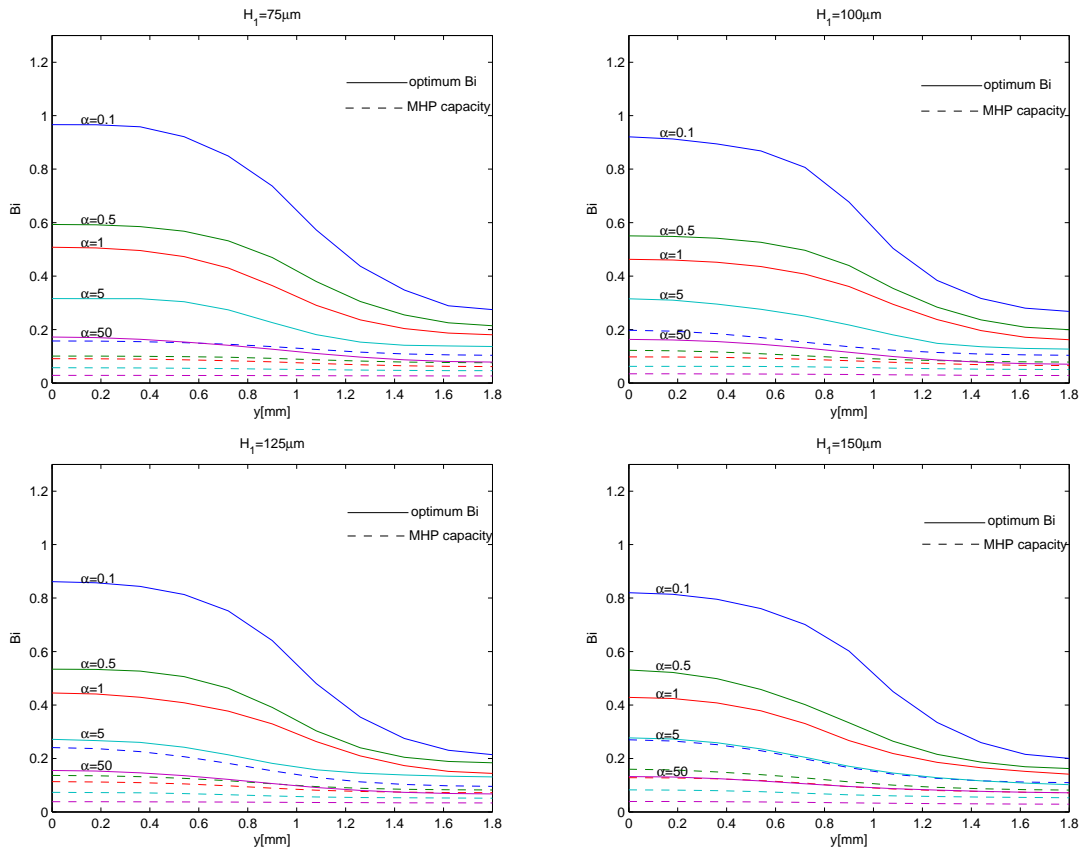


Figure 4.21: Distributions of the 'ideal' optimum  $Bi$  and the optimum  $Bi$  corresponding to the maximum heat transport capacity of the pipe, for  $N = 56$  and different channel depths.



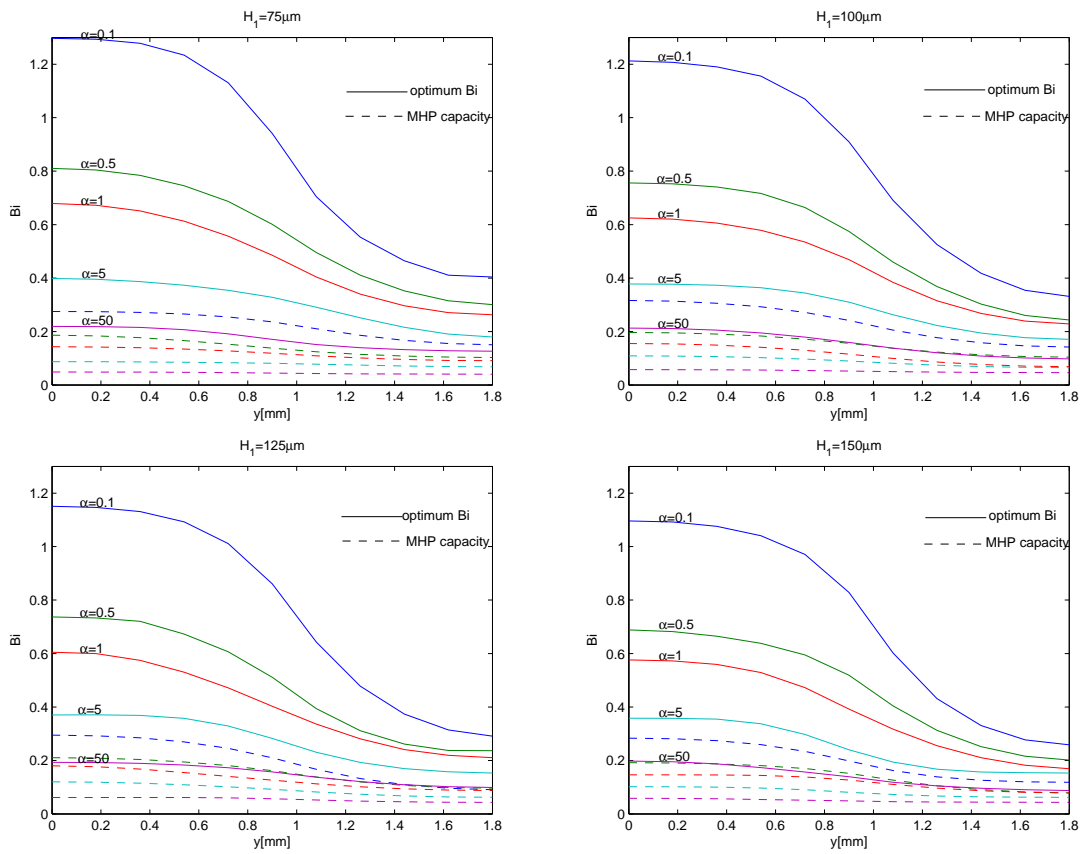


Figure 4.22: Distributions of the 'ideal' optimum  $Bi$  and the optimum  $Bi$  corresponding to the maximum heat transport capacity of the pipe, for  $N = 30$  and different channel depths.

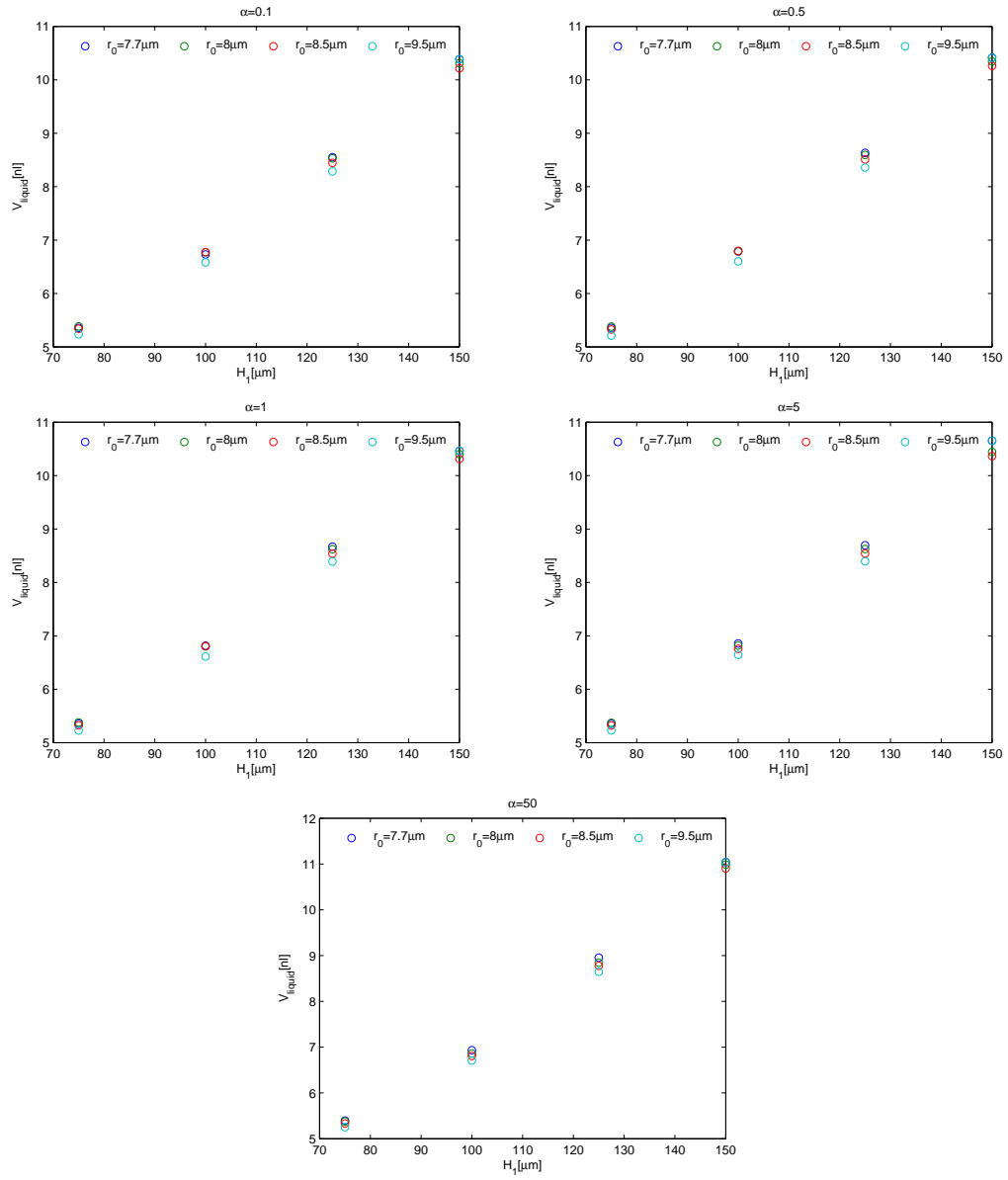


Figure 4.23: Variations of the liquid charge with  $r_0$  for different channel depths ( $N = 60$ ).

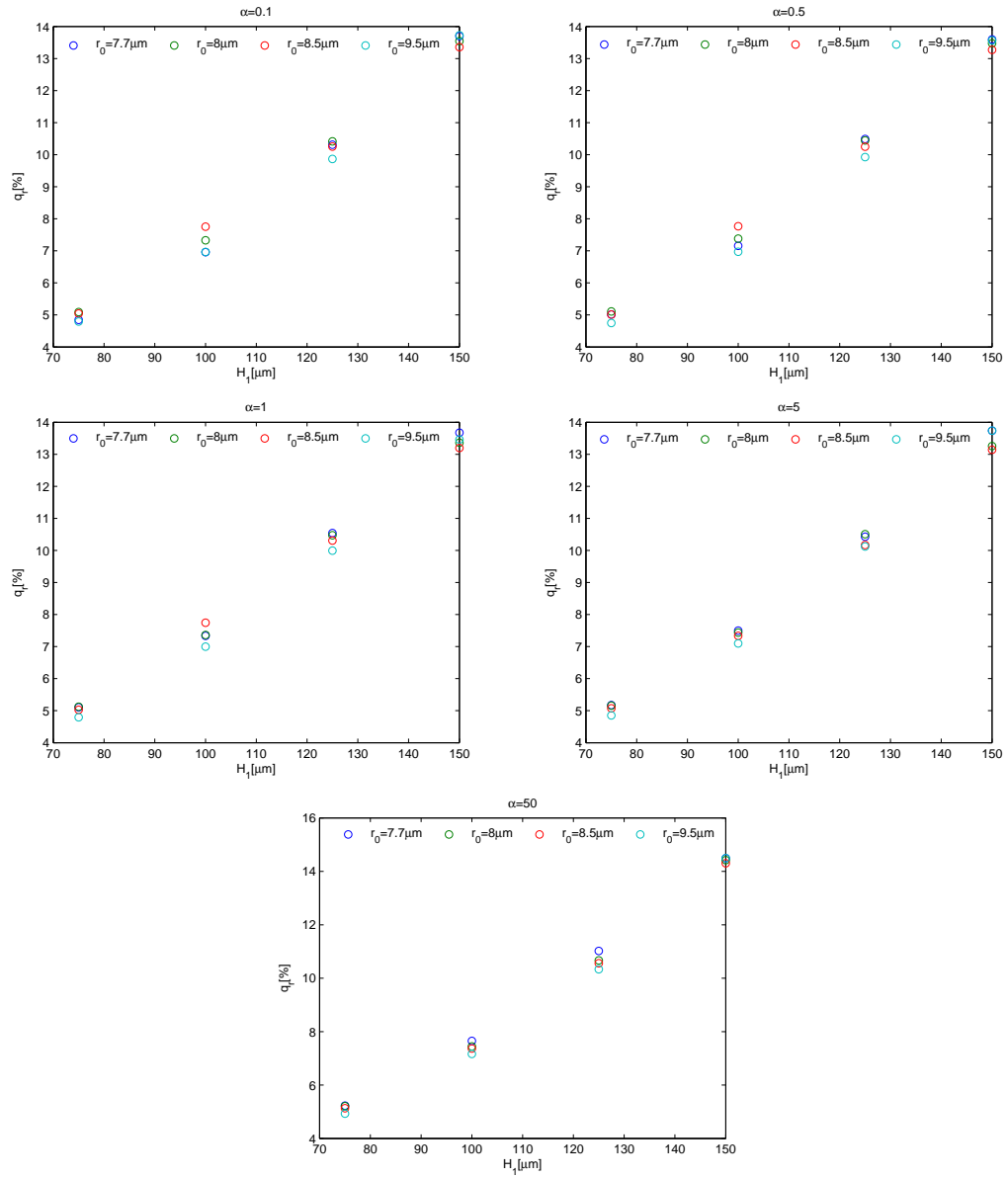


Figure 4.24: Variations of MHP heat transport capacity with  $r_0$  for different channel depths ( $N = 60$ ).

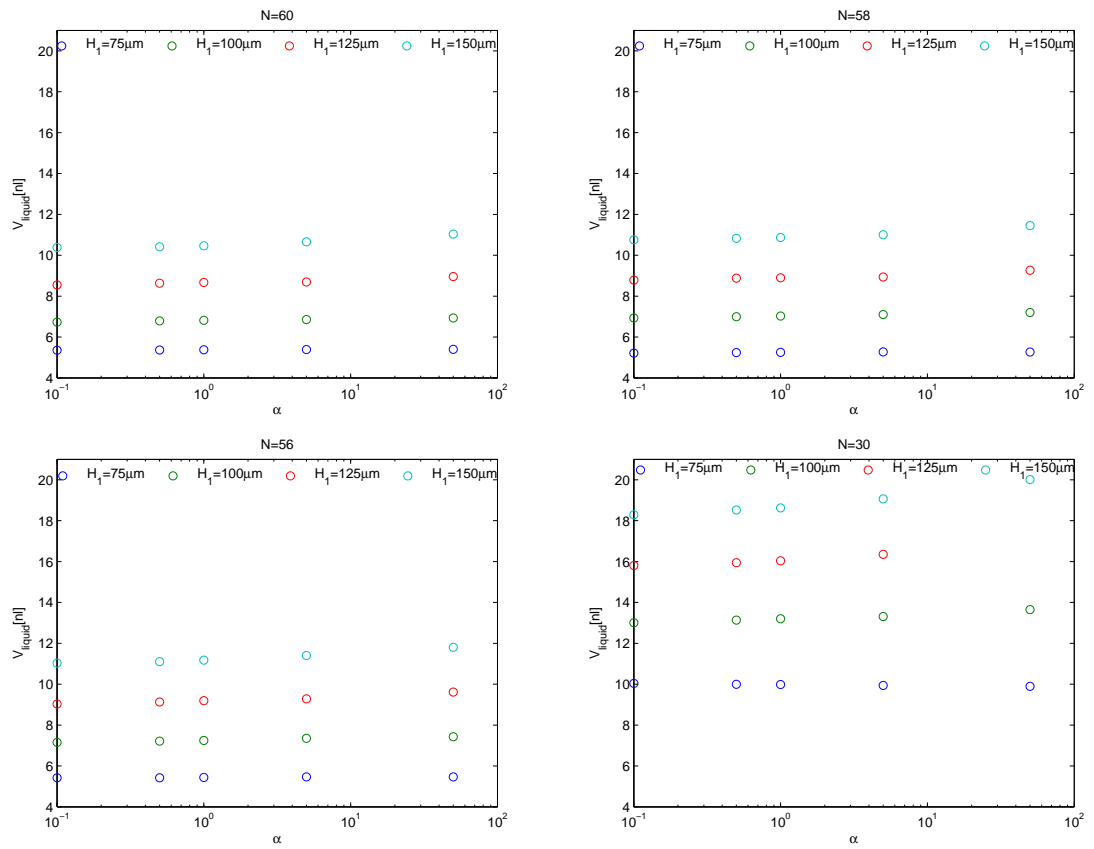


Figure 4.25: Variations of liquid charge with channel depth for different values of  $\alpha$ .

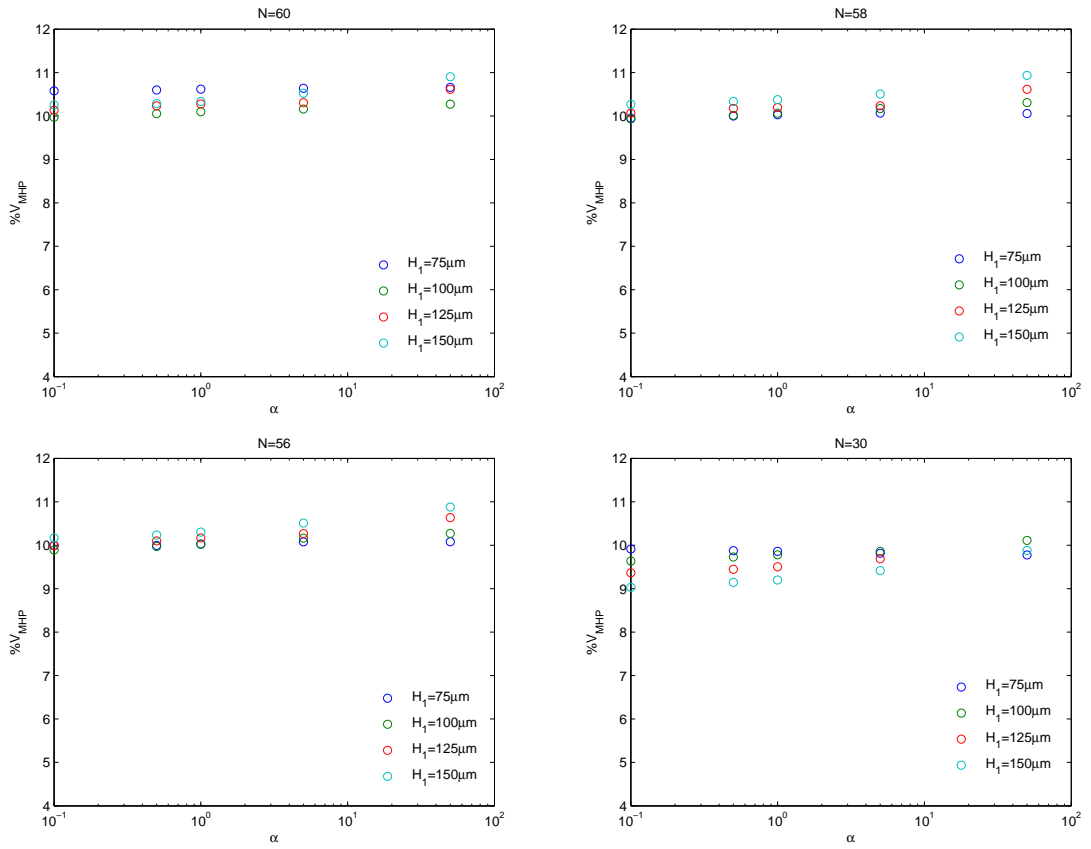


Figure 4.26: Percent of volume charge corresponding to maximum heat transport capacity of the pipe.

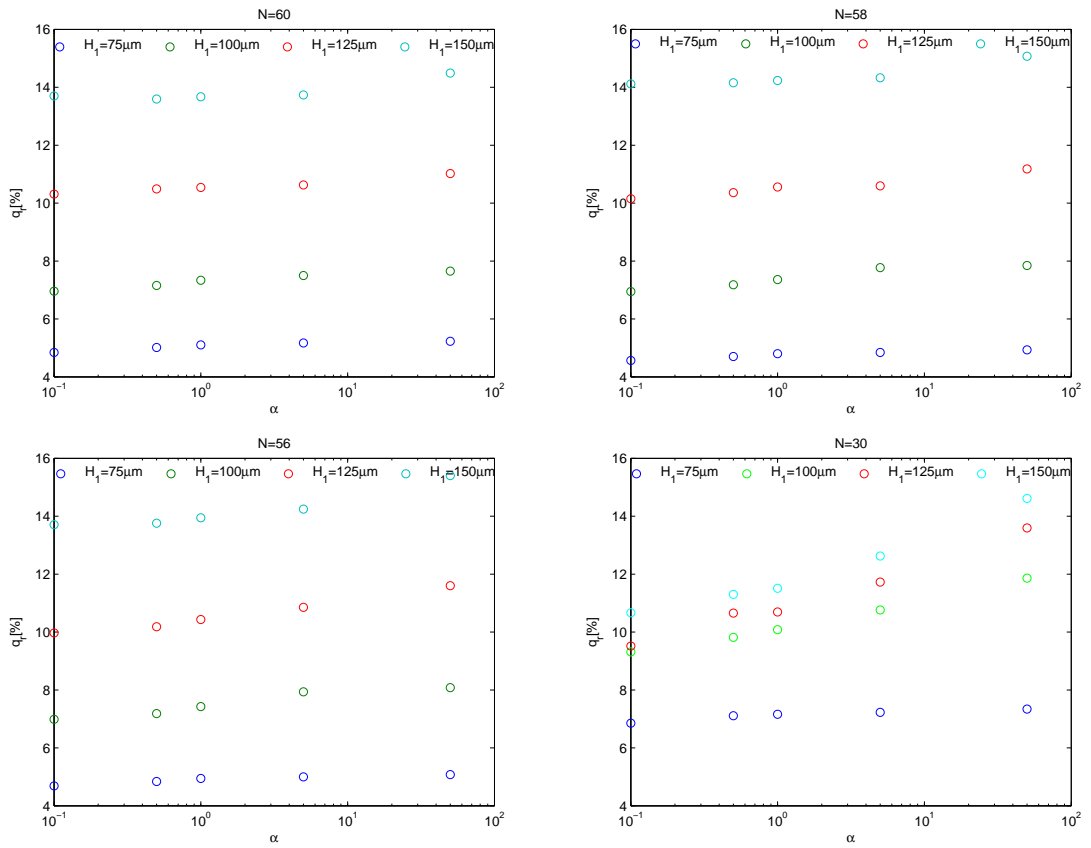


Figure 4.27: Variations of MHP heat transport capacity with channel depth for different values of  $\alpha$ .

## BIBLIOGRAPHY

- [1] O.M. Alifanov. *Inverse Heat Transfer Problems*. Springer, 1994.
- [2] K.K. Ambatipudi and M.M. Rahman. Analysis of conjugate heat transfer in microchannel heat sinks. *Numerical Heat Transfer, Part A*, 37:711–731, 2000.
- [3] K. Atkinson and W. Han. *Theoretical Numerical Analysis- A Functional Analysis Framework*. Springer, 2001.
- [4] M. Le Berre, G. Pandraud, P. Morfouli, and M. Lallemand. The performance of micro heat pipes measured by integrated sensors. *Journal of Micromechanics and Microengineering*, 16:1047–1050, 2006.
- [5] R. Chein and G. Huang. Analysis of microchannel heat sink performance using nanofluids. *Applied Thermal Engineering*, 25(17-18):3104–3114, December 2005.
- [6] E. K. P. Chong and S. Zák. *An in introduction to optimization*. Wiley, 2nd edition, 2001.
- [7] M.J. Colaço and H.R.B. Orlande. Inverse natural convection problem of simultaneous estimation of two boundary heat fluxes in irregular cavities. *International Journal of Heat and Mass Transfer*, 47(6-7):1201–1215, March 2004.
- [8] T.P. Cotter. Principles and prospects of micro heat pipes. *Proceedings 5th International Heat Pipe Conference*, Tsukuba, Japan:328–335, 1984.
- [9] J.R. Culham, M.M. Yovanovich, and T.F. Lemczyk. Thermal characterization of electronic packages using three-dimensional Fourier series solutions. *Journal of Electronic Packaging*, 122:233–239, September 2000.
- [10] G. Dalarozée. Introduction to reliability. *Microelectronic Engineering*, 49(1-2):3–10, November 1999.
- [11] M. Fabbri and V.K. Dhir. Optimized heat transfer for high power electronic cooling using arrays of microjets. *ASME Journal of Heat Transfer*, 127:760–769, July 2005.
- [12] A. Faghri. *Heat Pipe Science and Technology*. Taylor & Francis, 1995.
- [13] C. Gillot, Y. Avenas, N. Cezac, G. Poupon, C. Schaeffer, and E. Fournier. Silicon heat pipes used as thermal spreaders. *IEEE Transactions on Components and Packaging Technologies*, 26(2):332–339, June 2003.
- [14] C. Gillot, L. Meysenc, C. Schaeffer, and A. Bricard. Integrated single and two-phase micro heat sinks under igbt chips. *IEEE Transactions on Components and Packaging Technologies*, 22(3):384–389, September 1999.

- [15] M. Groll, M. Schneider, V. Sartre, M.C. Zaghoudi, and M. Lallemand. Thermal control of electronic equipment by heat pipes. *Revue Générale de Thermique*, 37(5):323–352, May 1998.
- [16] M.D. Gunzburger and H.-C. Lee. Analysis and approximation of optimal control problems for first-order elliptic systems in three dimensions. *Applied Mathematics and Computation*, 100(1):49–70, April 1999.
- [17] J.M. Ha and G.P. Peterson. The interline heat transfer of evaporating thin films along a micro grooved surface. *ASME Journal of Heat Transfer*, 118:747–755, August 1996.
- [18] I. Hassan, P. Phutthavong, and Abdelgawad. Microchannel heat sinks: An overview of the state-of-the-art. *Microscale Thermophysical Engineering*, 8:183–205, 2004.
- [19] S. Hingorani, C.J. Fahrner, D.W. Mackowski, J.S. Goodling, and R.C. Jaeger. Optimal sizing of planar thermal spreaders. *ASME Journal of Heat Transfer*, 116(2):296–301, May 1994.
- [20] C.-H. Huang and B.-H. Chao. An inverse geometry problem in identifying irregular boundary configurations. *International Journal of Heat and Mass Transfer*, 40(9):2045–2053, June 1997.
- [21] C.-H. Huang and H.-M. Chen. Inverse geometry problem of identifying growth of boundary shapes in a multiple region domain. *Numerical Heat Transfer, Part A*, 35(4):435–450, March 1999.
- [22] C.-H. Huang and J.-H. Hsiao. A non-linear fin design problem in determining the optimum shape of spine and longitudinal fins. *Communications in Numerical Methods in Engineering*, 19:111–124, 2003.
- [23] C.-H. Huang and C.-C. Shih. A shape identification problem in estimating simultaneously two interfacial configurations in a multiple region domain. *Applied Thermal Engineering*, 26(1):77–88, January 2006.
- [24] C.-H. Huang and C.-Y. Yeh. An inverse problem in simultaneous estimating the Biot numbers of heat and moisture transfer for a porous material. *International Journal of Heat and Mass Transfer*, 45(23):4643–4653, November 2002.
- [25] C.-H. Huang and C.-Y. Yeh. An optimal control algorithm for entrance concurrent flow problems. *International Journal of Heat and Mass Transfer*, 46(6):1013–1027, March 2003.
- [26] U. Imke. Porous media simplified simulation of single- and two- phase flow heat transfer in micro-channel heat exchangers. *Chemical Engineering Journal*, 101(1-3):295–302, August 2004.



- [27] M. Ivanova, C. Schaeffer, Y. Avenas, A. Lai, and C. Gillot. Realization and thermal analysis of silicon thermal spreaders used in power electronics cooling. *IEEE International Conference on Industrial Technology*, 2:1124–1129, 10-12 December 2003.
- [28] D.S. Kercher, J.-B. Lee, O. Brand, M.G. Allen, and A. Glezer. Microjet cooling devices for thermal management of electronics. *IEEE Transactions on Components and Packaging Technologies*, 26(2):359–366, June 2003.
- [29] D. Khrustalev and A. Faghri. Heat transfer during evaporation on capillary-grooved structures of heat pipes. *ASME Journal of Heat Transfer*, 117:740–747, August 1995.
- [30] D. Khrustalev and A. Faghri. Fluid flow effects in evaporation from liquid-vapor meniscus. *ASME Journal of Heat Transfer*, 118:725–730, 1996.
- [31] D. Khrustalev and A. Faghri. Coupled liquid and vapor flow in miniature passages with micro grooves. *ASME Journal of Heat Transfer*, 121:729–733, 1999.
- [32] R. W. Knight, D.J. Hall, J.S. Goodling, and R.C. Jaeger. Heat sink optimization with application to microchannels. *IEEE Transactions on Components, Hybrids, and Manufacturing Technology*, 15(5):832–842, October 1992.
- [33] R.W. Knight, J.S. Goodling, and B.E. Gross. Optimal thermal design of air cooled forced convection finned heat sinks- experimental verification. *IEEE Transactions on Components, Hybrids, and Manufacturing Technology*, 15(5):754–760, October 1992.
- [34] A. Lai, C. Gillot, M. Ivanova, Y. Avenas, C. Louis, C. Schaeffer, and E. Fournier. Thermal characterization of flat silicon heat pipes. *20th IEEE Semiconductor Thermal Measurement and Management Symposium*, pages 21–25, 9-11 March 2004.
- [35] P. Lall, M. Pecht, and E. B. Hakim. Characterization of functional relationship between temperature and microelectronic reliability. *Microelectronics and Reliability*, 35(3):377–402, March 1995.
- [36] S. Launay, V. Sartre, and M. Lallemand. Experimental study on silicon micro heat pipe arrays. *Applied Thermal Engineering*, 24(2-3):233–243, February 2004.
- [37] S. Lenhart and D.G. Wilson. Optimal control of heat transfer problem with convective boundary condition journal of optimization theory and applications. *Journal of Optimization Theory and Applications*, 79(3):581–597, December 1993.
- [38] H.-Y. Li and W.-M. Yan. Identification of wall heat flux for turbulent forced convection by inverse analysis. *International Journal of Heat and Mass Transfer*, 46(6):1041–1048, March 2003.
- [39] J. Li, G. P. Peterson, and P. Cheng. Three-dimensional analysis of heat transfer in a micro-heat sink with single phase flow. *International Journal of Heat and Mass Transfer*, 47(19-20):4215–4231, September 2004.

- [40] J.L. Lions. *Optimal Control Systems Governed by Partial Differential Equations*. Springer, 1971.
- [41] J.P. Longtin, B. Badran, and F. M. Gerner. A one-dimensional model of a micro heat pipe during steady-state operation. *ASME Journal of Heat Transfer*, 116:709–715, August 1995.
- [42] J. C. De los Reyes. A primal-dual active set method for bilaterally control constrained optimal control of the navier-stokes equations. *Numerical Functional Analysis and Optimization*, 25(1):657–683, 2005.
- [43] T. J. Martin and G. S. Dulikravich. Inverse determination of steady heat convection coefficient distributions. *ASME Journal of Heat Transfer*, 120:328–334, May 1998.
- [44] O.S. Nadgauda. Fabrication, filling, sealing and testing of micro heat pipes, Master Thesis, Auburn University, December 2006.
- [45] H.M. Park and W.J. Lee. A new numerical method for the boundary optimal control problems of the heat conduction equation. *International Journal for Numerical Methods in Engineering*, 53(7):1593–1613, March 2002.
- [46] H.M. Park and H.J. Shin. Empirical reduction of modes for the shape identification problems of heat conduction systems. *Computer Methods in Applied Mechanics and Engineering*, 192(15):1893–1908, April 2003.
- [47] K. Park and K.-S. Lee. Flow and heat transfer characteristics of the evaporating extended meniscus in a micro-capillary channel. *International Journal of Heat and Mass Transfer*, 46(24):4587–4594, November 2003.
- [48] Y. Peles, A. Kosar, C. Mishra, C.-J. Kuo, and B. Schneider. Forced convective heat transfer across a pin fin micro heat sink. *International Journal of Heat and Mass Transfer*, 48(17):3615–3627, August 2005.
- [49] X. F. Peng and G. P. Peterson. The effect of thermofluid and geometrical parameters on convection of liquids through rectangular microchannels. *International Journal of Heat and Mass Transfer*, 38(4):755–758, March 1995.
- [50] X. F. Peng and G. P. Peterson. Convective heat transfer and flow friction for water flow in microchannel structures. *International Journal of Heat and Mass Transfer*, 39(12):2599–2608, August 1996.
- [51] X. F. Peng, B. X. Wang, G. P. Peterson, and H. B. Ma. Experimental investigation of heat transfer in flat plates with rectangular microchannels. *International Journal of Heat and Mass Transfer*, 38(1):127–137, January 1995.

- [52] P. Razelos and R.N. Krikkis. On the optimum thermal design of individual longitudinal fins with rectangular profile. *International Communications in Heat and Mass Transfer*, 30(3):349–358, 2003.
- [53] J. H. Ryu, D. H. Choi, and S. J. Kim. Numerical optimization of the thermal performance of a microchannel heat sink. *International Journal of Heat and Mass Transfer*, 45(13):2823–2827, June 2002.
- [54] J. H. Ryu, D. H. Choi, and S. J. Kim. Three-dimensional numerical optimization of a manifold microchannel heat sink. *International Journal of Heat and Mass Transfer*, 46(9):1553–1562, April 2003.
- [55] A.K. Saha and S. Acharya. Parametric study of unsteady flow and heat transfer in a pin-fin heat exchanger. *International Journal of Heat and Mass Transfer*, 46(20):3815–3830, September 2003.
- [56] O. Salmela. The effect of introducing increased-reliability-risk electronic components into 3rd generation telecommunications systems. *Reliability Engineering & System Safety*, 89(2):208–218, August 2005.
- [57] V. Sartre, M.C. Zaghoudi, and M. Lallemand. Effect of interfacial phenomena on evaporative heat transfer in micro heat pipes. *International Journal of Thermal Sciences*, 39:498–504, 2000.
- [58] M. Silieti, E. Divo, and A.J. Kassab. An inverse boundary element method/genetic algorithm based approach for retrieval of multi-dimensional heat transfer coefficients within film cooling holes/slots. *Inverse Problems in Science and Engineering*, 13(1):79–98, February 2005.
- [59] F. Simionescu and D.K. Harris. Estimation of the heat transfer coefficient of a microchannel heat sink using an optimal control technique. In *Proceedings of ASME ICNMM2006 4th International Conference on Nanochannels, Microchannels and Minichannels*, Limerick, Ireland, June 19-21, 2006.
- [60] F. Simionescu, A.J. Meir, and D.K. Harris. Approximation of an optimal convective heat transfer coefficient. *Optimal Control Applications and Methods*, 27:237–253, 2006.
- [61] P.C. Stephan and C.A. Busse. Analysis of the heat transfer coefficient of grooved heat pipe evaporator walls. *International Journal of Heat and Mass Transfer*, 35(2):383–391, 1992.
- [62] B. Suman, S. De, and S. DasGupta. A model of the capillary limit of a micro heat pipe and prediction of the dry-out length. *International Journal of Heat and Fluid Flow*, 26:495–505, 2005.

- [63] B. Suman and N. Hoda. Effect of variations in thermophysical properties and design parameters on the performance of a V-shaped micro grooved heat pipe. *International Journal of Heat and Mass Transfer*, 48:2090–2101, 2005.
- [64] L.W. Swanson and G.P. Peterson. The interfacial thermodynamics of micro heat pipes. *ASME Journal of Heat Transfer*, 117:195–201, February 1995.
- [65] S.K. Thomas, R.C. Lykins, and Kirk L. Yerkes. Fully developed laminar flow in trapezoidal grooves with shear stress at the liquidvapor interface. *International Journal of Heat and Mass Transfer*, 44(18):3397–3412, September 2001.
- [66] C.L. Tien, A. Majumdar, and F. Gerner. *Microscale Energy Transport*. Taylor & Francis, 1998.
- [67] K.C. Toh, X.Y. Chen, and J.C. Chai. Numerical computation of fluid flow and heat transfer in microchannels. *International Journal of Heat and Mass Transfer*, 45(26):5133–5141, December 2002.
- [68] D. B. Tuckerman and F. W. Pease. High performance heat sinking for VLSI. *IEEE Electron Device Letters*, 2(5):126–129, May 1981.
- [69] K. Vafai and L. Zhu. Analysis of two-layered micro-channel heat sink concept in electronic cooling. *International Journal of Heat and Mass Transfer*, 42(12):2287–2397, June 1999.
- [70] C.-Y. Wang, M. Groll, S. Rösler, and C.-J. Tu. Porous medium model for two-phase flow in mini channels with applications to micro heat pipes. *Heat Recovery Systems & CHP*, 14(4):377–389, 1994.
- [71] J.J. Wei and H. Honda. Effects of fin geometry on boiling heat transfer from silicon chips with micro-pin-fins immersed in FC-72. *International Journal of Heat and Mass Transfer*, 46(21):4059–4070, October 2003.
- [72] A. Weisberg, H. H. Bau, and J. N. Zemel. Analysis of micro-channels for integrated cooling. *International Journal of Heat and Mass Transfer*, 35(10):2465–2474, 1992.
- [73] H. Y. Wu and P. Cheng. An experimental study of convective heat transfer in silicon microchannels with different surface conditions. *International Journal of Heat and Mass Transfer*, 46(14):2547–2556, July 2003.
- [74] R.-H. Yeh and M. Chang. Optimum longitudinal convective fin arrays. *International Communications in Heat and Mass Transfer*, 22(3):445–460, 1995.
- [75] E. P. Zafiroopoulos and E. N. Dialynas. Reliability and cost optimization of electronic devices considering the component failure rate uncertainty. *Reliability Engineering & System Safety*, 84(3):271–284, June 2004.

- [76] C. Y. Zhao and T. J. Lu. Analysis of microchannel heat sinks for electronics cooling. *International Journal of Heat and Mass Transfer*, 45(24):4857–4869, November 2002.